ETSI GR THz 003 V1.1.1 (2024-12)

TeraHertz modeling (THz);
Channel measurements and modeling in THz bands

Disclaimer

The present document has been produced and approved by the TeraHertz (THz) ETSI Industry Specification Group (ISG) and represents the views of those members who participated in this ISG.
It does not necessarily represent the views of the entire ETSI membership.

Reference
DGR/THz-003

Keywords
measurement, model

ETSI

650 Route des Lucioles
F-06921 Sophia Antipolis Cedex - FRANCE

Tel.: +33 4 92 94 42 00 Fax: +33 4 93 65 47 16

Siret N° 348 623 562 00017 - APE 7112B
Association à but non lucratif enregistrée à la
Sous-Préfecture de Grasse (06) N° w061004871

Contents

Intellectual Property Rights

Essential patents

IPRs essential or potentially essential to normative deliverables may have been declared to ETSI. The declarations pertaining to these essential IPRs, if any, are publicly available for **ETSI members and non-members**, and can be found in ETSI SR 000 314: *"Intellectual Property Rights (IPRs); Essential, or potentially Essential, IPRs notified to ETSI in respect of ETSI standards"*, which is available from the ETSI Secretariat. Latest updates are available on the ETSI IPR online database.

Pursuant to the ETSI Directives including the ETSI IPR Policy, no investigation regarding the essentiality of IPRs, including IPR searches, has been carried out by ETSI. No guarantee can be given as to the existence of other IPRs not referenced in ETSI SR 000 314 (or the updates on the ETSI Web server) which are, or may be, or may become, essential to the present document.

Trademarks

The present document may include trademarks and/or tradenames which are asserted and/or registered by their owners. ETSI claims no ownership of these except for any which are indicated as being the property of ETSI, and conveys no right to use or reproduce any trademark and/or tradename. Mention of those trademarks in the present document does not constitute an endorsement by ETSI of products, services or organizations associated with those trademarks.

DECT™, **PLUGTESTS™**, **UMTS™** and the ETSI logo are trademarks of ETSI registered for the benefit of its Members. **3GPP™**, **LTE™** and **5G™** logo are trademarks of ETSI registered for the benefit of its Members and of the 3GPP Organizational Partners. **oneM2M™** logo is a trademark of ETSI registered for the benefit of its Members and of the oneM2M Partners. **GSM**® and the GSM logo are trademarks registered and owned by the GSM Association.

Foreword

This Group Report (GR) has been produced by ETSI Industry Specification Group (ISG) TeraHertz (THz).

Modal verbs terminology

In the present document "**should**", "**should not**", "**may**", "**need not**", "**will**", "**will not**", "**can**" and "**cannot**" are to be interpreted as described in clause 3.2 of the ETSI Drafting Rules (Verbal forms for the expression of provisions).

"**must**" and "**must not**" are **NOT** allowed in ETSI deliverables except when used in direct citation.

Executive summary

The present document focuses on channel measurements and modeling in THz bands. Specifically, it first summarizes the key channel measurement scenarios and frequency bands for THz communications and sensing systems. It identifies the key THz-specific propagation aspects, such as effects of atmospheric absorption, micro-mobility, specifics of scattering and surface roughness, impact of large arrays and near-field propagation, and material characterization in THz bands. It summarizes relevant channel measurements and open measurement datasets performed in THz bands. Next, it details the relevant channel modeling approaches, including deterministic, stochastic, hybrid, and machine learning models and introduces updates to the existing geometry based stochastic channel model defined by 3GPP with extensions required to support THz frequency bands. Finally, it introduces key channel modeling considerations for Integrated Sensing And Communications (ISAC) and Reconfigurable Intelligent Surfaces (RIS).

Introduction

The emergence of TeraHertz (THz) communication and sensing systems has garnered significant attention as a promising solution to meet the increasing demand for ultra-high data rates, low-latency applications, and enhanced spectrum utilization in future wireless networks. Positioned between millimetre-wave and infrared frequencies, the THz band (0,1 THz to 10 THz) offers an expansive amount of untapped spectrum. This potential makes it a strong candidate for enabling technologies such as 6G, ultra-fast wireless backhaul, and other advanced use cases that require high-capacity links.

However, despite its promise, the deployment of THz communications presents unique challenges. THz waves experience higher path losses, atmospheric absorption, and sensitivity to obstacles compared to lower frequency bands. To ensure robust and reliable THz communications, it is critical to develop a comprehensive understanding of the propagation characteristics and to model the radio channels accurately under various environmental conditions and deployment scenarios.

The present document summarizes channel measurement scenarios, frequency bands, and radio propagation characteristics specific to the THz range. Furthermore, it extends state-of-the-art channel modeling techniques - ranging from geometry based stochastic, deterministic, to machine learning models - to support communication and sensing in THz bands. Furthermore, it discusses the key considerations related to channel modeling for ISAC and RIS.

Overall, the present document aims to provide a comprehensive framework for understanding THz-specific propagation effects and the development of accurate channel models, consequently contributing to ongoing efforts to enable reliable THz communication and sensing systems.

1 Scope

The present document focuses on channel measurements and channel modeling in THz frequency bands.

2 References

2.1 Normative references

Normative references are not applicable in the present document.

2.2 Informative references

References are either specific (identified by date of publication and/or edition number or version number) or non-specific. For specific references, only the cited version applies. For non-specific references, the latest version of the referenced document (including any amendments) applies.

NOTE: While any hyperlinks included in this clause were valid at the time of publication, ETSI cannot guarantee their long term validity.

The following referenced documents are not necessary for the application of the present document but they assist the user with regard to a particular subject area.

[i.1] ETSI TR 138 901: "5G; Study on channel model for frequencies from 0.5 to 100 GHz (3GPP TR 38.901 version 18.0.0 Release 18)".

[i.2] S. Tarboush et al.: "TeraMIMO: A channel simulator for wideband ultramassive MIMO terahertz communications", 2021, IEEE Transactions on Vehicular Technology, Vol: 70, Issue: 12, December 2021.

[i.3] Han, C., Wang, Y., Li, Y., Chen, Y., Abbasi, N. A., Kürner, T., & Molisch, A. F. (2022): "Terahertz wireless channels: A holistic survey on measurement, modeling, and analysis". IEEE Communications Surveys & Tutorials, 24(3), 1670-1707.

[i.4] C. Jansen, R. Piesiewicz, D. Mittleman, T. Kürner and M. Koch: "The Impact of Reflections From Stratified Building Materials on the Wave Propagation in Future Indoor Terahertz Communication Systems", in IEEE Transactions on Antennas and Propagation, vol. 56, no. 5, pp. 1413-1419, May 2008.

[i.5] S. Kim, W. T. Khan, A. Zajić, and J. Papapolymerou: "D-band channel measurements and characterization for indoor applications", IEEE Trans. Antennas Propag., vol. 63, no. 7, pp. 3198-3207, July 2015.

[i.6] S. L. H. Nguyen, J. Järveläinen, A. Karttunen, K. Haneda and J. Putkonen: "Comparing radio propagation channels between 28 and 140 GHz bands in a shopping mall", 12th European Conference on Antennas and Propagation (EuCAP 2018), pp. 1-5, London, 9-13 April, 2018.

[i.7] L. Pometcu and R. D'Errico: "Characterization of sub-THz and mmwave propagation channel for indoor scenarios", 12th European Conference on Antennas and Propagation (EuCAP 2018), pp. 1-4, London, 9-13 April, 2018.

[i.8] S. Priebe, M. Kannicht, M. Jacob, and T. Kürner: "Ultra broadband indoor channel measurements and calibrated ray tracing propagation modeling at THz frequencies", Journal of Communications and Networks, vol. 15, no. 6, pp. 547-558, December 2013.

[i.9] C. Jansen et al.: "Diffuse scattering from rough surfaces in THz communication channels", IEEE Trans. THz Sci. Technol., vol. 1, no. 2, pp. 462-472, November 2011.

[i.10] Kim S, Zajić A (2015): "Statistical characterization of 300 GHz propagation on a desktop". IEEE Transactions on Vehicular Technology, doi: 10.1109/TVT.2014.2358191.

[i.11] Kim S., Zajić A. (2016): "Characterization of 300 GHz wireless channel on a computer motherboard". IEEE Transactions on Antennas and Propagation, doi: 10.1109/TAP.2016.2620598.

[i.12] Fricke A., Rey S., Achir M., et al. (2013): "Reflection and transmission properties of plastic materials at THz frequencies". 38th International Conference on Infrared, Millimetre, and Terahertz Waves (IRMMW-THz), doi: 10.1109/IRMMWTHz.2013.6665413.

[i.13] Fricke A., Achir M., Le Bars P., et al. (2015): "Characterization of transmission scenarios for terahertz intra-device communications. IEEE-APS Topical Conference on Antennas and Propagation in Wireless Communications (APWC)", doi: 10.1109/APWC.2015.7300195.

[i.14] Cheng C., Kim S., Zajić A. (2018): "Study of diffraction at 30 GHz, 140 GHz, and 300 GHz". IEEE International Symposium on Antennas and Propagation USNC/URSI National Radio Science Meeting, doi: 10.1109/APUSNCURSINRSM.2018.86088.

[i.15] Kürner T., Fricke A., Rey S., et al. (2015): "Measurements and modeling of basic propagation characteristics for intra-device communications at 60 GHz and 300 GHz". Journal of Infrared, Millimetre, and Terahertz Waves, doi:10.1007/s10762- 014-0117-5.

[i.16] Fu J., Juyal P., Zajić A. (2019): "THz channel characterization of chip-to-chip communication in desktop size metal enclosure". IEEE Transactions on Antennas and Propagation, doi: 10.1109/TAP.2019.2934908.

[i.17] Cheng C., Kim S., Zajić A. (2017): "Comparison of path loss models for indoor 30 GHz, 140 GHz, and 300 GHz channels". 11th European Conference on Antennas and Propagation (EUCAP), doi: 10.23919/EuCAP.2017.7928124.

[i.18] Piesiewicz R., Jansen C., Mittleman D., et al. (2007): "Scattering analysis for the modeling of THz communication systems". IEEE Transactions on Antennas and Propagation, doi: 10.1109/TAP.2007.908559.

[i.19] Fricke A., Kürner T., Achir M., et al. (2017): "A model for the reflection of terahertz signals from printed circuit board surfaces". 11th European Conference on Antennas and Propagation (EUCAP), doi: 10.23919/EuCAP.2017.7928148.

[i.20] Jacob M., Priebe S., Dickhoff R., et al. (2012): "Diffraction in mm and sub-mm wave indoor propagation channels". IEEE Transactions on Microwave Theory and Techniques, doi: 10.1109/TMTT.2011.2178859.

[i.21] He D., Guan K., Ai B. et al. (2017): "Stochastic channel modeling for kiosk applications in the terahertz Band". IEEE Transactions on Terahertz Science and Technology, doi: 10.1109/TTHZ.2017.2720962.

[i.22] Recommendation ITU-R P.676-12: "Attenuation by atmospheric gases and related effects", August 2019.

[i.23] Recommendation ITU-R P.838-3: "Specific attenuation model for rain for use in prediction methods", March 2005.

[i.24] Recommendation ITU-R P.840-8: "Attenuation due to clouds and fog", August 2019.

[i.25] Fricke A. (2016): "Channel Modeling Document", In: IEEE P802.15™: "Working Group for Wireless Personal Area Networks (WPANs)".

[i.26] Cheng C., Zajić A. (2020): "Characterization of Propagation Phenomena Relevant for 300 GHz Wireless Data Centre Links", In: IEEE Transactions on Antennas and Propagation, vol. 68, no. 2, pp. 1074-1087.

[i.27] Eckhardt J. M., Doeker T., Rey S., Kürner T. (2019): "Measurements in a Real Data Centre at 300 GHz and Recent Results", In: Proceedings of 13th European Conference on Antennas and Propagation (EuCAP 2019), Krakow, Poland.

[i.28] Cheng C., Sangodoyin S., Zajić A. (2020): "THz Cluster-Based Modeling and Propagation Characterization in a Data Centre Environment", In: IEEE Access, vol. 8.

[i.29] Petrov V., Eckhardt J. M., Moltchanov D. (2020): "Measurements of Reflection and Penetration Losses in Low Terahertz Band Vehicular Communications", Proc. of EuCAP, 1-5.

[i.30] Priebe S., Kürner T. (2013): "Stochastic modeling of THz indoor radio channels". IEEE Transactions on Wireless Communications, doi: 10.1109/TWC.2013.072313.121581.

[i.31] Guan K., Peng B., He D. et al. (2019): "Measurement, simulation, and characterization of train-to-infrastructure inside-station channel at the terahertz", IEEE Transactions on Terahertz Science and Technology, doi: 10.1109/TTHZ.2019.2909975.

[i.32] J. Fu, P. Juyal, and A. Zajić: "Modeling of 300 GHz chip-to-chip wireless channels in metal enclosures", in IEEE Transactions on Wireless Communications.

[i.33] L. Pometcu and R. D'Errico: "An Indoor Channel Model for High Data-Rate Communications in D-Band", in IEEE Access, vol. 8, pp. 9420-9433, 2020.

[i.34] Guan K., Li G., Kürner T. et al. (2016): "On millimetre wave and THz mobile radio channel for smart rail mobility". IEEE Transactions on Vehicular Technology, doi: 10.1109/TVT.2016.2624504.

[i.35] Rappaport T. S., Xing Y., Kanhere O. et al. (2019): "Wireless communications and applications above 100 GHz: opportunities and challenges for 6G and beyond". IEEE Access, doi: 10.1109/ACCESS.2019.2921522.

[i.36] Vitucci E. M., Zoli M., Fuschini M. et al. (2018): "Tri-band mm-wave directional channel measurements in indoor environment". In: 2018 IEEE 29th Annual International Symposium on Personal, Indoor and Mobile Radio Communications (PIMRC), Bologna, 2018.

[i.37] Guan K., Zhong Z., Ai B. et al. (2014): "Propagation measurements and analysis for train stations of high-speed railway at 930 MHz". IEEE Transactions on Vehicular Technology, doi: 10.1109/TVT.2014.2307917.

[i.38] Guan K., Peng B., He D. et al. (2019): "Channel characterization for intra-wagon communication at 60 and 300 GHz bands". IEEE Transactions on Vehicular Technology, doi: 10.1109/TVT.2019.2907606.

[i.39] T. S. Rappaport, K. A. Remley, C. Gentile, A. F. Molisch and A. Zajić: "Radio Propagation Measurements and Channel Modeling: Best Practices for Millimetre-Wave and Sub-Terahertz Frequencies", Cambridge, U.K.: Cambridge Univ. Press, 2021.

[i.40] N. A. Abbasi et al.: "Double directional channel measurements for THz communications in an urban environment", Proc. IEEE Int. Conf. Commun. (ICC), pp. 1-6, June 2020.

[i.41] S. Kim and A. G. Zajić: "Statistical characterization of 300-GHz propagation on a desktop", IEEE Trans. Veh. Technol., vol. 64, no. 8, pp. 3330-3338, August 2015.

[i.42] C.-L. Cheng, S. Sangodoyin and A. Zajić: "THz cluster-based modeling and propagation characterization in a data centre environment", IEEE Access, vol. 8, pp. 56544-56558, 2020.

[i.43] C.-L. Cheng, S. Sangodoyin and A. Zajić: "Terahertz MIMO fading analysis and doppler modeling in a data centre environment", Proc. Eur. Conf. Antennas Propag. (EuCAP), pp. 1-5, March 2020.

[i.44] Y. Zantah, F. Sheikh, A. A. Abbas, M. Alissa and T. Kaiser: "Channel measurements in lecture room environment at 300 GHz", Proc. Int. Workshop Mobile Terahertz Syst. (IWMTS), pp. 1-5, July 2019.

[i.45] N. A. Abbasi, A. Hariharan, A. M. Nair and A. F. Molisch: "Channel measurements and path loss modeling for indoor THz communication", Proc. Eur. Conf. Antennas Propag. (EuCAP), pp. 1-5, March 2020.

[i.46] Z. Yu, Y. Chen, G. Wang, W. Gao and C. Han: "Wideband channel measurements and temporal-spatial analysis for terahertz indoor communications", Proc. IEEE Int. Conf. Commun. Workshops (ICC Workshops), pp. 1-6, June 2020.

[i.47] Y. Chen, C. Han, Z. Yu and G. Wang: "140 GHz channel measurement and Characterization in an office room", Proc. IEEE Int. Conf. Commun. (ICC), pp. 1-6, June 2021.

[i.48] J. He, Y. Chen, Y. Wang, Z. Yu and C. Han: "Channel measurement and path-loss Characterization for low-terahertz indoor scenarios", Proc. IEEE Int. Conf. Commun. Workshops (ICC Workshops), pp. 1-6, June 2021.

[i.49] Y. Wang, Y. Li, Y. Chen, Z. Yu and C. Han: "0.3 THz channel measurement and analysis in an L-shaped indoor hallway", Proc. IEEE Int. Conf. Commun. (ICC), pp. 1-6, June 2022.

[i.50] Y. Li, Y. Wang, Y. Chen, Z. Yu and C. Han: "Channel measurement and analysis in an indoor corridor scenario at 300 GHz", Proc. IEEE Int. Conf. Commun. (ICC), pp. 1-6, June 2022.

[i.51] N. Abbasi et al.: "Double-directional channel measurements for urban THz communications on a linear route", Proc. IEEE Int. Conf. Commun. Workshops (ICC Workshops), pp. 1-6, June 2021.

[i.52] N. Abbasi et al.: "Ultra-wideband double directional channel measurements for THz communications in urban environments", Proc. IEEE Int. Conf. Commun. (ICC), pp. 1-6, June 2021.

[i.53] S. L. H. Nguyen, K. Haneda, J. Järveläinen, A. Karttunen and J. Putkonen: "Large-scale parameters of spatio-temporal short-range indoor backhaul channels at 140 GHz", Proc. IEEE Veh. Technol. Conf. (VTC), pp. 1-6, April 2021.

[i.54] Y. Xing and T. S. Rappaport: "Propagation measurements and path loss models for sub-THz in urban microcells", Proc. IEEE Int. Conf. Commun., pp. 1-6, March 2021.

[i.55] S. Ju, Y. Xing, O. Kanhere and T. S. Rappaport: "Millimetre wave and sub-terahertz spatial statistical channel model for an indoor office building", IEEE J. Sel. Areas Commun., vol. 39, no. 6, pp. 1561-1575, June 2021.

[i.56] S. Ju, Y. Xing, O. Kanhere and T. S. Rappaport: "Sub-terahertz channel measurements and characterization in a factory building", Proc. IEEE Int. Conf. Commun. (ICC), pp. 1-6, June 2022.

[i.57] O. Kanhere and T. S. Rappaport: "Outdoor sub-THz position location and tracking using field measurements at 142 GHz", Proc. IEEE Int. Conf. Commun., pp. 1-6, 2021.

[i.58] S. Ju and T. S. Rappaport: "140 GHz urban microcell propagation measurements for spatial consistency modeling", Proc. IEEE Int. Conf. Commun., pp. 1-6, 2021.

[i.59] S. Ju and T. S. Rappaport: "Sub-terahertz spatial statistical MIMO channel model for urban microcells at 142 GHz", Proc. IEEE Global Commun. Conf. (GLOBECOM), pp. 1-6, December 2021.

[i.60] D. Dupleich, R. Müller, S. Skoblikov, M. Landmann, G. Del Galdo and R. Thomä: "Characterization of the propagation channel in conference room scenario at 190 GHz", Proc. Eur. Conf. Antennas Propag. (EuCAP), pp. 1-5, July 2020.

[i.61] F. Undi, A. Schultze, W. Keusgen, M. Peter and T. Eichler: "Angle-resolved THz channel measurements at 300 GHz in an outdoor environment", Proc. IEEE Int. Conf. Commun. Workshops (ICC Workshops), pp. 1-7, June 2021.

[i.62] K. Guan et al.: "Channel sounding and ray tracing for train-to-train communications at the THz band", Proc. Eur. Conf. Antennas Propag. (EuCAP), pp. 1-5, April 2019.

[i.63] J. M. Eckhardt, T. Doeker and T. Kürner: "Indoor-to-outdoor path loss measurements in an aircraft for terahertz communications", Proc. IEEE Veh. Technol. Conf. (VTC), pp. 1-5, May 2020.

[i.64] A. Fricke, C. Homann and T. Kürner: "Time-domain propagation investigations for terahertz intra-device communications", Proc. Eur. Conf. Antennas Propag. (EuCAP), pp. 1760-1764, May 2014.

[i.65] G. A. Siles, J. M. Riera and P. Garcia-del-Pino: "Atmospheric attenuation in wireless communication systems at millimetre and THz frequencies", IEEE Antennas Propag. Mag., vol. 57, no. 1, pp. 48-61, February 2015.

[i.66] T. Doeker, J. M. Eckhardt and T. Kürner: "Channel Measurements and Modeling for Low Terahertz Communications in an Aircraft Cabin," in IEEE Transactions on Antennas and Propagation, vol. 70, no. 11, pp. 10903-10916, Nov. 2022, doi: 10.1109/TAP.2022.3191218.

[i.67] A. Schultze, F. Undi, M. Peter, W. Keusgen and T. Eichler: "Angle-resolved THz channel measurements at 300 GHz in a conference room environment", Proc. 34th Gen. Assem. Sci. Symp. Int. Union Radio Sci., pp. 1-4, 2021.

[i.68] D. Dupleich, A. Ebert, Y. Völker-Schöneberg, L. Löser, M. Boban and R. Thomä: "Spatial/Temporal Characterization of Propagation and Blockage from Measurements at sub-THz in Industrial Machines", 2023 17th European Conference on Antennas and Propagation (EuCAP), Florence, Italy, 2023, pp. 1-5, doi: 10.23919/EuCAP57121.2023.10133323.

[i.69] ETSI GR THz 001 (V1.1.1): "TeraHertz modeling (THz); Identification of use cases for THz communication systems".

[i.70] Recommendation ITU-R P.1238: "Propagation data and prediction methods for the planning of indoor radiocommunication systems and radio local area networks in the frequency range 300 MHz to 450 GHz", August 2023.

[i.71] Recommendation ITU-R P.1411: "Propagation data and prediction methods for the planning of short-range outdoor radiocommunication systems and radio local area networks in the frequency range 300 MHz to 100 GHz", August 2023.

[i.72] ETSI GR THz 002 (V1.1.1): "TeraHertz technology (THz); Identification of frequency bands of interest for THz communication systems".

[i.73] ITU Radio Regulations. Vol 1, Articles. Geneva 2020.

[i.74] J. M. Eckhardt, T. Doeker and T. Kürner (2020): "Indoor-to-Outdoor Path Loss Measurements in an Aircraft for Terahertz Communications", 2020 IEEE 91st Vehicular Technology Conference (VTC2020-Spring), 2020, pp. 1-5, doi: 10.1109/VTC2020-Spring48590.2020.9128849.

[i.75] S. Ju, Y. Xing, O. Kanhere and T. S. Rappaport (2022): "Sub-terahertz channel measurements and characterization in a factory building", ICC 2022 - IEEE International Conference on Communications, Seoul, Korea, Republic of, 2022, pp. 2882-2887, doi: 10.1109/ICC45855.2022.9838910.

[i.76] Z. Xiao, Q. Yang, J. Huang, Z. Huang, W. Zhou, Y. Gao, R. Shu, and Z. He (2018): "Terahertz communication windows and their point-to-point transmission verification", *Appl. Opt. 57*, pp. 7673-7680 (2018). doi: 10.1364/AO.57.007673.

[i.77] Zhengqing Yun, and Magdy F. Iskander: "Ray Tracing for Radio Propagation Modeling: Principles and Applications", IEEE Access 3 (2015): 1089-1100. doi: 10.1109/ACCESS.2015.2453991.

[i.78] H. Ling, R.-C. Chou, and S.-W. Lee: "Shooting and bouncing rays: Calculating the RCS of an arbitrarily shaped cavity", IEEE Trans. Antennas Propag., vol. 37, no. 2, pp. 194-205, February 1989.

[i.79] Recommendation ITU-R P.2040: "Effects of building materials and structures on radiowave propagation above about 100 MHz", approved August 23, 2023.

[i.80] Recommendation ITU-R P.527: "Electrical Characteristics of the Surface of the Earth", approved September 27, 2021.

[i.81] C. Jansen, R. Piesiewicz, D. Mittleman, T. Kürner and M. Koch: "The impact of reflections from stratified building materials on the wave propagation in future indoor terahertz communication systems", IEEE Trans. Antennas Propag., vol. 56, no. 5, pp. 1413-1419, May 2008.

[i.82] J. Gomez-Ponce et al.: "Impact of common reflecting and absorbing building materials on THz multipath channels", Radio Sci., vol. 57, no. 2, February 2022.

[i.83] F. Sheikh et al.: "Scattering and Roughness Analysis of Indoor Materials at Frequencies from 750 GHz to 1.1 THz", IEEE Transactions on Antennas and Propagation, 2021.

[i.84] H. Ragheb and E. R. Hancock: "The modified Beckmann-Kirchhoff scattering theory for rough surface analysis", Pattern Recognition, vol. 40, no. 7, pp. 2004-2020, 2007.

[i.85] C. Han, A.O. Bicen, and I. Akyildiz: "Multi-ray channel modeling and wideband characterization for wireless communications in the terahertz band", IEEE Transactions on Wireless Communications, vol. 14, no. 5, pp. 2402-2412, May 2015.

[i.86] Yuanzhe Wang, Hao Cao, Yifan Jin, Zizhe Zhou, Yinghua Wang, Jialing Huang, Yuxiao Li, Jie Huang, Cheng-Xiang Wang: "An SBR Based Ray Tracing Channel Modeling Method for THz and Massive MIMO Communications", 2022 IEEE 96th Vehicular Technology Conference (VTC2022-Fall).

[i.87] J. M. Eckhardt, T. Doeker and T. Kürner: "Hybrid Channel Model for Low Terahertz Links in a Data Centre", in IEEE Open Journal of the Communications Society, vol. 5, pp. 4731-4745, 2024, doi: 10.1109/OJCOMS.2024.3433561.

[i.88] J. M. Eckhardt: "THz Communications in a Data Centre: Channel Measurements, Modeling and Physical Layer Analysis", Düren, Germany: Shaker Verlag, 2024, doi: 10.24355/dbbs.084-202405061045-0.

[i.89] J. M. Eckhardt, A. Schultze, R. Askar, T. Doeker, M. Peter, W. Keusgen, T. Kürner: "Uniform Analysis of Multipath Components from Various Scenarios with Time-Domain Channel Sounding at 300 GHz", in IEEE Open Journal of Antennas and Propagation, vol. 4, pp. 446-460, 2023, doi: 10.1109/OJAP.2023.3263597.

[i.90] J. M. Eckhardt, T. Doeker and T. Kürner: "Channel Measurements at 300 GHz for Low Terahertz Links in a Data Centre," in IEEE Open Journal of Antennas and Propagation, vol. 5, no. 3, pp. 759-777, June 2024, doi: 10.1109/OJAP.2024.3391798.

[i.91] Eckhardt, J. M., Doeker, T., Kürner, T.: "Calibrated Impulse Responses and Extracted Multipath Components from Channel Sounding at 300 GHz in a Data Centre", 2024, doi: 10.24355/dbbs.084-202312041057-0.

[i.92] Eckhardt, J.M., Schultze, A., Askar, R., Doeker, T., Peter, M., Keusgen, W., Kürner, T.: "Extracted Multipath Components from Time-Domain Channel Sounding at 300 GHz in Various Scenarios", 2023, doi: 10.24355/dbbs.084-202301191318-0.

[i.93] Figshare, doi: 10.6084/m9.figshare.21539109.

[i.94] F. Taleb, G. G. Hernandez-Cardoso, E. Castro-Camus and M. Koch: "Transmission, Reflection, and Scattering Characterization of Building Materials for Indoor THz Communications", in IEEE Transactions on Terahertz Science and Technology, vol. 13, no. 5, pp. 421-430, Sept. 2023, doi: 10.1109/TTHZ.2023.3281773.

[i.95] Erhan Karakoca, Hasan Nayir, Gizem Sümen, Güneş Karabulut Kurt, Ali Görçin: "Sub-THz Wireless Channel Measurements", IEEE Dataport, December 14, 2022.

[i.96] Kürşat Tekbıyık, Ali Rıza Ekti, Güneş Karabulut Kurt, Ali Görçin: "THz Wireless Channel Measurements in between 240GHz and 300GHz", IEEE Dataport, December 15, 2019.

[i.97] K. Tekbıyık, A. R. Ekti, G. K. Kurt, A. Görçin and S. Yarkan: "Modeling and Analysis of Short Distance Sub-Terahertz Communication Channel via Mixture of Gamma Distribution", in IEEE Transactions on Vehicular Technology, vol. 70, no. 4, pp. 2945-2954, April 2021.

[i.98] M. F. de Guzman, K. Haneda, P. Kyösti: "Measurement-based MIMO channel model at 140GHz", February 14, 2023.

[i.99] A. Nimr (ed.): "Hexa-X Deliverable D2.3 Radio models and enabling techniques towards ultra-high data rate links and capacity in 6G", April 2023.

[i.100] M. F. De Guzman and K. Haneda: "Analysis of wave-interacting objects in indoor and outdoor environments at 142 GHz", IEEE Transactions on Antennas and Propagation, vol. 71, no. 12, pp. 9838-9848, December 2023, doi: 10.1109/TAP.2023.3318861.

[i.101] J. Kokkoniemi, J. Lehtomäki and M. Juntti: "Simplified molecular absorption loss model for 275-400 gigahertz frequency band", in Proc. 12th European Conference on Antennas and Propagation (EuCAP 2018), London, UK, 2018, pp. 1-5.

[i.102] I.E. Gordon et al.: "The HITRAN2020 molecular spectroscopic database", J. Quant. Spectrosc. Radiat. Transfer, vol. 277, pp. 1-82, January 2022.

[i.103] Jung, B. K. and Kürner, T.: "Performance analysis of 300 GHz backhaul links using historic weather data", Adv. Radio Sci., 19, 153-163, doi: 10.5194/ars-19-153-2021, 2021.

[i.104] J. Huang, Y. Cao, X. Raimundo, A. Cheema and S. Salous: "Rain Statistics Investigation and Rain Attenuation Modeling for Millimetre Wave Short-Range Fixed Links", in IEEE Access, vol. 7, pp. 156110-156120, 2019, doi: 10.1109/ACCESS.2019.2949437.

[i.105] O. Zahid and S. Salous: "Long-term rain attenuation measurement for short-range mmWave fixed link using DSD and ITU-R prediction models", in Radio Science, vol. 57, no. 4, pp. 1-21, April 2022, doi: 10.1029/2021RS007307.

[i.106] H. J. aufm Kampe: "Visibility and Liquid Water Content in the free Atmosphere", Journal of Meteorology, Vol. 7, p. 54-57, February 1950.

[i.107] Wu, Mengfan, et al.: "Direct Clustering and Multi-Path Component Identification on THz Channel Measurements in a Factory Environment", 18th European Conference on Antennas and Propagation (EuCAP), Glasgow, United Kingdom, 2024.

[i.108] Mildenhall, Ben, et al.: "Nerf: Representing scenes as neural radiance fields for view synthesis", Communications of the ACM 65, no. 1, 2021.

[i.109] Zhao, Xiaopeng, Zhenlin An, Qingrui Pan, and Lei Yang: "Nerf2: Neural radio-frequency radiance fields", In Proceedings of the 29th Annual International Conference on Mobile Computing and Networking, 2023.

[i.110] R. He, O. Renaudin, V.-M. Kolmonen, K. Haneda, Z. Zhong, B. Ai, S. Hubert, and C. Oestges: "Vehicle-to-vehicle radio channel characterization in crossroad scenarios", IEEE Transactions on Vehicular Technology, vol. 65, no. 8, 2015.

[i.111] S. Marano, W. M. Gifford, H. Wymeersch, and M. Z. Win: "Nlos identification and mitigation for localization based on uwb experimental data", IEEE Journal on selected areas in communications, vol. 28, no. 7, 2010.

[i.112] C. Huang, A. F. Molisch, R. He, R. Wang, P. Tang, B. Ai, and Z. Zhong: "Machine learning-enabled los/nlos identification for mimo systems in dynamic environments", IEEE Transactions on Wireless Communications, vol. 19, no. 6, 2020.

[i.113] C. Huang, A. F. Molisch, R. Wang, P. Tang, R. He, and Z. Zhong: "Angular information-based nlos/los identification for vehicle to vehicle mimo system", in 2019 IEEE International Conference on Communications Workshops (ICC Workshops). IEEE, 2019.

[i.114] M. Yang, B. Ai, R. He, C. Shen, M. Wen, C. Huang, J. Li, Z. Ma, L. Chen, X. Li et al.: "Machine-learning-based scenario identification using channel characteristics in intelligent vehicular communications", IEEE Transactions on Intelligent Transportation Systems, vol. 22, no. 7, 2020.

[i.115] I. M. AlHajri, T. A. Nazar and M.S. Raed: "Classification of indoor environments for IoT applications: A machine learning approach", IEEE Antennas and Wireless Propagation Letters 17.12 (2018).

[i.116] H. Cheng, S. Ma, and H. Lee: "CNN-Based mmWave Path Loss Modeling for Fixed Wireless Access in Suburban Scenarios", IEEE Antennas and Wireless Propagation Letters, vol. 19, no. 10, 2020.

[i.117] R. Levie, C¸. Yapar, G. Kutyniok, and G. Caire: "RadioUNet: Fast Radio Map Estimation With Convolutional Neural Networks", IEEE Transactions on Wireless Communications (TWC), vol. 20, no. 6, 2021.

[i.118] H. Ates, S. Hashir, T. Baykas, and B. Gunturk: "Path Loss Exponent and Shadowing Factor Prediction From Satellite Images Using Deep Learning", IEEE Access, vol. 7, pp. 101366-101375, 2019.

[i.119] X. Wang, Z. Zhang, D. He, K. Guan, D. Liu, J. Dou, S. Mumtaz, and S. AlRubaye: "A Multi - Task Learning Model for Super Resolution of Wireless Channel Characteristics", in 2022 IEEE Global Telecommunications Conference (GLOBECOM 2022). Rio de Janeiro, Brazil: IEEE, 12-2022, pp. 952-957.

[i.120] P. M. Ramya, M. Boban, C. Zhou, and S. Stanczak: "Using learning methods for V2V path loss prediction", in 2019 IEEE Wireless Communications and Networking Conference (WCNC).

[i.121] P. Dong, H. Zhang, G. Y. Li, N. NaderiAlizadeh, and I. S. Gaspar: "Deep CNN for Wideband Mmwave Massive Mimo Channel Estimation Using Frequency Correlation", in IEEE International Conference on Acoustics, Speech and Signal Processing (ICASSP 2019). Brighton, United Kingdom.

[i.122] J. Yuan, H. Q. Ngo, and M. Matthaiou: "Machine Learning-Based Channel Estimation in Massive MIMO with Channel Aging", in 20th IEEE International Workshop on Signal Processing Advances in Wireless Communications (SPAWC 2019). Cannes, France.

[i.123] H. Kim, S. Kim, H. Lee, C. Jang, Y. Choi, and J. Choi: "Massive MIMO Channel Prediction: Kalman Filtering Vs. Machine Learning", IEEE Transactions on Communications, vol. 69, no. 1, 2021.

[i.124] W. Jiang and H. D. Schotten: "Deep learning for fading channel prediction", IEEE Open Journal of the Communications Society, vol. 1, 2020.

[i.125] N. Czink, P. Cera, J. Salo, E. Bonek, J.-P. Nuutinen, and J. Ylitalo: "A Framework for Automatic Clustering of Parametric MIMO Channel Data Including Path Powers", in 64th IEEE Vehicular Technology Conference (VTC 2006). Montreal,´ Canada: IEEE, 9 2006, pp. 1-5.

[i.126] C. Gustafson, K. Haneda, S. Wyne, and F. Tufvesson: "On mm-Wave Multipath Clustering and Channel Modeling", IEEE Transactions on Antennas and Propagation, vol. 62, no. 3, pp. 1445-1455, 3 2014.

[i.127] C.-L. Cheng, S. Sangodoyin, and A. Zajic: "THz Cluster-Based Modeling and Propagation Characterization in a Data Centre Environment", IEEE Access, vol. 8, pp. 56544-56558, 3 2020.

[i.128] Y. Li, Y. Wang, Y. Chen, Z. Yu, and C. Han: "Channel Measurement and Analysis in an Indoor Corridor Scenario at 300 GHz", in 2022 IEEE International Conference on Communications (ICC 2022). Seoul, South Korea: IEEE, 05-2022.

[i.129] E. Martin, K. Hans-Peter, and X. Xiaowei: "A Density-Based Algorithm for Discovering Clusters in Large Spatial Databases with Noise", in Proceedings of the Second International Conference on Knowledge Discovery in Databases and Data Mining (KDD), Portland, OR, 8 1996, pp. 226-231.

[i.130] Y. Chen, Y. Li, C. Han, Z. Yu, and G. Wang: "Channel Measurement and Ray-Tracing-Statistical Hybrid Modeling for Low-Terahertz Indoor Communications", IEEE Transactions on Wireless Communications (TWC), vol. 20, no. 12, pp. 8163-8176, 12 2021.

[i.131] R. He, Q. Li, B. Ai, Y. L.-A. Geng, A. F. Molisch, V. Kristem, Z. Zhong, and J. Yu: "A Kernel-Power-Density-Based Algorithm for Channel Multipath Components Clustering", IEEE Transactions on Wireless Communications (TWC), vol. 16, no. 11, pp. 7138-7151, 11 2017.

[i.132] C. Schneider, M. Bauer, M. Narandzic, W. A. T. Kotterman, and R. S. Thomae: "Clustering of MIMO Channel Parameters - Performance Comparison", in 2009 69th IEEE Vehicular Technology Conference (VTC 2009-Spring). Barcelona, Spain: IEEE, 04-2009.

[i.133] C. Gentile: "Using the Kurtosis Measure to Identify Clusters in Wireless Channel Impulse Responses", IEEE Transactions on Antennas and Propagation, vol. 61, no. 6, pp. 3392-3395, June 2013.

[i.134] S. C. Zhu and A. Yuille: "Region competition: unifying snakes, region growing, and Bayes/MDL for multiband image segmentation", IEEE Transactions on Pattern Analysis and Machine Intelligence, vol. 18, no. 9, pp. 884-900, 1996.

[i.135] R. He, W. Chen, B. Ai, A. F. Molisch, W. Wang, Z. Zhong, J. Yu, and S. Sangodoyin: "On the Clustering of Radio Channel Impulse Responses Using Sparsity-Based Methods", IEEE Transactions on Antennas and Propagation, vol. 64, no. 6, pp. 2465-2474, 6 2016.

[i.136] R. Piesiewicz et al.: "Scattering analysis for the modeling of THz communication systems", IEEE Transactions on Antennas and Propagation, vol. 55, no. 11, pp. 3002-3009, 2007.

[i.137] Alissa M., Friederich B., Sheikh F., et al.: "Experimental investigation of terahertz scattering: a study of non-Gaussianity and lateral roughness influence", IEEE Access, 2020, 8: 170672-170680.

[i.138] Budiarto H., Horihata K., Haneda K., et al.: "Experimental study of non-specular wave scattering from building surface roughness for the mobile propagation modeling". IEICE transactions on Communications, 2004, 87(4): 958-966.

[i.139] Sheikh F., Zantah Y., Mabrouk I. B., et al.: "Scattering and roughness analysis of indoor materials at frequencies from 750 GHz to 1.1 THz". IEEE Transactions on Antennas and Propagation, 2021, 69(11): 7820-7829.

[i.140] B. Ji et al.: "Several key technologies for 6G: Challenges and opportunities", IEEE Communications Standards Magazine, vol. 5, no. 2, pp. 44-51, 2021.

[i.141] M. Inomata et al.: "Terahertz propagation characteristics for 6G mobile communication systems", in 2021 15th European Conference on Antennas and Propagation (EuCAP), 2021, pp. 1-5.

[i.142] M. Mrnka: "Random gaussian rough surfaces for full-wave electromagnetic simulations", Conference on Microwave Techniques (COMITE), Brno, Czech Republic, 2017, pp. 1-4, doi: 10.1109/COMITE.2017.7932310.

[i.143] M. Alissa, F. Sheikh, A. A. -h. Abbas and T. Kaiser: "Wave Scattering from Non-Gaussian Rough Surfaces at Terahertz Frequencies", Second International Workshop on Mobile Terahertz Systems (IWMTS), Bad Neuenahr, Germany, 2019, pp. 1-5.

[i.144] H. Yi et al.: "Full-Wave Simulation and Scattering Modeling for Terahertz Communications", in IEEE Journal of Selected Topics in Signal Processing, vol. 17, no. 4, pp. 713-728, July 2023, doi: 10.1109/JSTSP.2023.3285099.

[i.145] Warnick, K. F., & Chew, W. C. (2001): "Numerical simulation methods for rough surface scattering". Waves in Random Media, 11(1), R1-R30. https://doi.org/10.1088/0959-7174/11/1/201.

[i.146] Harrington R F. Field: "Computation by Moment Method". New York: Macmillan Company, 1968.

[i.147] B. Dembart and E. Yip: "The accuracy of fast multipole methods for Maxwell's equations," in IEEE Computational Science and Engineering, vol. 5, no. 3, pp. 48-56, July-September 1998, doi: 10.1109/99.714593.

[i.148] H. Yu: "The Multilevel Fast Multipole Method and its application", 2011 International Conference on Multimedia Technology, Hangzhou, China, 2011, pp. 3743-3745, doi: 10.1109/ICMT.2011.6002213.

[i.149] Humphries, Stanley: "Finite-element methods for electromagnetics", New Mexico, January (2010).

[i.150] Kunz, Karl S., and Raymond J. Luebbers: "The finite difference time domain method for electromagnetics", CRC press, 1993.

[i.151] Li, Juan, et al.: "Message-passing-interface-based parallel FDTD investigation on the EM scattering from a 1-D rough sea surface using uniaxial perfectly matched layer absorbing boundary", JOSA A 26.6 (2009): 1494-1502.

[i.152] Krakiwsky, Sean E., Laurence E. Turner, and Michal M. Okoniewski: "Acceleration of finite-difference time-domain (FDTD) using graphics processor units (GPU)", 2004 IEEE MTT-S International Microwave Symposium Digest (IEEE Cat. No. 04CH37535). Vol. 2. IEEE, 2004.

[i.153] L. Xiao, X. -H. Wang, B. -Z. Wang, G. Zheng and P. Chen: "An Efficient Hybrid Method of Iterative MoM-PO and Equivalent Dipole-Moment for Scattering From Electrically Large Objects", in IEEE Antennas and Wireless Propagation Letters, vol. 16, pp. 1723-1726, 2017, doi: 10.1109/LAWP.2017.2669910.

[i.154] Elfouhaily, Tanos Mikhael, and Charles-Antoine Guérin: "A critical survey of approximate scattering wave theories from random rough surfaces", Waves in random media 14.4 (2004): R1.

[i.155] Beckmann P. and Spizzichino A. (1963): "The Scattering of Electromagnetic Waves from Rough Surfaces" (Oxford: Pergamon).

[i.156] Voronovich A G (1994): "Small-slope approximation for electromagnetic wave scattering at a rough interface of two dielectric half-spaces", Waves Random Media 4 337-67.

[i.157] S. Afifi, R. Dusséaux and A. Berrouk: "Electromagnetic Scattering From 3D Layered Structures With Randomly Rough Interfaces: Analysis With the Small Perturbation Method and the Small Slope Approximation", in IEEE Transactions on Antennas and Propagation, vol. 62, no. 10, pp. 5200-5208, Oct. 2014, doi: 10.1109/TAP.2014.2341704.

[i.158] Wentz F J.: "A two-scale scattering model for foam-free sea microwave brightness temperatures", Journal of Geophysical Research, 1975, 80(24): 3441-3446.

[i.159] D. W. Eaton: "Backscattering from spherical elastic inclusions and accuracy of the Kirchhoff approximation for curved interfaces", in Geophysical Journal International, vol. 166, no. 3, pp. 1249-1258, September 2006, doi: 10.1111/j.1365-246X.2006.03047.x.

[i.160] F. Zhengguang, W. Rui, Z. Yanchun and L. Wei: "Estimation of Ground Scattering Coefficient Based on Small Perturbation Method", 2021 13th International Symposium on Antennas, Propagation and EM Theory (ISAPE), Zhuhai, China, 2021, pp. 1-2, doi: 10.1109/ISAPE54070.2021.9753509.

[i.161] D. He, B. Ai, K. Guan, L. Wang, Z. Zhong and T. Kürner: "The Design and Applications of High-Performance Ray-Tracing Simulation Platform for 5G and Beyond Wireless Communications: A Tutorial", in IEEE Communications Surveys & Tutorials, vol. 21, no. 1, pp. 10-27, Firstquarter 2019, doi: 10.1109/COMST.2018.2865724.

[i.162] V. Degli-Esposti, F. Fuschini, E. M. Vitucci and G. Falciasecca: "Measurement and Modelling of Scattering From Buildings", in IEEE Transactions on Antennas and Propagation, vol. 55, no. 1, pp. 143-153, Jan. 2007, doi: 10.1109/TAP.2006.888422.

[i.163] B. Chen et al.: "A 3D Modeling Method for Scattering on Rough Surfaces at the Terahertz Band", GLOBECOM 2023 - 2023 IEEE Global Communications Conference, Kuala Lumpur, Malaysia, 2023, pp. 764-769, doi: 10.1109/GLOBECOM54140.2023.10437063.

[i.164] J. Guo, Y. Li, S. Cai and D. Su: "Fast Prediction of Electromagnetic Scattering Characteristics of Targets Based on Deep Learning", 2021 International Applied Computational Electromagnetics Society (ACES-China) Symposium, Chengdu, China, 2021, pp. 1-2, doi: 10.23919/ACES-China52398.2021.9581613.

[i.165] Z. Zhang et al.: "A Deep Learning Based Surface Current Generation Method for Scattering Modeling at Terahertz Band", 2024 18th European Conference on Antennas and Propagation (EuCAP), Glasgow, United Kingdom, 2024, pp. 1-5, doi: 10.23919/EuCAP60739.2024.10501597.

[i.166] L. Wei, C. Huang et al.: "Tri-Polarized Holographic MIMO Surfaces for Near-Field Communications: Channel Modeling and Precoding Design", IEEE Transactions on Wireless Communications, 2023.

[i.167] S. Priebe, M. Jacob, C. Jansen and T. Kürner: "Non-specular scattering modeling for THz propagation simulations", Proceedings of the 5th European Conference on Antennas and Propagation (EUCAP), Rome, Italy, 2011, pp. 1-5.

[i.168] T. Kurner, D. Mittleman, and T. Nagatsuma: "THz Communciations paving the way toward 1 Tbps". Springer, 2020.

[i.169] V. Degli-Esposti, M. Zoli, E. M. Vitucci, F. Fuschini, M. Barbiroli and J. Chen: "A Method for the Electromagnetic Characterization of Construction Materials Based on Fabry-Pérot Resonance", in IEEE Access, vol. 5, pp. 24938-24943, 2017, doi: 10.1109/ACCESS.2017.2767278.

[i.170] M. Jacob, T. Kürner, R. Geise and R. Piesiewicz: "Reflection and transmission properties of building materials in D-band for modeling future mm-wave communication systems", Proceedings of the Fourth European Conference on Antennas and Propagation, Barcelona, Spain, 2010, pp. 1-5.

[i.171] A. Fricke, S. Rey, M. Achir, P. Le Bars, T. Kleine-Ostmann and T. Kürner: "Reflection and transmission properties of plastic materials at THz frequencies", 2013 38th International Conference on Infrared, Millimetre, and Terahertz Waves (IRMMW-THz), Mainz, Germany, 2013, pp. 1-2, doi: 10.1109/IRMMW-THz.2013.6665413.

[i.172] A. Fricke, T. Kürner, M. Achir and P. Le Bars: "A model for the reflection of terahertz signals from printed circuit board surfaces", 2017 11th European Conference on Antennas and Propagation (EUCAP), Paris, France, 2017, pp. 711-715, doi: 10.23919/EuCAP.2017.7928148.

[i.173] Piesiewicz, R., Jansen, C., Wietzke, S. et al.: "Properties of Building and Plastic Materials in the THz Range". Int J Infrared Milli Waves 28, 363-371 (2007). doi: 10.1007/s10762-007-9217-9.

[i.174] ETSI GR RIS 003 (V1.1.1): "Reconfigurable Intelligent Surfaces (RIS); Communication Models, Channel Models, Channel Estimation and Evaluation Methodology", June 2023.

[i.175] Chian, De-Ming, Chao-Kai Wen, Chi-Hung Wu, Fu-Kang Wang, and Kai-Kit Wong: "A novel channel model for reconfigurable intelligent surfaces with consideration of polarization and switch impairments", arXiv preprint arXiv:2304.03713, 2023.

[i.176] C. A. Balanis: "Advanced Engineering Electromagnetics". Hoboken, NJ, USA: Wiley, 2012. 2nd edition.

[i.177] E. Bjornson, O. T. Demir, and L. Sanguinetti: "A primer on near-field beamforming for arrays and reconfigurable intelligent surfaces", CoRR, vol. abs/2110.06661, 2021.

[i.178] Quadriga Version: 2.8.1, accessed June 2024.

[i.179] Yu Han, Shi Jin, Chao-Kai Wen, and Xiaoli Ma: "Channel Estimation for Extremely Large-Scale Massive MIMO Systems", IEEE Wireless Communications Letters, vol. 9, no. 5, May 2020.

[i.180] 3GPP RP-234069, RAN #102 meeting, December 2023.

[i.181] 3GPP TR 37.885: "Study on evaluation methodology of new Vehicle-to-Everything (V2X) use cases for LTE and NR".

[i.182] 3GPP TR 36.777: "Enhanced LTE support for aerial vehicles".

[i.183] Asia Pacific Telecommunity: "Draft APT Recommendation on Model(s) for FWS Link Performance Degradation due to Wind", The 29th Meeting of the APT Wireless Group, March 2022.

[i.184] T. Kawanishi: "Millimetre-wave and THz links under severe weather condition", 2020 International Symposium on Antennas and Propagation (ISAP), Osaka, Japan, 2021, pp. 661-662, doi: 10.23919/ISAP47053.2021.9391156.

[i.185] Z. -K. Weng, K. Inagaki, P. T. Dat, A. Kanno, T. Kawanishi and K. Akahane: "Antenna Effective Gain Estimation under Windy Condition in Terahertz Fixed Wireless Systems", 2023 IEEE Conference on Antenna Measurements and Applications (CAMA), Genoa, Italy, 2023, pp. 271-272, doi: 10.1109/CAMA57522.2023.10352721.

[i.186] J. S. Ward: "Phase Noise Induced by a Vibrating Antenna", in IEEE Transactions on Microwave Theory and Techniques, vol. 65, no. 11, pp. 4148-4153, Nov. 2017, doi: 10.1109/TMTT.2017.2699682.

[i.187] K. A. Al Mallak, M. Nair, G. Hilton, T. H. Loh and M. Beach: "Characterisation of Horizontally Induced Vibrations on Antenna's Channel Response at Millimetre-Wave", 2022 18th International Conference on Wireless and Mobile Computing, Networking and Communications (WiMob), Thessaloniki, Greece, 2022, pp. 166-171, doi: 10.1109/WiMob55322.2022.9941362.

[i.188] J. Blumenstein, J. Vychodil, M. Pospisil, T. Mikulasek and A. Prokes: "Effects of vehicle vibrations on mm-wave channel: Doppler spread and correlative channel sounding", 2016 IEEE 27th Annual International Symposium on Personal, Indoor, and Mobile Radio Communications (PIMRC), Valencia, Spain, 2016, pp. 1-5, doi: 10.1109/PIMRC.2016.7794619.

[i.189] M. Soliman, Y. Dawoud, E. Staudinger, S. Sand, A. Schuetz and A. Dekorsy: "Influences of train wagon vibrations on the mmwave wagon-to-wagon channel", 12th European Conference on Antennas and Propagation (EuCAP 2018), London, UK, 2018, pp. 1-5, doi: 10.1049/cp.2018.0962.

[i.190] E. N. Papasotiriou, A. -A. A. Boulogeorgos and A. Alexiou: "Performance Analysis of THz Wireless Systems in the Presence of Antenna Misalignment and Phase Noise", in IEEE Communications Letters, vol. 24, no. 6, pp. 1211-1215, June 2020, doi: 10.1109/LCOMM.2020.2981336.

[i.191] M. Heino, C. Icheln and K. Haneda: "Self-user shadowing effects of millimetre-wave mobile phone antennas in a browsing mode", 2019 13th European Conference on Antennas and Propagation (EuCAP), Krakow, Poland, 2019, pp. 1-5.

[i.192] P. Bhardwaj and S. M. Zafaruddin: "On the Performance of Multihop THz Wireless System Over Mixed Channel Fading With Shadowing and Antenna Misalignment", in IEEE Transactions on Communications, vol. 70, no. 11, pp. 7748-7763, Nov. 2022, doi: 10.1109/TCOMM.2022.3205657.

[i.193] R. Tanski et al.: "Sub-THz Wireless Channel Field Measurements: A Study at 140 GHz", 2022 IEEE Globecom Workshops (GC Wkshps), Rio de Janeiro, Brazil, 2022, pp. 1790-1795, doi: 10.1109/GCWkshps56602.2022.10008496.

[i.194] Agneessens, S. (2023, March 23): "Sway compensation antennas, your E-band friend, with benefits", Ericsson.

[i.195] Kedar, D., & Arnon, S. (2004): "Urban optical wireless communication networks: the main challenges and possible solutions". IEEE Communications Magazine, 42(5), S2-S7.

[i.196] L. Fuhrmann, O. Biallawons, J. Klare, R. Panhuber, R. Klenke and J. Ender: "Micro-Doppler analysis and classification of UAVs at Ka band", 2017 18th International Radar Symposium (IRS), Prague, Czech Republic, 2017, pp. 1-9, doi: 10.23919/IRS.2017.8008142.

[i.197] S. Zhang, G. Li, M. Ritchie, F. Fioranelli and H. Griffiths: "Dynamic hand gesture classification based on radar micro-Doppler signatures", 2016 CIE International Conference on Radar (RADAR), Guangzhou, China, 2016, pp. 1-4, doi: 10.1109/RADAR.2016.8059518.

[i.198] Tahmoush, D. (2015): "Review of micro-Doppler signatures". IET Radar Sonar Navig., 9: 1140-1146. doi: 10.1049/iet-rsn.2015.0118.

[i.199] Kokkoniemi, J., Boulogeorgos, A. A. A., Aminu, M., Lehtomäki, J., Alexiou, A., & Juntti, M. (2020): "Impact of beam misalignment on THz wireless systems", Nano Communication Networks, 24, 100302.

3 Definition of terms, symbols and abbreviations

3.1 Terms

Void.

3.2 Symbols

Void.

3.3 Abbreviations

For the purposes of the present document, the following abbreviations apply:

AGV	Automated Guided Vehicle
AI	Artificial Intelligence
AoA	Angle of Arrival
AoD	Angle of Departure
AP	Access Point
AR	Augmented Reality
AS	Angular Spread
BS	Base Station
CV	Computer Vision
D2D	Device to Device
DL	DownLink
DS	Delay Spread
HLS	High Layer Split
IoT	Internet of Things
ISAC	Integrated Sensing And Communications
KPI	Key Performance Indicator
LLS	Low Layer Split
LoS	Line of Sight
LSP	Large Scale Parameter
MIMO	Multiple-Input and Multiple-Output
ML	Machine Learning
MPC	MultiPath Component
MR	Mixed Reality
NLoS	Non-Line of Sight
NTN	Non-Terrestrial Networks
OAM	Orbital Angular Moment
OFDM	Orthogonal Frequency-Division Multiplexing
OLoS	Obstructed Line of Sight
OOB	Out-Of-Band
PL	Path Loss
QoS	Quality of Service
RAT	Radio Access Technology
RCS	Radar Cross-Section
RF	Radio Frequency
RIS	Reconfigurable Intelligent Surface
RMS	Root Mean Square
RX	Receiver
SDN	Software Defined Networks
SF	Shadow Fading
SLAM	Simultaneous Localization And Mapping
SNR	Signal to Noise Ratio
SSP	Small Scale Parameter
T2I	Train to Infrastructure
T2T	Train-to-Train
TCC	Train Control Centre
THz	TeraHertz
TX	Transmitter
UAV	Unmanned Air Vehicle
UE	User Equipment
UL	UpLink
V2V	Vehicle-to-Vehicle
V2X	Vehicle-to-everything
VR	Virtual Reality
XR	Extended Reality

4 Channel measurement scenarios and frequency bands

4.1 Channel measurement scenarios

4.1.1 Identified THz use cases and physical environments

ETSI GR THz 001 [i.69] generated by the ETSI ISG THz work item on Identification of use cases for THz communication systems identified 19 use cases either enabled by or highly benefiting from the use of THz communications:

- Remote surgery
- In airplane or train cabin entertainment
- Cooperative mobile robots
- Hazardous material work
- Remote education
- Fixed point to point wireless applications
- Mobile wireless X-haul transport
- Wireless data centres
- Interactive immersive XR
- Mission critical XR
- Real-time industrial control
- Simultaneous imaging, mapping and localization
- Commissioning of industrial plants
- Grand events with ultra-high throughput
- Ultra-high throughput for indoor users
- Intra-device communications
- Local area collaboration for fixed or low mobility applications
- Local area collaboration for vehicular applications
- Predictive maintenance and diagnostics

For each identified use case, ETSI GR THz 001 [i.69] provided the description of the physical environment, including propagation aspects, range, and mobility. The physical environments corresponding to the identified use cases are falling into one or more of the following categories:

- Indoor:
    - On-body
    - Medical facilities
    - Living room
    - Airplane cabin

- Train cabin
- Factory
- Classroom
- Data centre
- Hallway
- Meeting room
- Office
- Intra-machine/device

- Outdoor:
  - Open space
  - Highway
  - Urban street
  - Urban canyon
  - Stadium
  - Square

4.1.2 Mapping the identified use cases and deployment scenarios to relevant channel measurements scenarios

A mapping of the identified use cases and deployment scenarios to relevant channel measurements scenarios was provided in [i.69]. In order to support the evaluation of the identified use cases through simulations, one necessary component is the definition of channel models for THz communications and sensing in the environments where the use case will be deployed. To that end, each use case described in [i.69] contains the description of the target physical environment. Table 1 below summarizes each of the physical environments, classifies them into two groups (indoor and outdoor), and indicates related THz channel measurement studies available in the existing literature for that particular environment. The aim of the present document is to provide channel measurements and models for the physical environments identified in Table 1. In addition, other typical indoor environments as specified in Recommendation ITU-R 1238 [i.70], such as conference room, corridors, railway stations, airport terminals and commercial environments and outdoor environments as specified in Recommendation ITU-R 1411 [i.71], including residential, urban and suburban will be considered for typical deployment scenarios.

Table 1: Mapping the identified use cases and deployment scenarios to relevant channel measurements scenarios

Physical environment / Use case	Indoor													Outdoor					
	On-body	Medical facility	Living room	Airplane cabin	Train cabin	Factory	Classroom	Data centre	Hallway	Meeting room	Office	Intra-machine/ device	Inter-machine	Open space	Highway	Urban street	Urban canyon	Stadium	Square
Remote surgery	Y	Y	Y																
In airplane / train cabin entertainment				Y	Y														
Cooperative mobile robots						Y													
Hazardous material work						Y													
Remote education							Y												
Fixed wireless X-haul transport														Y	Y	Y	Y	Y	Y
Mobile wireless X-haul transport														Y	Y	Y	Y		
Wireless data centres								Y											
Interactive immersive XR			Y								Y								
Mission critical XR		Y	Y			Y	Y	Y			Y			Y		Y	Y	Y	Y
Real-time industrial control						Y						Y	Y						
Simultaneous imaging, mapping, and localization			Y				Y		Y	Y	Y							Y	Y
Commissioning of industrial plants						Y													
Grand Events with Ultra-High Throughput																		Y	Y
Ultra-high throughput for indoor users			Y				Y		Y	Y	Y								
Intra-device communications												Y							
Local area collaboration for fixed/low mobility applications	Y	Y	Y			Y	Y		Y	Y	Y			Y				Y	Y

Physical environment / Use case	Indoor													Outdoor					
	On-body	Medical facility	Living room	Airplane cabin	Train cabin	Factory	Classroom	Data centre	Hallway	Meeting room	Office	Intra-machine/ device	Inter-machine	Open space	Highway	Urban street	Urban canyon	Stadium	Square
Local area collaboration with mobility														Y	Y	Y	Y		
Predictive maintenance and diagnostics						Y													
Related measurement study				[i.31] [i.63] [i.66] [i.74]	[i.31] [i.34] [i.37] [i.38] [i.61]	[i.56]	[i.61]	[i.25] [i.26] [i.27] [i.28] [i.42] [i.43] [i.61]	[i.6] [i.49] [i.50] [i.53] [i.61]	[i.5] [i.7] [i.30] [i.33] [i.36] [i.44] [i.45] [i.46] [i.60] [i.61] [i.66]	[i.8] [i.10] [i.17] [i.21] [i.47] [i.48] [i.55]	[i.11] [i.13] [i.15] [i.16] [i.18] [i.25] [i.32] [i.64] [i.66]	[i.68]	[i.22] [i.23] [i.24] [i.40] [i.61]	[i.29] [i.57] [i.58] [i.59]	[i.40] [i.51] [i.52] [i.57] [i.58] [i.59] [i.61]	[i.40] [i.51] [i.52] [i.61]		
NOTE: The following generic references apply to all use cases: [i.4], [i.9], [i.12], [i.14], [i.19], [i.20], [i.35], [i.66].																			

As can be seen from Table 1, channel measurements for most of the physical environments identified by the ISG THz are reported in the literature. However, for some environments and certain scenarios, measurements are still lacking or are under-explored, such as for:

- indoor: on-body, medical, factories, classroom, living room and inter-machine;
- outdoor: stadium and square;
- mobile environments.

Furthermore, while channel models for THz bands are available, they do not cover all of the use cases and physical environments identified in [i.69]. It was therefore recommended to perform channel measurements and develop channel models in the THz bands for the identified use cases with typical deployment scenarios for both indoor and outdoor environments within the scope of the present document.

4.2 Frequency bands

4.2.1 Introduction

The frequency range 100 GHz to 10 THz is referred to as the 'THz range', as shown in Figure 1. The corresponding wavelengths are from 0,03 mm to 3 mm. Below this range, the mm-wave and microwave frequency ranges are found, already heavily utilized for communications and non-communications applications. Above 10 THz the near- and mid-infrared spectrum starts.

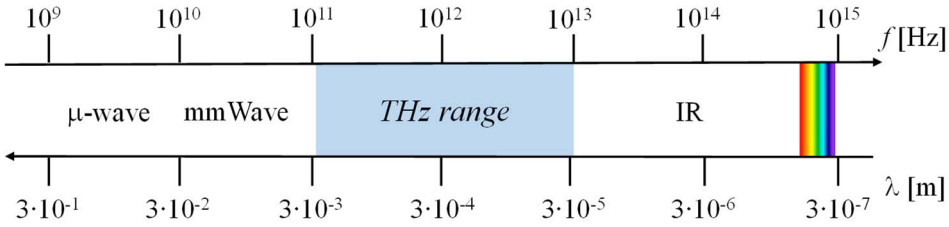

Figure 1: Position of the THz band in the radio spectrum

As discussed in detail in [i.72], the frequency ranges from 100 GHz and upwards are already utilized for non-communications purposes, and therefore there is a need to understand the regulatory landscape and identify the most interesting frequency bands for THz communications. The frequency range from 100 GHz to 3 THz is regulated by the ITU-R Radio Regulations (RR) [i.73], but on different levels. As shown in Figure 2, frequency allocations exist, which is the strictest type of global spectrum regulations, up to 275 GHz. Further, the range between 275 and 450 GHz is identified for fixed and mobile services. In this range, and further up to 1 THz, several bands are also identified for so-called passive services. In some of the bands in this range, specific conditions to ensure protection of the passive services exist. Above 1 THz up to 3 THz, the whole spectrum can be used freely for both active and passive services, while above 3 THz, no regulations exist.

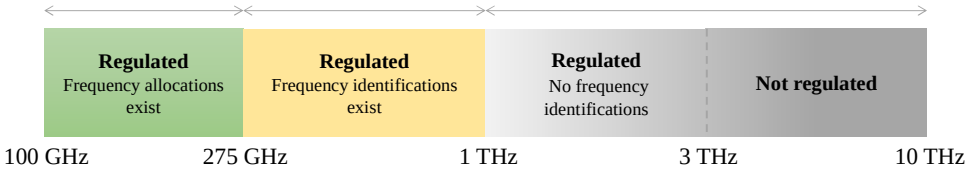

Figure 2:Frequency ranges within the THz band with different regulatory status

Between 100 and 275 GHz, 8 bands with sufficient contiguous bandwidths are allocated to FIXED and MOBILE services on a co-primary basis, constituting 90,7 GHz bandwidth in total. Above 275 GHz, interesting bands have been identified for THz communications purposes based on a combination of regulatory status and favourable propagation conditions. A new concept of transmission windows is defined (as explained in Annex A) to help in identifying the interesting frequencies above 275 GHz. The resulting analysis yielded 12 bands of interest constituting 488 GHz of bandwidth. 91 GHz of this range is identified for fixed and mobile services.

4.2.2 Mapping the identified frequency bands and physical environments to relevant channel measurements and modelling scenarios

To support the development of channel models for the frequency bands defined in [i.72], Table 2 below summarizes each of the physical environments, classifies them into frequency bands and indicates related THz channel measurement studies available in the existing literature for that particular environment. In order to group the available literature, a less fine-granular classification is used than in [i.72]. Furthermore, the present document aims to provide channel measurements and models for the physical environments identified in Table 2. In addition, other typical indoor environments as specified in Recommendation ITU-R P.1238 [i.70], such as conference room, corridors, railway stations, airport terminals and commercial environments and outdoor environments as specified in Recommendation ITU-R P.1411 [i.71], including residential, urban and suburban may be considered for typical deployment scenarios.

Table 2: Mapping the identified frequency bands and physical environments to relevant channel measurements and modelling scenarios

Physical environment / Frequency Range in GHz	Indoor													Outdoor						
	On-body	Medical facility	Living room	Airplane cabin	Train cabin	Factory	Classroom	Data centre	Hallway	Meeting room	Office	Intra-machine/device	Inter-machine	Open space	Highway	Urban street	Urban canyon	Stadium	Square	Relevant to all Scenarios
100 - 175						[i.75]			[i.6]	[i.5] [i.7] [i.33]	[i.52] [i.55] [i.67]			[i.22] [i.23] [i.24] [i.35]		[i.54]	[i.39] [i.62] [i.52]			[i.14]
175 - 250														[i.22] [i.23] [i.24]						
250 - 350				[i.52] [i.66]	[i.31] [i.34] [i.38]			[i.25] [i.26] [i.27] [i.28] [i.43]	[i.44] [i.45] [i.54] [i.55]	[i.50] [i.60] [i.68]	[i.8] [i.10] [i.17] [i.30] [i.41] [i.53]	[i.11] [i.13] [i.15] [i.16] [i.19] [i.21] [i.32] [i.66] [i.67]		[i.22] [i.23] [i.24] [i.61]	[i.29] [i.62]	[i.40] [i.75]	[i.40]			[i.4] [i.9] [i.12] [i.14] [i.18] [i.20] [i.65]
Beyond 350														[i.22] [i.23] [i.24]						

5 THz-specific radio propagation aspects

5.1 Atmospheric effects

5.1.0 Introduction

As denoted in clause 4.2.1, 'THz range', also known as sub-millimetre waves, refers to the frequency range between 100 GHz and 10 THz, and particularly the spectrum range between 275 GHz and 450 GHz is identified for fixed and mobile services. One of the distinct characteristics of the THz range is that its radio propagation channel is susceptible to atmospheric conditions, especially water molecules, as water molecules mainly absorb and scatter the wave propagation energy at this frequency, which in turn impedes its wave propagation and thus the wireless communication. These natural characteristics of wave propagation in the THz range should be thoroughly characterized to enable the use of wireless communication, especially for the cases of outdoor application scenarios. In [i.25], three main influential atmospheric effects contributing to wave propagation have been identified: gaseous attenuation due to oxygen and water vapour, rain attenuation, and clouds and fogs attenuation.

5.1.1 Gaseous attenuation due to oxygen and water vapour

In Recommendation ITU-R P.676-12 [i.22], the effect of oxygen and water vapour absorption on wave propagation at frequencies from 1 GHz up to 1 000 GHz is identified encompassing the consideration of the individual spectral lines from oxygen and water vapour, together with the impact of pressure-induced nitrogen attenuation above 100 GHz and a wet continuum. The specific attenuation due to oxygen and water vapour can be accurately evaluated based on the line-by-line calculation using spectroscopic data for oxygen and water vapour and is given by:

$$\gamma = \gamma_o + \gamma_w = 0{,}1820 f\left(N''_{Oxygen}(f) + N''_{Water\ Vapour}(f)\right)$$

Where γ_o and γ_w represent the specific attenuations (dB/km) due to dry air (oxygen and pressure-induced nitrogen) and water vapour. $N''_{Oxygen}(f)$ and $N''_{Water\ Vapour}(f)$ are the imaginary parts of the frequency dependent complex retroactivities indicating the impact of spectral lines for oxygen and water vapour for specific frequencies and the dry continuum due to pressure-induced nitrogen absorption above 100 GHz. The corresponding values can be calculated by employing the mathematical expressions provided in [i.22], exploiting frequency-dependent spectroscopic data for oxygen and water vapour attenuation given in the same document.

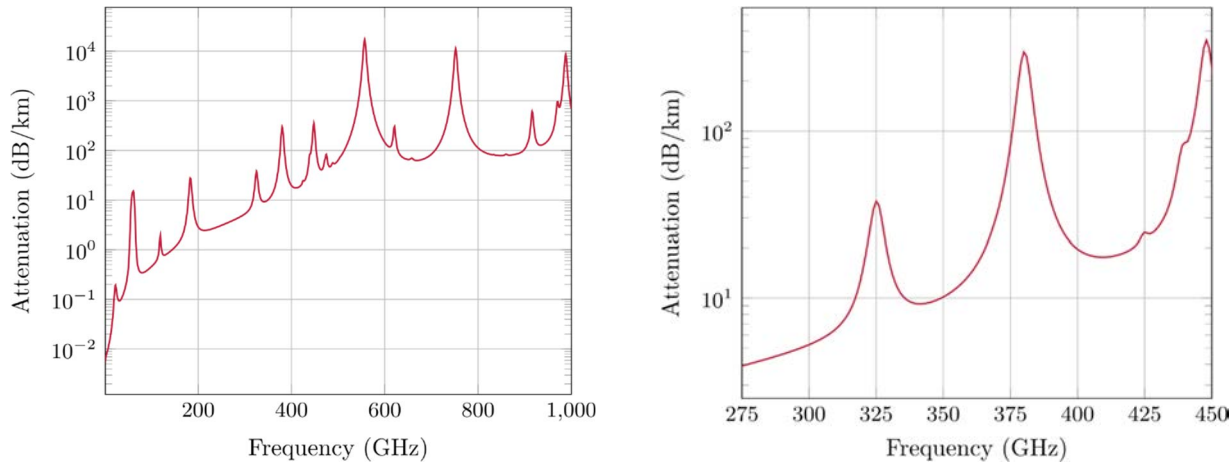

NOTE: Frequency range between 1 GHz to 1 000 GHz (left) and 275 GHz to 450 GHz identified for fixed and mobile services (right).

Figure 3: Frequency-dependent gaseous attenuation due to oxygen and water vapour with the granularity of 1 GHz for an air pressure of 1 013,25 hPa, temperature of 15 °C, a water vapour density of 7,5

In particular, the ITU approach can be computationally complex due to the fact that the ITU calculation is generated from the numerous concatenated equations including tables containing a wide range of information that provide a line-shape function and broadening factors that are applied to each absorption line for any known pressure, temperature, and water vapour height profile.

Instead, [i.102] introduces a simplified model developed to predict the molecular absorption loss for 275 GHz to 400 GHz frequency range without a need to implement complex absorption models and obtaining values from the HITRAN databases that provides detailed information about molecular absorption line including both weaker absorption lines and lines distributed over a much broader frequency space [i.101].

The simplified model shows sufficiently agreeable accuracy showing negligible error below one kilometre link distance and can be easily extended to any frequency bands. This is particularly important for standardization of propagation channel modelling, which is necessary to characterize absorption loss due to molecules such as water, carbon dioxide, nitrous oxide, carbon monoxide, methane, and oxygen in a simple way.

$$\alpha(f) = a_o \exp[b_o(f - f_0)] + c_o \left[\frac{\mathrm{dB}}{\mathrm{m}}\right]$$

where a_o, b_o, and c_o are the fitting parameters, f_0 in GHz is the break-point frequency. Within the specific frequency range, the absorption coefficient is fitted with an exponential function. Default reference pressure of 1 013,25 hPa, temperature of 20 °C, and relative humidity of 50 % are assumed in the parameterization of the piece-wise function given in Table 3. It is noted that the simplified model enables easy to calculate frequency dependency of the specific attenuation between 100 GHz and 448 GHz and it is intended only for performance evaluations in default conditions. If other atmospheric conditions are of importance it is recommended to use HITRAN or ITU-R models.

Table 3: Frequency dependent parameters for the characterization of molecular absorption attenuation

Frequency range [GHz]	[GHz]	a_o	b_o	c_o
[100, 119]	119	0,0472	0,5778	0,0040
(119, 129]	129	0,0001	-0,5820	0,0066
(129, 183]	183	0,7136	0,2640	0,0114
(183, 224]	224	0,00005	-0,2345	0,0239
(224, 325]	325	0,9355	0,2186	0,0239
(325, 342]	342	0,0034	-0,3374	0,1320
(342, 380]	380	7,8736	0,2642	0,1696
(380, 411]	411	0,0034	-0,2499	0,2615
(411, 448]	448	9,1267	0,2232	0,3105

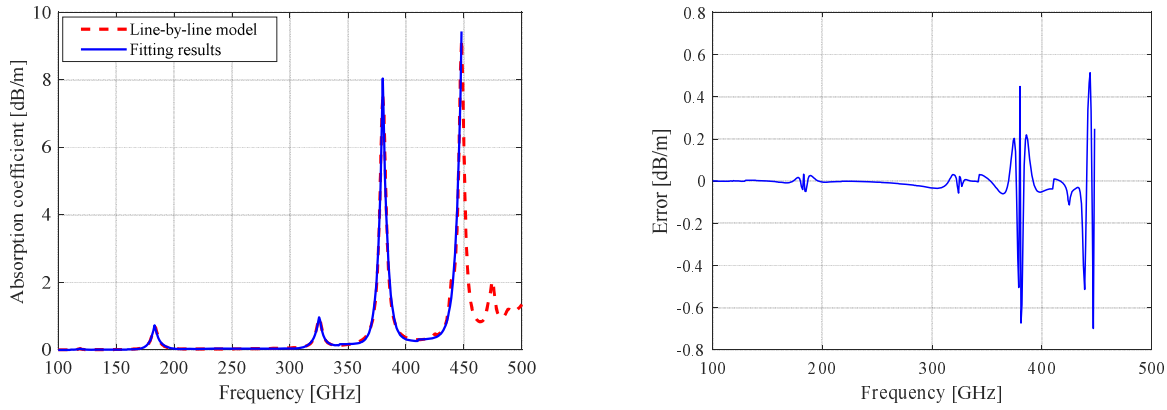

Figure 4: Fitting results with piecewise functions (left) and fitting error (right)

To extend the integration of the molecular absorption loss in wideband channel, firstly the time-domain channel impulse response of each path is transformed into frequency-domain channel transfer function, and apply the proposed simplified model of molecular absorption loss to the channel's frequency-domain channel transfer function at each frequency point of $f_c + \Delta f$ within the considered frequency range $[f_c - B/2, f_c + B/2]$, where B is the bandwidth. In turn, the molecular absorption loss for the n-path at the frequency of $f_c + \Delta f$ is modelled as:

$$L_n^{\text{molecular}}(f_c + \Delta f) = \alpha(f_c + \Delta f)c\tau_n$$

where c the speed of light, τ_n is the absolutely propagation delay of the n-path, and $\alpha(\cdot)$ is the absorption coefficient obtained from the simplified model.

Then, the frequency-domain channel transfer function of the multipath channel is obtained by the summation of frequency-domain channel transfer functions of all paths. Finally, the time-domain channel impulse response can be obtained by the reverse Fourier transform from the obtained frequency-domain channel transfer function.

5.1.2 Rain attenuation due to droplets

Recommendation ITU-R P.838-3 [i.23] identifies the effect of rain on wave propagation at frequencies from 1 GHz up to 1 000 GHz using the power-law relationship between the specific attenuation and the rain rate and the effect of rain is given by:

$$\gamma_R = \kappa R^{\alpha}$$

Where R is the rain rate (mm/h), κ and α are the frequency-dependent coefficients based on the curve-fitting to power-law coefficients derived from scattering calculations for both horizontal and vertical polarization.

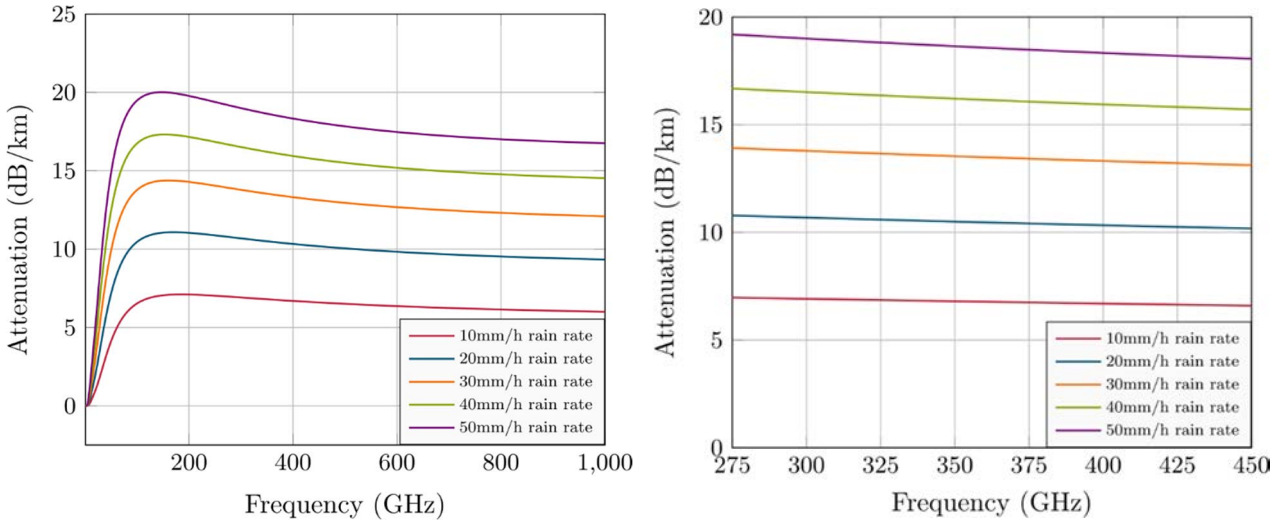

NOTE: Frequency range between 1 GHz to 1 000 GHz (left) and 275 GHz to 450 GHz identified for fixed and mobile services (right).

Figure 5: Frequency-dependent rain attenuation for straight path (same height level for both TX and RX) considering the rain rate between 10 mm/h and 50 mm/h with the granularity of 10 mm/h

The frequency dependent rain attenuation for straight path demonstrates a sharp increase below 100 GHz and a very gradual decrease with frequency in the region above 200 GHz after reach the peak. In particular, for short range communication between 275 GHz and 450 GHz, the effect of rain attenuation in a broadband channel can potentially be assumed as transmission at a single centre frequency rather than considering its effect separately across the wider bandwidth, which can reduce the computational effort. The historical mid-term rainfall data for Hannover over a 25-year period from 1995 to 2020 analysed in [i.103] provides supporting evidence that consideration of rain effect in a single frequency-domain is viable in certain circumstances as it shows that 99,9 % of the rainfall remains below 20 mm/h and the maximum value slightly above 30 mm/h over the given period of time where the difference of rain attenuation is less than 1 dB/km. Furthermore, based on [i.104], the historic rainfall data collected for one year in Durham in UK, which is typically well known for its frequent and heavy rainfall, showed that 99,95 % of the rainfall over the year remains below 50 mm/h and the same for 99,8 % of the rainfall considering the worst month. Note that the historical data does not include cloudburst, but rather it indicates the mid-term rainfall rate.

In addition, it is important to note that [i.105] showed that the calculation of the rain attenuation based on rain rate (ITU-R) may over- or underestimate its actual impact on wave propagation, depending on the actual droplet size, shape and type of rain. Due to the fact that those behaviours of rain are not predictable and differ from in diverse ways at different times and in different locations, it may be necessary to employ individual rain attenuation models for specific categories at the regional and seasonal levels to more precisely reflect its impact on wave propagation.

5.1.3 Clouds and fogs attenuation due to droplets

For terrestrial links, the effect of clouds may be less relevant and can therefore be excluded, as the link through clouds is unlikely to occur except in alpine regions. In contrast, the influence of fog may be of interest and emphasized for the dense urban area where fog is highly expected due to its geographical and environmental reason such as San Francisco, London, and Cape Town.

Cloud and fog consist of small droplets, generally less than 0,01 cm, that induce the scattering effect in wave propagation. In Recommendation ITU-R P.840-8 [i.24], a mathematical model up to 200 GHz based on Rayleigh scattering considering a double-Debye model for the dielectric permittivity of water is provided and is given by:

$$\gamma_c = K_l \rho_l$$

where γ_c is the specific attenuation (dB/km) due to scattering from liquid contents within the cloud or fog, K_l is liquid water specific attenuation coefficient ((dB/km)/(g/m^3)) and ρ_l is liquid water density in the cloud or fog (g/m^3). Although the recommendation is valid up to 200 GHz, the same approach can be extrapolated to the THz range.

In general, the liquid water content can be estimated by post-processing the measurement data obtained with specific instruments for droplet size distribution such as cloud droplet probe or fog monitor. This approach requires extensive measurement and post-processing data, hence the increased computational effort. Instead, a look-up table for typical liquid water densities of cloud and fog types can be used to reduce the effort needed to obtain exact values for modelling their effects on channels. Table 4 includes some typical value of the liquid water density of various cloud and fog types given in [i.24] and [i.106].

Table 4: Typical liquid water density for various cloud and fog types

Cloud/fog type	Typical liquid water density in g/m^3
Medium fog (visibility of the order of 300 m) [i.24]	0,05
Stratocumulus/stratus/altostratus [i.106]	0,2
Thick fog (visibility of the order of 50 m) [i.24]	0,5

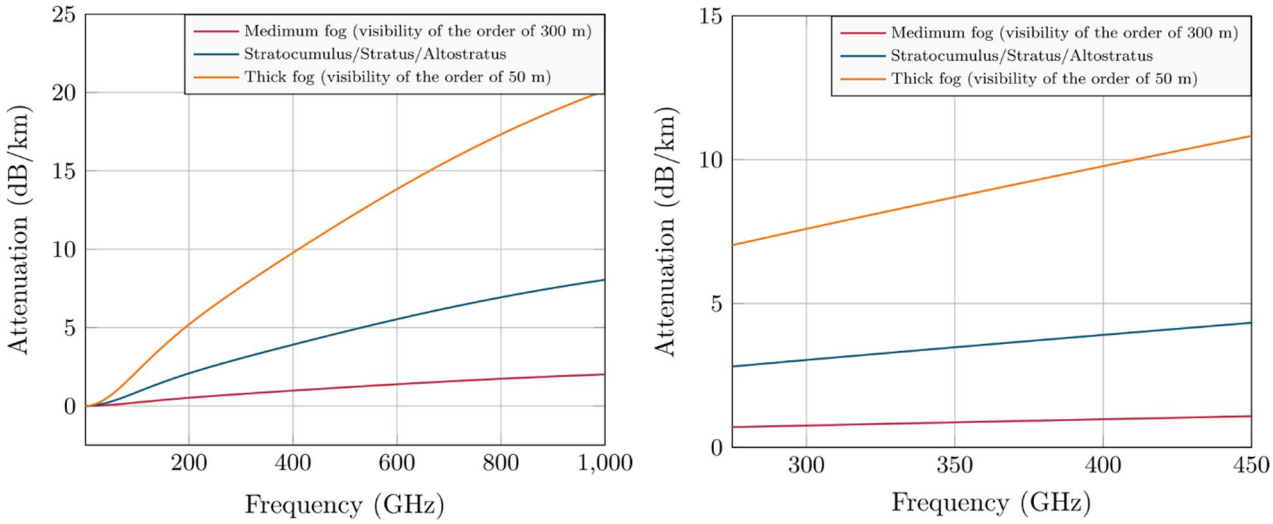

NOTE: Frequency range between 1 GHz to 1 000 GHz (left) and 275 GHz to 450 GHz identified for fixed and mobile services (right).

Figure 6: Frequency-dependent cloud and fog attenuation for straight path (same height level for both TX and RX) considering temperature of 15 °C and typical values of liquid water density given in Table 4

The frequency-dependent cloud and fog attenuation for the straight path continuously increases in value as the frequency increases. In addition, the slope of the graph and the liquid water density are positively correlated, i.e. the slope of the graph increases as the density increases.

For the short-range communication over tens of metres, the effect of the cloud and fog attenuation can be selectively negligible depending on the frequency for the given types of cloud and fog in Table 4. In particular, in the case of medium fog, fog attenuation does not hinder the long-range communication as well as it demonstrates only minor impact on wave propagation. Besides, in the case of medium fog, stratocumulus, stratus and altostratus in the frequency range between 275 and 450 GHz, the effect of cloud and fog in a broadband channel can potentially be assumed as transmission at a single centre frequency rather than considering their effect separately over the wider bandwidth. Especially, in the case of medium fog in the frequency range between 275 GHz and 450 GHz, the attenuation is less than 1,1 dB over a distance of 1 km.

5.1.4 Consideration on simulation complexity

Above mentioned atmospheric effects are frequency and distance dependent. By applying those effect to a simulator, the computational complexity can be unnecessarily increased when applying different atmospheric effect modeling coefficients to different paths, especially in the case of wide band channels in environments with numerous multi-paths with various path distances. For example, if N clusters and M rays per cluster have different delays, M × N convolution operations or frequency domain coefficient multiplications are required. When dropping multiple UEs in system-level simulation, the distance and delay are different for each UE, so complexity increases by a multiple of the number of UEs.

Instead, applying a cluster common atmospheric effect modelling as proposed in [i.1] can be a promising method to reduce the computational complexity further, whose specific loss for cluster n at centre frequency f_c is modelled as:

$$OL_n(f_c) = \frac{\alpha(f_c)}{1000} \cdot (d_{3D} + c \cdot (\tau_n + \tau_\Delta)) \text{ [dB]}$$

where $\alpha(f_c)$ is frequency dependent atmospheric effects [dB/km], c is the speed of light [m/s], d_{3D} is the distance [m], τ_n is the n-th cluster delay [s] in Step 11 in clause 7.5 in [i.1], τ_Δ is 0 in the LoS case and min(τ'_n) otherwise, where min(τ'_n) is the minimum delay. If a ray within a cluster has a different delay, a different atmospheric effect value can be applied for accurate modelling. To reduce complexity, all rays within one cluster share common atmospheric effects loss for simplicity.

In addition, considering scenarios designed for short range communication (tens of metres) and using frequency windows where atmospheric loss is small, the impact of atmospheric effect is negligible, e.g. negligible molecular absorption loss (< 0,1 dB) at around 250 GHz over 30 m. Furthermore, in the long-range scenario, the effective path delay of the beam-formed channel will also be reduced as the high path loss can be compensated by using a sharp beam in the THz band. In other words, applying different atmospheric effect coefficients for each path will have little effect on simulation performance. Thus, the small delay difference between rays in a cluster can be ignored and applied the cluster-level path delay to atmospheric effects modeling. Although this approach may result in inaccuracy of prediction of some multi paths, it can generate a frequency-selective coefficient set and apply a single time-domain convolution or a single frequency-domain multiplication. In this respect, the atmospheric effects can be considered separately according to the application scenarios and appropriate model can be applied correspondingly for the sake of balance simplicity and accuracy.

5.2 Effect of micro-mobility

5.2.1 Causes of micro-mobility

5.2.1.1 Wind turbulence

The impact of wind on antenna mast movement was investigated in [i.183], which concluded that when antennas and their supporting structures are exposed to strong winds, the mechanical stress can induce vibrations and mechanical distortions, sometimes leading to temporary deviations of the main beams from their intended directions. In [i.184], a long-term measurement campaign was conducted, revealing a correlation between mechanical vibration and received radio power, with wind-induced losses potentially reaching up to 4,4 dB at millimetre-wave frequencies. In [i.185], a model is presented for estimating the effective gain of antennas under windy conditions for THz fixed wireless systems. This model considers input parameters such as the inner and outer diameter of the antenna pole, the length of the pole, the antenna diameter etc., with the results showing that, under extreme 43,5 m/s windy conditions, the maximum antenna gain designed without consideration of the wind effects being 48,18 dBi reduces to an effective gain of 43,84 dBi when wind effects are taken into account.

5.2.1.2 Mechanical vibrations

When an antenna vibrates, it generates phase noise in the signals it transmits and receives. This source of noise is particularly critical for microwave and millimetre-wave systems operating in high-vibration environments, and even more so for THz systems, where low phase noise at small frequency offsets is essential. In [i.186], an analytical framework describing how antenna vibrations induce phase noise is provided. In [i.187], horizontally induced vibrations on an antenna in a laboratory environment at a frequency of 25 GHz are emulated using a vibration rig. This research demonstrates that vibrations cause the antenna misalignment and perturbation of the composite amplitude and phase of the radiation pattern. The phase changes are significant, as they add modulation at the receiver's side, which degrades the quality of the link. Further practical insights are shown in [i.188], where mechanical vibrations of an intra-vehicular 60 GHz communication system mounted in a passenger vehicle were caused by driving on uneven pavement and by running the internal combustion engine. In this case, the vibrations manifested as an increased level of phase noise. In [i.189], a wagon-to-wagon 60 GHz wireless system is operated, and vibrations are measured. The authors point out that the Doppler spread and coherence time of the channel are affected by the vibrations of the train. As for THz bands, a rigorous analysis of phase noise and antenna misalignment effects on the outage probability of wireless systems is carried out in [i.190].

5.2.1.3 Physical movement

In this context, physical movement refers to the deliberate movement of the user holding a user equipment, or a movement in the surrounding vicinity of the THz channel.

Self-user shadowing effects on millimetre-wave mobile phone antennas at 28 and 60 GHz are researched in [i.191]. The results of the shadowing simulations are significant: it was found that, in a one-hand grip, the human body shadows the radiation by up to 22 dB for a 60° sector behind the user at 28 GHz, while at 60 GHz, the maximum shadowing increases to 30 dB. When a two-hand browsing grip was considered, the shadowed sector increased to 77° behind the user. In the THz band, a multihop-assisted backhaul communication mixed with an access link under shadowed fading with antenna misalignment errors is considered in [i.192]. Besides other theoretical derivations, asymptotic expressions for the outage probability in the high SNR region are provided.

Another possible source of additional loss caused by physical movement is foliage shadowing. In a high wind situation, a wireless link that is otherwise obstruction-free might be interrupted by the movement of branches or trees. In this case, for the frequency of 140 GHz, the additional loss is measured in [i.193], ranging from 3 dB/m to 10 dB/m, depending on the specific tree.

In a data centre environment, it was shown in [i.43] that airflow caused by the cooling fans vibrated the cabling system in the data centre. Such vibrations have impacted the THz channel, where the authors have quantified this phenomenon by deriving a Doppler power spectrum.

5.2.1.4 Solar radiations

Antennas may be deployed on monopoles that have wide surface areas with poor heat dissipation capabilities. When exposed to the sun, the temperature difference between the exposed and unexposed areas to sun radiation causes a tilt to the pole that may result in a link performance degradation for highly directional antennas [i.183], [i.194]. For instance, in [i.183], it was shown that the performance of the communication link degraded due to solar radiation. A similar observation is reported in [i.194], where a quasi-periodic behaviour of received signal fades due to solar radiation is depicted.

5.2.1.5 Building sways

Building sways due to wind, weak earthquakes and thermal expansions of structures were considered as causes of performance degradation in the context of free-space optical communications [i.195].

5.2.2 Effects of micro-mobility

5.2.2.1 Micro-Doppler

The concept of Micro-Doppler phenomena in the existing literature is somewhat vague, with two scenarios that can be more specifically identified: (1) the motion of human limbs during specific activities [i.196], and (2) distinct Doppler signatures associated with Unmanned Aerial Vehicles (UAVs) generated by their propellers [i.197]. Both scenarios typically assume that a general (or macro-) Doppler effect arises from the movement of the entire human body or the UAV. However, with increasing centre frequencies and signal bandwidths, it has become feasible to detect not just a single reflection from the target object but rather to discern multiple frequency shifts within the received signal. The (macro-) Doppler shifts are predominantly determined by the velocity and motion vector of the target object, whereas the frequency shifts representing the Micro-Doppler effects are attributed to reflections from specific parts of the target object that move relative to its main body (such as limbs or propellers).

Micro-Doppler signatures are produced by the kinematic properties of the subject's motion and can be used to extract salient features of the subject's behaviour [i.198]. For example, in [i.196], the movement of limbs causes specific signatures that indicate human activity. In [i.197], the Micro-Doppler signature can reveal the specific type of UAV. As indicated in the previous clause 5.2.1, such micro-mobility effects can cause vibrations, leading to increased phase noise, shadowing, Doppler spread, reduced coherence times or even antenna misalignment. The severity of these phenomena ranges from a few dB in the case of wind effects on an antenna on a mast to tens of dB in the case of shadowing.

5.2.2.2 Boresight antenna gain variation

Adopting higher frequencies comes with the price of an increased propagation loss. To compensate for such losses, higher antenna gains are deployed to focus energy from the transmitter to the receiver. Antennas with higher gains, however, have narrow beam-widths, thus having an increased directional sensitivity, and rendering the communication link more sensitive to slight misalignments and susceptible to outages. Therefore, micro-mobility could pose a challenge concerning the reliability of such links. In [i.199], an analysis of the performance of THz communication links affected by dynamic and random misalignment was carried out, where the performance degradation was quantified. In [i.183], it was shown with measurements that the received signal level drops in association with higher wind speeds and pole tilt due to solar radiations. The same report has shown that the severity of the angular misalignment is dependent on the type and height of the pole that holds the antenna. Therefore, micro-mobility has a negative impact on the directivity of links with very narrow beam-widths, and may require more sophisticated antenna apparatus to combat the misalignment.

5.3 Specific considerations for scattering, reflections, and diffractions

5.3.1 Modeling surface roughness

5.3.1.0 Introduction

As the frequency moves to the THz band, the wavelength in the sub-millimetre range approaches the size of the surface microstructures of some common objects [i.136] (e.g. Wallpaper [i.143], [i.137] Brick [i.138], Wood [i.139], etc.). The surfaces that are considered smooth at lower frequency bands can become incredibly rough for THz waves [i.140]. Therefore, scattering will play a significant role in the propagation at THz bands [i.141] reliable scattering models on rough surfaces are essential for accurate THz channel modeling. Modeling of rough surface scattering at THz frequencies in specular and non-specular directions has been addressed e.g. in [i.136], [i.167]. An extensive measurement campaign of a representative collection of 50 building materials typically used for construction of buildings has been performed in [i.94]. The measured characteristics - including the scattering - have been made publicly available at https://doi.org/10.6084/m9.figshare.21539109.

To measure the roughness of the surface on an object, the common equipment including optical profilers, etc., are able to portray and model the surface microstructure accurately. Generally, the height fluctuations of these random rough surfaces are widely considered to obey certain statistical distributions, such as Gaussian [i.142], exponential or other non-Gaussian distributions [i.143]. Gaussian rough surface, as a typical rough surface, can be modelled using the Monte Carlo method [i.144], and its two important distribution parameters include Root Mean Square (RMS) height and correlation length. The RMS height is used to describe the RMS value of the height fluctuation on the rough surface, while the correlation length characterizes the correlation between two points on the rough surface [i.142]. Figure 7 illustrates the appearance of the Gaussian rough surface with different roughness.

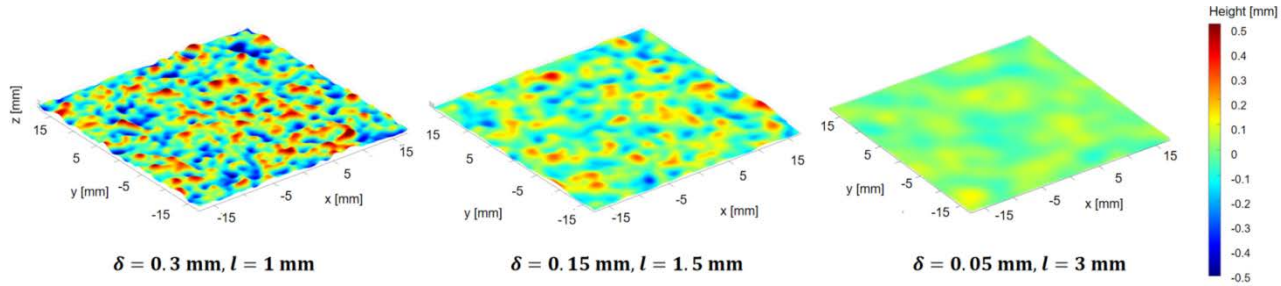

Figure 7: Surfaces with different roughness generated using Monte Carlo method

The modeling methods for rough surface scattering are classified into four categories in the present document, including numerical method, approximate computational method, theoretical modeling method, and Deep Learning (DL)-based modeling method.

5.3.1.1 Numerical method

Benefiting from the development of computer technology in the last century, accurate numerical calculation methods have been widely used in the calculation of electromagnetic scattering from rough surfaces [i.145]. Due to the direct numerical solution of Maxwell's equations, it has the advantages of wide range of applicability and high computational accuracy, but with the drawbacks of large memory occupation and time-consuming.

The numerical methods can be classified into four types according to the form of the equations, which are frequency-domain integration (e.g. method of moments [i.146], Fast Multipole Method [i.147], Multi Level Fast Multipol Method [i.148]), frequency-domain differentiation (e.g. Finite Element Method [i.149]), time-domain integration (e.g. Finite Difference Time Domain [i.150]), and time-domain differentiation.

However, due to the short wavelength of THz waves, rough surfaces often behave as electrically large dimensions, so the use of parallel computing [i.151] or GPU acceleration [i.152] is necessary to improve the efficiency of solving electromagnetic scattering problems. Besides, the combination of numerical computation and high-frequency approximate methods is also an important research direction to enhance the solution efficiency, such as MOM-PO [i.153].

5.3.1.2 Approximate computational method

When the size of the rough surface satisfies certain conditions, some parameters of the electromagnetic scattering calculation can be reasonably approximated [i.154].

Commonly used methods such as Kirchhoff's approximation [i.155], small-perturbation method [i.156], small slope approximate method [i.157], two-scale method [i.158], etc. are respectively applicable to rough surfaces under different conditions. The Kirchhoff method requires that the mean radius of curvature on rough surfaces should be larger than one wavelength [i.159]. The small perturbation method requires the value of the average slope of the surface to be at the same order of magnitude as the product of wave number and root mean square deviation, with the root mean square deviation being less than 5 % of the wavelength [i.160]. The two-scale method is a combination of the former two methods for solving the scattering problem for rough surfaces containing both large and small roughness structures. Compared with the numerical methods, the approximate method is simpler and more efficient, but the computational accuracy is reduced and has a certain range of applicability.

5.3.1.3 Theoretical modeling method

For some common scattering scenarios in wireless communication environments, especially when the scattering comes from flat rough surfaces such as floors, ceilings, walls, tiles, etc., theoretical modeling methods enable faster computation of scattering, which is crucial for improving the overall efficiency of ray tracing-based channel modeling [i.161].

Theoretical models are based on some assumption or theory that can mathematically formulate the laws of scattering. Typical theoretical modeling methods include the Directive Scattering (DS) model [i.162] and the Lambertian scattering model. Instead of modeling the specific structure of the rough surface, they only need to reconstruct the scattering lobe by one or two parameters, which demonstrates the theoretical distribution characteristics of the scattering field. For example, the DS model describes the width of the lobe by the equivalent roughness and the scattering strength by the scattering coefficient. In addition, the study [i.163] proposes a method based on the DS model, which is capable of better describing the stochastic characteristics of rough surface scattering in the THz band.

5.3.1.4 Deep Learning (DL)-based modeling method

The DL model has a strong adaptive learning ability to find implicit mapping relationships between input and output data. The fully trained neural network has excellent generalization ability, good computational accuracy, and efficiency.

In recent years, with the development of DL technology, researchers have begun to explore the application of neural network models in electromagnetic scattering calculations [i.164]. In [i.165], a DL-based current generation method for rough surfaces is proposed and the THz scattered electric fields is reconstructed using the Dyadic Green's function [i.166]. Compared with approximate and theoretical modeling methods, DL-based methods have superior computational accuracy and efficiency, but lack interpretability and require a large amount of simulation or measurement data as a database to train a reliable DL model.

5.4 Considerations for large arrays and near-field propagation effects

5.4.1 Spherical wave modelling

5.4.1.0 Introduction

Geometry-based MIMO channel models, such as ETSI TR 138 901 [i.1], assume operations in the far-field region, where propagation can be modelled using the plane wave theory. However, this assumption may not be accurate for the modelling of THz channels. Given the short wavelength relative to the effective antenna aperture, part of the coverage area can fall into the near-field region. To address this issue, two extensions of ETSI TR 138 901 [i.1] to support spherical wavefront modelling are proposed, and potential issues related to the increased computational complexity are discussed.

5.4.1.1 Stochastic-based approach

In the near-field region, the plane wave approximation is no longer valid and a spherical wavefront model should be used instead. As a consequence, the phase variation over the TX/RX arrays depends not only on the incident angle but also on the position of the element with respect to the centre of the spherical wavefront.

In the following, it is discussed how the 3GPP spatial channel model can be extended to support the modelling of spherical wavefronts. Only the effects of wave's curvature on the phase are considered, while any amplitude variation is neglected. This is reasonable when operating in the radiating near-field region [i.177]. A geometric representation of the proposed extension is depicted in Figure 8.

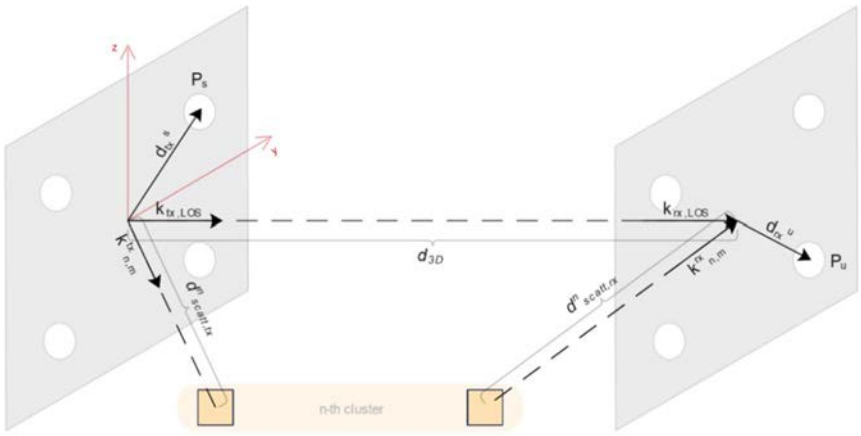

Figure 8: Representation of the proposed extension to support spherical wave propagation

LoS component

The channel impulse response of the LoS path between *s*-th transmit and the *u*-th receive elements is expressed as:

$$\begin{aligned} h_{u,s}^{LOS}(t,\tau) &= e^{-\frac{j2\pi}{\lambda}d_{3D}} e^{\frac{j2\pi}{\lambda}\Delta\Phi_{LOS}^{s,u}} \delta(\tau-\tau_{LOS}) \\ &= e^{-\frac{j2\pi}{\lambda}d_{3D}} e^{\frac{j2\pi}{\lambda}\Delta\Phi_{tx,LOS}^{s}} e^{\frac{j2\pi}{\lambda}\Delta\Phi_{rx,LOS}^{u}} \delta(\tau-\tau_{LOS}), \end{aligned}$$

where d_{3D} corresponds to the distance between the centre of the transmit and receive arrays, λ is the wavelength, τ_{LOS} is the delay of the LoS path, and $\Delta\Phi_{LOS}^{s,u} = \Delta\Phi_{tx,LOS}^{s} + \Delta\Phi_{rx,LOS}^{u}$ represents the phase variation due to the array geometries.

When adopting a spherical wavefront model, the phase variation $\Delta\Phi_{LOS}^{s,u}$ is equivalent to the distance between the s-th transmit and u-th receive antenna elements. By setting the origin of the coordinate system at the centre of the transmit array, the position of the s-th transmit element is $P_s = \vec{d}_{tx}^{s}$, while the position of the u-th receive element is $P_u = d_{3D} \cdot \vec{k}_{tx,LOS} + \vec{d}_{rx}^{u}$, where $\vec{k}_{tx,LOS}$ is the spherical unit vector of the LoS ray. Then, the phase excitation can be computed as:

$$\begin{aligned} \Delta\Phi_{LOS}^{s,u} &= d_{3D} - ||P_s - P_u|| \\ &= d_{3D} - ||\vec{d}_{tx}^{s} - d_{3D} \cdot \vec{k}_{tx,LOS} - \vec{d}_{rx}^{u}||, \end{aligned} \quad (1)$$

where a normalization with respect to d_{3D} is needed to avoid a double contribution of the phase shift due to the propagation distance.

NLoS components

The channel impulse response for the NLoS components between the s-th transmit and u-th receive antenna elements can be expressed as:

$$h_{u,s}^{NLOS}(t,\tau) = \sum_{n=1}^{N} \sum_{m=1}^{M} \sqrt{\frac{P_n}{M}} e^{\frac{j2\pi}{\lambda}\Delta\Phi_{tx,n,m}^{s}} e^{\frac{j2\pi}{\lambda}\Delta\Phi_{rx,n,m}^{u}} \delta(\tau - \tau_n),$$

where *N* is the number of clusters, *M* is the number of rays, P_n is the cluster power, τ_n is the cluster delay, and the terms $\Delta\Phi_{tx,n,m}^{s}$ and $\Delta\Phi_{rx,n,m}^{u}$ represents the phase excitation of path *m* in cluster *n* due to the transmit and receive array geometries.

For the NLoS components, the centre of the spherical wavefront corresponds to the position of the first (in case of departing wave) or last (in case of arriving wave) scatterer, as represented in Figure 8. Therefore, the phase excitation can be expressed as:

$$\Delta\Phi_{tx,n,m}^{s} = d_{scatt,tx}^{n} - d_{scatt,tx}^{n,s} \quad (2)$$

$$\Delta\Phi_{rx,n,m}^{u} = d_{scatt,rx}^{n} - d_{scatt,rx}^{n,u} \quad (3)$$

where $d_{scatt,tx}^{n,s}$ is the distance between the *s*-th antenna element at the transmitter and the first scatterer hit by cluster *n*, $d_{scatt,tx}^{n}$ is the distance between the centre of the transmit array and the first scatterer hit by cluster *n*, $d_{scatt,rx}^{n,u}$ is the distance between the *u*-th antenna element at the receiver and the last scatterer hit by cluster *n*, and $d_{scatt,rx}^{n}$ is the distance between the centre of the receive array and the last scatterer hit by cluster *n*. Equations 2 and 3 can be written as:

$$\Delta\Phi_{tx,n,m}^{s} = d_{scatt,tx}^{n} - ||d_{scatt,tx}^{n} \cdot \vec{k}_{tx,n,m} - \vec{d}_{tx,s}|| \quad (4)$$

$$\Delta\Phi_{rx,n,m}^{u} = d_{scatt,rx}^{n} - ||d_{scatt,rx}^{n} \cdot \vec{k}_{rx,n,m} - \vec{d}_{rx,u}|| \quad (5)$$

where $\vec{k}_{tx,n,m}$ and $\vec{k}_{rx,n,m}$ are the spherical unit vector of the m-th ray belonging to the n-th cluster, for the transmitter and receiver. Here implicit assumption is made that all rays belonging to the same cluster interact with the same scattering objects. This is reasonable since all rays in a cluster experience the same propagation delay. Furthermore, ETSI TR 138 901 [i.1] subdivides the three strongest NLOS clusters into sub-clusters with different propagation delays. In this case, the same formulation applies at a sub-cluster level.

To apply equations 4 and 5, the distances $d_{scatt,tx}^{n}$ and $d_{scatt,rx}^{n}$ between the centre of the transmit (receive) array and the first (last) scattering objects need to be determined. The 3GPP framework does not provide any explicit modelling of the scattering object, therefore $d_{scatt,tx}^{n}$ and $d_{scatt,rx}^{n}$ cannot be determined directly. A possible approach to determine $d_{scatt,tx}^{n}$ and $d_{scatt,rx}^{n}$ is the one proposed in [i.178], which involves the solution of an optimization problem for determining $d_{scatt,tx}^{n}$ and $d_{scatt,rx}^{n}$ such that the distance between the first bounce and last bounce scatterer is minimized. Another approach is to regard $d_{scatt,tx}^{n}$ and $d_{scatt,rx}^{n}$as random variables whose distribution is derived from simple geometrical considerations. From the propagation delay, the propagation distance of the *n*-th cluster as $d_n = \tau_n \cdot c + d_{3D}$ can be computed, where *c* is the speed of light and d_{3D} is the 3D distance between the transmit and receive arrays. The delays are normalized with respect to the first component, i.e. the first component has delay 0. d_n represents an upper bound for determining $d_{scatt,tx}^{n}$ and $d_{scatt,rx}^{n}$, because the overall propagation distance is greater or equal to the sum of lengths of the first and last segments:

$$d_{scatt,tx}^{n} + d_{scatt,rx}^{n} <= d_n.$$

The equality is reached when cluster *n* interacts with a single scatterer before reaching the receiver. Based on these considerations, $d^n_{scatt,tx}$ and $d^n_{scatt,rx}$ can be determined with the following procedure:

1) compute the overall propagation distance as $d_n = \tau_n \cdot c + d_{3D}$;

2) draw $d^n_{scatt,tx} \sim U[D^{min}_{scatt}, d_n - D^{min}_{scatt}]$;

3) draw $d^n_{scatt,rx} \sim U[D^{min}_{scatt}, d_n - d^n_{scatt,tx}]$,

where D^{min}_{scatt} corresponds to the minimum distance between the centre of the Tx/Rx array and the first/last bounce scatterer. D^{min}_{scatt} should be set according to the scenario (e.g. 0,1 m for indoor propagation and 1 m for outdoor propagation is indicated in [i.178]).

To include the modelling of spherical wavefronts, the procedure should be extended as shown in Figure 9. In particular, an additional step after step 5 is needed for computing the terms $d^n_{scatt,tx}$ and $d^n_{scatt,rx}$ as described above. Moreover, step 11 has to be modified for computing the phase components $\Delta\Phi^{s,u}_{LOS}$, $\Delta\Phi^{s}_{tx,n,m}$, and $\Delta\Phi^{u}_{rx,n,m}$ using equations 1, 4 and 5.

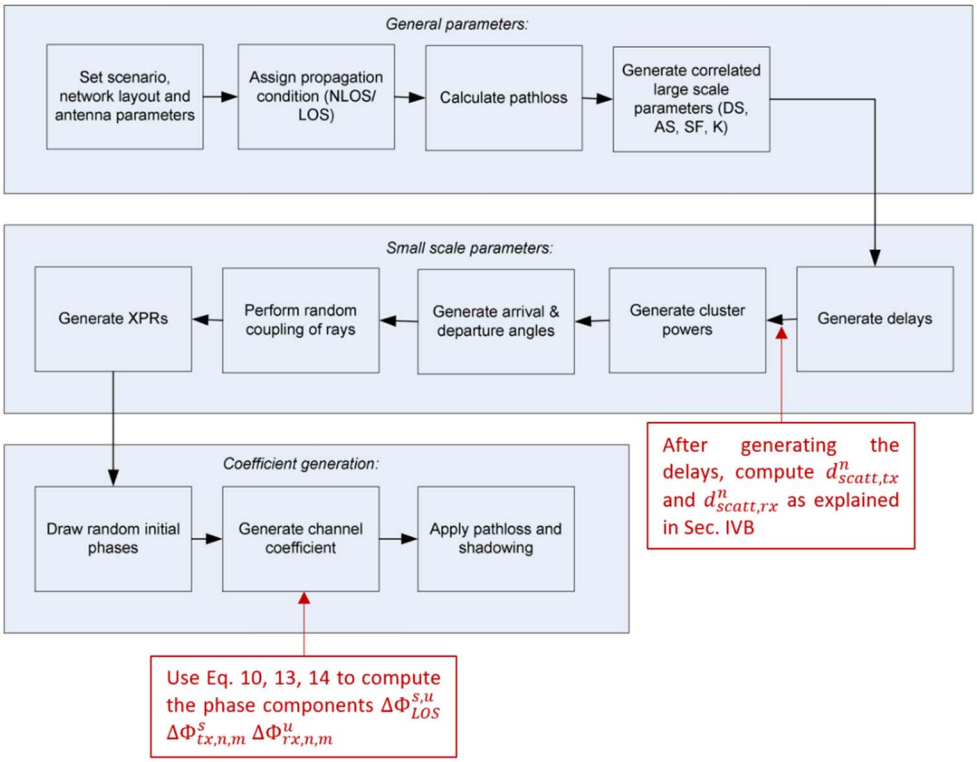

Figure 9: Modified channel coefficient generation procedure from 3GPP TR 138 901 [i.1] to support spherical wave modeling

5.4.1.2 Virtual Tx-based approach

5.4.1.2.0 Introduction

The idea of the proposed solution is to provide simple means to determine propagation distance between each Tx and Rx antenna element and to use them for: 1) spherical wave modelling, 2) frequency dependent array responses, and 3) frequency dependent Doppler shifts. In mobile channels the time variant propagation delays are determined. These per antenna propagation delays can be used to substitute the departure/arrival related phase terms of antenna arrays and the phase terms related to Doppler, as they are used in legacy models such as ETSI TR 138 901 [i.1]. For the LoS path it is straightforward to calculate distances between Tx and Rx arrays since array locations and element locations within arrays are known. In the case of NLoS paths this is not trivial, since the model provides only angles and delay, but not locations or types of interacting objects. If the location and orientation of, e.g. a reflecting surface or a diffracting edge were known, one could determine per antenna path lengths, but the model does not provide this information.

To overcome this problem, the following operation of finding virtual array positions for each propagation path can be used. It is essentially done by rotating the Tx antenna array in the global cartesian coordinate system such, that the arrival and departure angles are pointing towards each other's and the distance between array centres corresponds to the original path length in metres. Based on the original Rx antenna coordinates and the new virtual Tx antenna coordinates the per antenna distances can be calculated similarly as in the LoS path case. This operation is performed separately for each path (ray). The underlying assumption is that the interaction is reflection, which is the most significant interaction type at sub-THz frequencies. In the absence of interaction type information of NLoS paths they can be assumed specularly reflected.

5.4.1.2.1 Description

Assume the interactions in propagation environment are not frequency dependent within the frequency band of interest and the polarimetric propagation channel matrix of the lth path between Tx location and Rx location is $\mathbf{h}_l \in \mathbb{C}^{2\times 2}$. In addition to the complex 2×2 coefficient matrix, the path l is characterized by departure angle Ω_l^{tx}, arrival angle Ω_l^{rx}, and propagation delay (=path length) τ_l. The propagation channel can be represented as a sum of L discrete impulse like propagation paths as:

$$\mathbf{h}(\Omega^{\mathrm{rx}}, \Omega^{\mathrm{tx}}, \tau) = \sum_{l=1}^{L} \mathbf{h}_l \delta(\Omega^{\mathrm{rx}} - \Omega_l^{\mathrm{rx}})\delta(\Omega^{\mathrm{tx}} - \Omega_l^{\mathrm{tx}})\delta(\tau - \tau_l). \tag{6}$$

Tx and Rx antenna arrays have N and M elements, respectively. Position of each Rx antenna $m = 1, \dots, M$ is defined by vector $\vec{d}_m^{\mathrm{rx}}$ in the global geometry. Polarimetric antenna pattern matrices of the Rx and the Tx array are $\mathbf{G}_{\mathrm{rx}}(\Omega^{\mathrm{rx}}) \in \mathbb{C}^{M\times 2}$ and $\mathbf{G}_{\mathrm{tx}}(\Omega^{\mathrm{tx}}) \in \mathbb{C}^{N\times 2}$, respectively. Rows of $\mathbf{G}_{\mathrm{rx}}(\Omega^{\mathrm{rx}})$ contain complex antenna gains for orthogonal polarizations from arrival direction Ω^{rx}. Note that each antenna element pattern is defined with respect to its individual radiation phase centre, i.e. the array geometry does not affect the entries of $\mathbf{G}_{\mathrm{rx}}(\Omega^{\mathrm{rx}})$ or $\mathbf{G}_{\mathrm{tx}}(\Omega^{\mathrm{tx}})$. Tx pattern $\mathbf{G}_{\mathrm{tx}} \in \mathbb{C}^{N\times 2}$ and position vectors $\vec{d}_n^{\mathrm{tx}}$ are defined analogously. As auxiliary parameters position vectors to array centres are defined as:

$$\begin{cases} \vec{d}^{\mathrm{rx}} = \sum_m \vec{d}_m^{\mathrm{rx}}/M \\ \vec{d}^{\mathrm{tx}} = \sum_n \vec{d}_n^{\mathrm{tx}}/N \end{cases}. \tag{7}$$

Distance from mth Rx element to nth Tx element in the LoS path case is calculated as:

$$d_{mn} = \left\| \vec{d}_n^{tx} - \vec{d}_m^{\mathrm{rx}} \right\|, \tag{8}$$

where $\|\ \ \|$ is the norm (=length) of a vector. Distances for an NLoS path l is determined as follows.

First define a rotation matrix $\mathbf{R}_l \in \mathbb{R}^{3\times 3}$ for each path l based on the arrival unit vector $\vec{r}_l^{\mathrm{rx}}$ from angle $\Omega_l^{\mathrm{rx}}$and departure unit vector $\vec{r}_l^{\mathrm{tx}}$ to angle Ω_l^{tx} as:

$$\mathbf{R}_l = \mathbf{I} + 2\mathbf{K}^2 = \begin{bmatrix} 1 & 0 & 0 \\ 0 & 1 & 0 \\ 0 & 0 & 1 \end{bmatrix} + 2\begin{bmatrix} 0 & -a_z & a_y \\ a_z & 0 & -a_x \\ -a_y & a_x & 0 \end{bmatrix}^2 \tag{9}$$

where $\mathbf{I}$ is the 3×3 identity matrix and the unit vector pointing between vectors $-\vec{r}^{\mathrm{rx}}$ and $\vec{r}^{\mathrm{tx}}$ in the plane set by them is:

$$\vec{a} = [a_x \quad a_y \quad a_z]^T = \frac{-\vec{r}_l^{\mathrm{rx}} + \vec{r}_l^{\mathrm{tx}}}{\left\| -\vec{r}_l^{\mathrm{rx}} + \vec{r}_l^{\mathrm{tx}} \right\|}. \tag{10}$$

Now for the lth NLoS path the Tx antenna elements are rotated using $\mathbf{R}_l$ such that the new virtual positions and orientations of antenna elements correspond to the condition where the propagation distance between array centres is $\tau_l c_0$, and arrival and departure vectors point towards each other's as illustrated in the example in Figure 10. The position vector for the nth virtual Tx element is:

$$\vec{d}_{nl}^{\,vtx} = \mathbf{R}_l\left(\vec{d}_n^{\,tx} - \vec{d}^{\,\mathrm{tx}}\right) + \vec{d}^{\,\mathrm{rx}} + \vec{r}_l^{\,\mathrm{rx}}\tau_l c_0, \tag{11}$$

where c_0 is the speed of light in vacuum. In equation 11 the nth element is first translated close to origin such that the array centre would be exactly in the origin, then it is rotated by $\mathbf{R}_l$, then translated to the location indicated by the Rx centre, and finally translated to the direction of the arrival unit vector to the distance specified by τ_l.

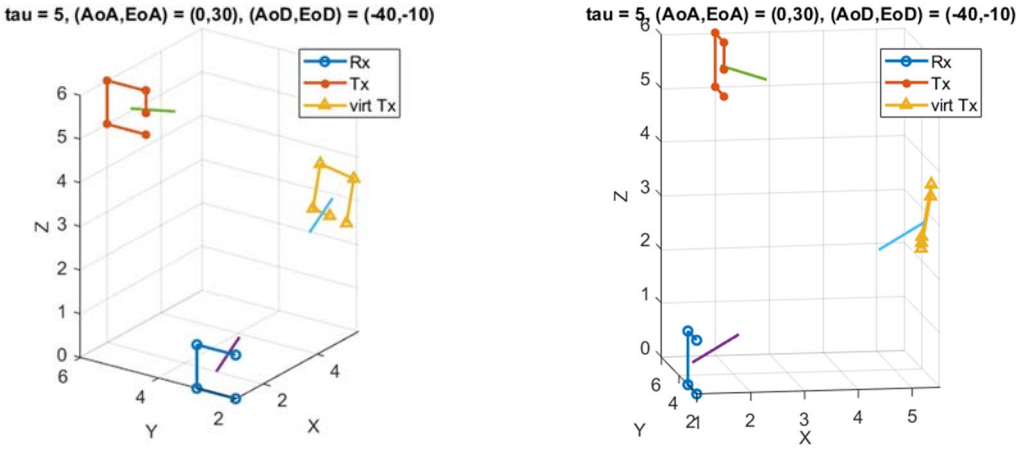

NOTE: Both figures illustrate the same configuration from different perspectives.

Figure 10: An example of Tx, Rx, and rotated virtual Tx arrays and unit vectors indicating arrival/departure angles

Now each Tx/Rx antenna pair has a unique propagation delay for each path, determined simply as:

$$\tau_{lmn} = \frac{\left\|\vec{d}_m^{\,\mathrm{rx}} - \vec{d}_{nl}^{\,vtx}\right\|}{c_0}. \tag{12}$$

Propagation delays of path l can be collected in a matrix:

$$\mathbf{T}_l = \begin{bmatrix} \tau_{l11} & \cdots & \tau_{l1N} \\ \vdots & \ddots & \vdots \\ \tau_{lM1} & \cdots & \tau_{lMN} \end{bmatrix} \in \mathbb{R}_+^{M\times N}. \tag{13}$$

Finally, by including Tx and Rx antenna arrays of N and M elements, respectively, the MIMO radio channel in frequency domain can be defined as:

$$\mathbf{H}(f) = \sum_{l=1}^{L} \left(\mathbf{G}_{\mathrm{rx}}(\Omega_l^{\mathrm{rx}})\,\mathbf{h}_l\,\mathbf{G}_{\mathrm{tx}}(\Omega_l^{\mathrm{tx}})^T\right) \odot \exp(-j2\pi f \mathbf{T}_l) \in \mathbb{C}^{M\times N}, \tag{14}$$

where f is the radio frequency and $\odot$ is the Hadamard product (element-wise matrix product) operator. If keeping the delay domain representation, the channel coefficient from nth Tx antenna to mth Rx antenna for path l can be written as:

$$H_{m,n,l}(\tau) = \mathbf{g}_{\mathrm{rx},m}(\Omega_l^{\mathrm{rx}})\,\mathbf{h}_l\,\mathbf{g}_{\mathrm{tx},n}(\Omega_l^{\mathrm{tx}})^T \delta(\tau - \tau_{lmn}) \in \mathbb{C}, \tag{15}$$

where $\mathbf{g}_{\mathrm{rx},m}$ and $\mathbf{g}_{\mathrm{tx},n}$ are the mth row of Rx and the nth row of Tx antenna patter matrix, respectively.

5.4.1.2.2 Doppler and time variance due to virtual motion

Assume Rx is moving with a speed and towards a direction specified by a velocity vector $\vec{\mathrm{v}}$. The unit vector from the mth Rx antenna element to the nth virtual Tx element for the lth path is defined as:

$$\vec{\mathrm{r}}_{lmn} = \frac{\vec{d}_{nl}^{\,vtx} - \vec{r}_m^{\,\mathrm{rx}}}{\left\|\vec{d}_{nl}^{\,vtx} - \vec{r}_m^{\,\mathrm{rx}}\right\|}. \tag{16}$$

The distance increment per time unit (relative speed) between the mth Rx antenna element and the nth virtual Tx element for the lth path is:

$$v_{lmn} = \vec{\mathrm{v}} \cdot \vec{\mathrm{r}}_{lmn} \in \mathbb{R}, \tag{17}$$

where $\cdot$ is the vector dot product operator. Now the time dependency and Doppler can be introduced by specifying time variant path lengths as follows. Assume $\mathbf{T}_l$ defined in equation 13 are propagation delays at the time instant $t = 0$. At any time instant t within a small scale motion they are:

$$\mathbf{T}_l(t) = \begin{bmatrix} \tau_{l11} & \cdots & \tau_{l1N} \\ \vdots & \ddots & \vdots \\ \tau_{lM1} & \cdots & \tau_{lMN} \end{bmatrix} - \begin{bmatrix} v_{l11} & \cdots & v_{l1N} \\ \vdots & \ddots & \vdots \\ v_{lM1} & \cdots & v_{lMN} \end{bmatrix} \frac{t}{c_0} \in \mathbb{R}_+^{M \times N}. \tag{18}$$

Note that with positive relative speed, the distance between antennas and a scatterer decreases over time, i.e. propagation delays become shorter. In most practical cases, v_{lmn} are almost identical for all m and n, hence the second term in the right hand side of equation 18 could be substituted by a scalar $v_l t/c_0$, where $v_l = \vec{v} \cdot \langle \vec{\mathrm{r}}_{lmn} \rangle$, and $\langle \vec{\mathrm{r}}_{lmn} \rangle$ denotes the average unit vector over all m and n.

The motion of Tx and scatterers can be included in $\mathbf{T}_l(t)$ analogously. Here it was assumed that the overall time span is such short that the displacement remains small enough such that angles Ω do not change significantly. Notice that position vectors $\vec{r}$ are not updated, hence the name "virtual motion".

Finally, the time variant MIMO channel matrix with virtual motion is defined by updating equation 14 with time variant delays as:

$$\mathbf{H}(t, f) = \sum_{l=1}^{L} \left(\mathbf{G}_{\mathrm{rx}}(\Omega_l^{\mathrm{rx}})\, \mathbf{h}_l\, \mathbf{G}_{\mathrm{tx}}(\Omega_l^{\mathrm{tx}})^T\right) \odot \exp\left(-j2\pi f \mathbf{T}_l(t)\right) \in \mathbb{C}^{M \times N}. \tag{19}$$

Correspondingly, the delay domain representation of equation 15 can be extended to time/delay domain as:

$$H_{m,n,l}(t, \tau) = \mathbf{g}_{\mathrm{rx},m}(\Omega_l^{\mathrm{rx}})\, \mathbf{h}_l\, \mathbf{g}_{\mathrm{tx},n}(\Omega_l^{\mathrm{tx}})^T \delta\left(\tau - \tau_{lmn}(t)\right) \in \mathbb{C}. \tag{20}$$

5.4.1.3 Physical consistency considerations

In the ETSI TR 138 901 [i.1] model, it is assumed that for a given ray all antenna elements experience the same delay regardless of the size of antenna array, but when the size of antenna array becomes very large (e.g. RIS or extreme massive MIMO at BS), elements may experience different delays. In addition, $d_{scatt,tx}^n$ and $d_{scatt,rx}^n$ were generated based on uniform distributions; this method needs to be verified through channel sounding or ray tracing in realistic environments. Moreover, the proposed approach assumes that the first and last scatterers act as virtual point sources which originate a new spherical wave; whether this assumption is correct depends on the reflecting object dimensions and characteristics.

In the ETSI TR 138 901 [i.1] model, the NLoS path does not distinguish between single bounce and multi bounce and generates AoA/AoD/delay of the NLoS path stochastically. What was proposed in clause 5.4.1.2 applies determining virtual antenna positions in NLoS path with assuming one or multiple specular reflections. To what extend true THz propagation channel supports this assumption needs to be further investigated with actual channel measurements. Another issue is that when the antenna array size becomes very large, computational complexity may increase considerably when modelling virtual antenna elements of all NLoS paths. However, because the amplitude of the NLoS path is significantly smaller than that of the direct path, the performance difference may be negligible compared to the increase in complexity.

5.4.1.4 Considerations on computational complexity

In the spherical wave model, each distance between each Tx-Rx antenna pair contributes to the phase and the delay of each channel coefficient. The far-field assumptions may not be applicable in THz bands and distance calculations between individual antenna pairs may be required. This would increase computational complexity.

To address the computational complexity issue, a subarray-based wave model is introduced. For example, a subarray comprises a group of nearby antenna elements. Inside the subarray, the Planar Wave Model (PWM) can be applied since the distance between antennas can be small inside the subarray, but between subarrays, the Spherical Wave Model (SWM) may be used for channel modelling since the distance between subarrays is large. The choice of wave model is related to the communication distance, the distance between antenna elements/subarrays, and the carrier frequency.

Three wave models are considered:

- Option 1: PWM+PWM a planar wave model within a subarray and a planar wave model between subarrays;
- Option 2: PWM+SWM a planar wave model within a subarray and a spherical wave model between subarrays; and
- Option 3: SWM+SWM a spherical wave model within subarrays and a spherical wave model between subarrays.

Depending on the wave model, the distance and phase are calculated differently. PWM+PWM option assumes that all antenna elements have the same Tx-Rx distance, generates array steering vectors according to AoA and AoD, and generates different phases for each antenna element according to the array steering vector. The formula below shows how to calculate the phases using the array steering vector for a $Q^{(t)} \times Q^{(r)}$ MIMO channel.

$$P_{Q^{(t)} \times Q^{(r)}\ MIMO} = a^{(r)}\left(\Phi^{(r)}\right) a^{(t)}\left(\Phi^{(t)}\right)^{T} \tag{21}$$

where $a^{(t)}(\cdot) \in \mathbb{C}^{Q^{(t)} \times 1}$ and $a^{(r)}(\cdot) \in \mathbb{C}^{Q^{(r)} \times 1}$ are the Tx and Rx antenna array steering vectors, respectively.

In PWM + SWM option, the antenna elements in one receiving subarray have one distance from the other transmitting subarray, and the antenna elements in the subarray generate different phases using the array steering vector according to the AoA/AoD between the subarray pair. Thus, equation 21 can be used with reduced number of antennas only considering antenna elements in the subarray.

In SWM + SWM option, all transmit and receive antenna pairs have different distances, and the phase of each antenna pair is calculated by the distance between the antenna pairs. Equation 22 shows how to calculate the phase between the $q^{(r)}$ th receive antenna and the $q^{(t)}$ th transmit antenna.

$$P_{q^{(r)},q^{(t)}} = e^{j\frac{2\pi d_{q^{(r)},q^{(t)}}}{\lambda_k}}. \tag{22}$$

It is important to note that for LoS path, the distance between antenna elements and subarray can be calculated, but for NLoS path, the distance between antenna elements cannot be calculated based on ETSI TR 138 901 [i.1] approach. For NLoS path, the approaches described in previous clause can be used. Then the exact antenna position can be determined at the scatterer location. Option 1 can be used when the number of antenna elements is not very large and the bandwidth is not very large. Option 3 can be used in situations with very wide bandwidth and/or a very large number of antennas (reflective intelligent surface). Option 2 is an alternative method for situations similar to option 3 when the computational complexity becomes too large. However, the accuracy of option 2 needs to be further analysed.

5.4.2 Heterogeneous scattering modeling

The use of extremely large antenna arrays can lead to spatial non-stationary channel conditions. Note that in the ETSI TR 138 901 [i.1] CDL channel model, homogeneous scatterers (i.e. all antenna elements/sub-arrays observe the same number of scatterers) are used. In case the antenna arrays are large relative to the scatterer size, each subarray can observe a different scatterer. If this is the case, it is worth exploring non-stationary spatiotemporal channel coefficients for each Sub-Array (SA). Also, blockage for some clusters may be experienced by selected subarrays. Figure 11 illustrates an example of the heterogeneous scatter modeling. In Figure 11, a blocker is located between Rx subarray #n and scatterer #j, so Rx subarray #n cannot observe scatterer #j but Rx subarray #m can observe two scatterers.
In [i.179], heterogeneous scatterer modeling is captured, but there is a lack of evidence of its accuracy from the actual measurements. Details of how to model this effect and validation based on actual measurement or ray tracing can be further discussed.

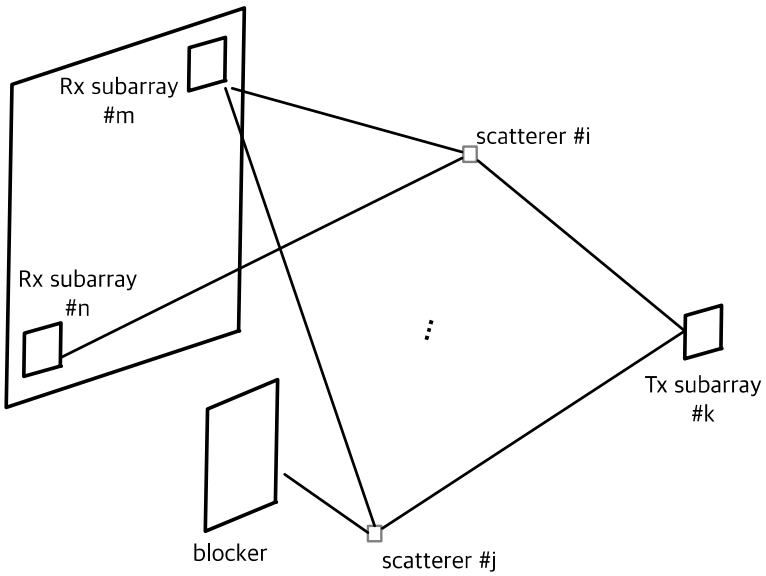

Figure 11: Heterogeneous scatterer modeling

5.5 Material characterization

5.5.0 Introduction

Most of the use cases that have been identified for THz communications apply to indoor environments, such as living rooms, factories, offices, and classrooms [i.69]. In these scenarios, reflection, diffraction, scattering, and penetration losses through walls and other objects can have a significant impact on wireless propagation. Given the relatively short wavelength, these effects are particularly relevant at THz frequencies [i.168].

5.5.1 Penetration loss of building materials

Table 5 summarizes the measurements contributed to the ETSI ISG THz, specifically for the purpose of characterizing the penetration loss of building materials.

Table 5: Measurement results for penetration loss of building materials

Organization	Material	Thickness	Centre frequency	Penetration Loss [dB]
Apple	Plywood	12,7 mm	39 GHz	5
			160 GHz	9
	Glass	2,38 mm	39 GHz	2
			160 GHz	4
	Drywall	12,7 mm	39 GHz	2
			160 GHz	11
	Aluminium Sheet	3,18 mm	39 GHz	35
			160 GHz	50
	Bricks	88,9 mm	39 GHz	28
			160 GHz	complete absorption
Durham Univ.	MDF	12 mm	25 GHz	1,98
			77 GHz	5,43
			153 GHz	7,25
	Wood Flooring	15 mm	25 GHz	4,02
			77 GHz	7,23
			153 GHz	11,26
	Gypsum Plasterboard	12,5 mm	25 GHz	1,06
			77 GHz	1,28
			153 GHz	1,28
	Plexiglass	4 mm	25 GHz	0,12
			77 GHz	0,71
			153 GHz	1,14
	hardboard (Plywood)	3 mm	25 GHz	1,35
			77 GHz	2,73
			153 GHz	4,64
	Single Glass	4 mm	25 GHz	1,46
			77 GHz	4,06
			153 GHz	5,96
	Double Glazed Glass	24 mm	25 GHz	13,27
			77 GHz	18,65
			153 GHz	23,06

Table 6 summarizes the penetration loss of indoor structures based on the measurement campaign conducted by Durham University. Indoor wall (1) refers to a wall between two offices, indoor wall (2) refers to a wall between office and corridor.

Table 6: Measurement results for penetration loss of indoor structures

Frequency	Glass door	Wooden door	Indoor wall (1)	Indoor Wall (2)
25 GHz	4,12 dB	10,17 dB	17,39 dB	26,64 dB
77 GHz	14,08 dB	21,21 dB	27,53 dB	38,40 dB
153 GHz	26,28 dB	41,97 dB	53,63 dB	59,17 dB

5.5.2 Dielectric properties of building materials

Table 7 summarizes the measurement results contributed to the ETSI ISG THz, specifically for the purpose of characterizing the penetration loss of building materials. Using the a, b, c, and d values provided in Table 7, it is possible to derive the real part of the dielectric constant (η') and the conductivity (σ) as a function of frequency using the following parametric models [i.79]:

$$\eta' = af^b$$
$$\sigma = cf^d$$

where f is the frequency in GHz and σ is in S/m. Figure 12 compares the amplitude and the phase of the transmission coefficient of the glass sample #1 measured and modelled using the derived parameters.

Table 7: Material properties

Material	a	b	c	d	Frequency range [GHz]
Glass (sample #1)	6,63	0	0,0011	1,51	100 - 400
Glass (sample #2)	6,50	0	0,0009	1,51	100 - 400
Glass (average)	**6,565**	**0**	**0,001**	**1,51**	**100 - 400**
Glass (ITU-R P.2040-3)	6,31	0	0,0036	1,3394	0,1 - 100
Glass (ITU-R P.2040-3)	5,79	0	0,0004	1,658	220 - 450
Pine	1,99	0	0,004	1,103	100 - 400
Birch	2,08	0	0,0053	1,10	100 - 400
Oak	2,05	0	0,0028	1,238	100 - 400
Wood (Average)	**2,04**	**0**	**0,004**	**1,1470**	**100 - 400**
Wood (ITU-R P.2040-3)	1,99	0	0,0047	1,0718	0,001 - 100
Plywood	**2,18**	**0**	**0,038**	**1,103**	**100 - 400**
Plywood (ITU-R P.2040-3)	2,71	0	0,33	0	1 - 40

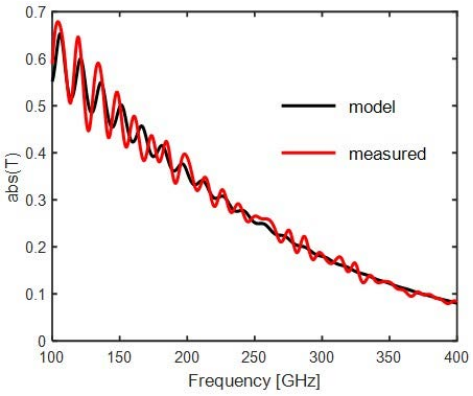

(a) Amplitude.

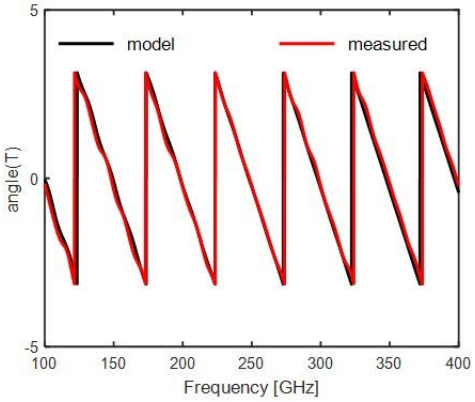

(b) Phase.

Figure 12: Transmission coefficient of the glass sample #1 measured (red lines) and modelled using the derived parameters (black lines)

5.5.3 Further resources

Herein further resources are listed for further study on: i) surface roughness ([i.94], [i.9]), electromagnetic characterization of building materials ([i.169], [i.170], [i.173]), and other materials ([i.171], [i.172]).

6 Channel measurements

6.1 Existing measurements published in relevant literature

Simulating electromagnetic propagation effects referred to as channel modelling provides insights into the behaviour of wireless systems and enables the development of innovative technologies. However, the accuracy and reliability of these simulations heavily rely on their alignment with real-world measurements. Considering electromagnetic propagation, where intricate interactions occur between electromagnetic waves and various mediums, simulations can offer predictions on signal propagation, interference patterns, and channel characteristics. Yet, without validation through measurements, these simulations risk inaccuracies that could lead to flawed designs and implementations.

Wireless channel sounding and measurements serve as crucial validation tools, allowing to compare simulated results with empirical data. This verification process not only ensures the fidelity of simulations but also enhances our understanding of complex physical phenomena. To this end, as an output generated by ETSI GR THz 001 [i.69] and ETSI GR THz 002 [i.72], clauses 4.1.2 and 4.2.2 provide an extensive survey of the existing literature. Specifically, ETSI GR THz 001 [i.69] identified 19 use cases and mapped them to physical environments, along with the resulting state of art literature on THz channel measurements per physical environment as listed in Table 1. Furthermore, Table 2 in clause 4.2.2 summarizes each of the physical environments, classifies them into frequency bands and indicates related THz channel measurement studies available in the existing literature for that particular environment.

6.2 Survey of existing open channel measurement datasets

Many funding agencies are requiring research data management plans for their funded projects. As a consequence, an increasing number of public funded projects are preparing to make research data originating from these projects publicly available. Recently, various research groups working on THz channel measurements have published their data covering channel impulse responses collected by channel sounders [i.92], [i.91], [i.95] [i.96], [i.99] as well as a database on material characteristics [i.93]. Such data will help the community to derive channel models and asses them using the same set of measurement data.

Aalto University and the University of Oulu have provided a package of a wideband Multiple-Input Multiple-Output (MIMO) stored radio channel model at 140 GHz in indoor hall, outdoor suburban, residential and urban scenarios. The package consists of measured wideband double-directional multipath data sets estimated from radio channel sounding and processed through measurement-based ray-launching and MATLAB code sets that allows users to generate wideband MIMO radio channels with various antenna array types [i.98]. The data is available in the Zenodo platform and is described in more detail in [i.99], [i.100].

Two data sets are available at the Research Data Management Platform of TU Braunschweig:

- [i.92] contains extracted multipath components from two different time-domain channel sounders in five scenarios: data centre, industrial environment, aircraft cabin, shopping mall, and conference room. The multipath components in all five scenarios are defined by amplitude, delay, angle of arrival. Additionally, the angle of departure is provided for the data centre and the aircraft scenarios. This published research data is explained and analysed in [i.89].

- The published data in [i.91] contains channel impulse responses measured in a real data centre and extracted multipath components of the propagation channel and the radio channel. A description of the measurement campaign and the evaluation is provided in [i.90]. Both double-directional channel measurements and Point-to-Point (P2P) radio channel measurements are conducted in Top-of-Rack and Medium Height scenarios Additional P2P radio channel measurements have been conducted for Intra-Rack setups. A more detailed description of the scenarios, the measurement set-up and the corresponding evaluations set-up is covered in [i.90].

Millimetre Wave and Terahertz Technologies Research Laboratories (MILTAL), Scientific and Technological Research Council of Turkey (TUBİTAK), Kocaeli, Turkey, has published two data sets at the IEEE data port platform:

- The measurements have been carried out in an anechoic chamber with the dimensions 7 m × 4 m × 3 m [i.95]. The dataset comprises channel impulse response in the frequency range 240 to 300 GHz for transmitter-receiver distances between 20 cm and 100 cm covering different misalignment degrees.

- The data set published in [i.96] has been derived in the same environment as used in [i.95]. A more detailed description of the scenarios, the measurement set-up and the corresponding evaluations set-up are covered in [i.97] targeting the modeling of the sub-terahertz communication channel via mixture of Gamma Distributions.

Philipps-Universität Marburg, Germany has published a data base with surface, transmission, reflection, and scattering characterization of 50 representative building materials based on fibre-couple THz time domain spectroscopy in the frequency range 0,1 to 1 THz [i.93] using the figshare repository. The description of the measurements and the derivation of the characteristics are published in [i.94].

RIKEN Centre for Advanced Photonics has maintained a spectroscopic database (https://www2.riken.jp/lab/tera/database-e.html) for THz bands since 2009, in cooperation with National Institute of Information and Communications Technology (NICT). The database covers a large number of materials including living organ tissues, polymer macro molecules, sugars, chemicals, various organic and inorganic materials including common building materials.

COST Action INTERACT is providing open data sets as well. The data available at https://interactca20120.org/wgs/datasets-2/ did not contain data above 100 GHz at the time of writing of the present document, but might be populated at a later stage with data of the frequency of interest.

7 Channel modeling

7.1 Modeling approaches

7.1.1 Deterministic Channel Modeling

7.1.1.0 Introduction

Deterministic channel modeling is obtained by approximating Maxwell's equations in a given environment and can achieve higher accuracy than statistical channel modeling. However, they require detailed information about the geometry and electromagnetic properties (dielectric constants, loss factors) of the environment and have higher computational complexity than statistical channel models.

7.1.1.1 Environment determination

The deterministic channel model requires detailed geometric information of the propagation environment, dielectric properties of the objects, and geometric information of the transmitter (Tx) and the receiver (Rx). For example, the size of the room and sizes and positions of indoor objects in the room need to be determined. The objects can be broadly categorized into static and dynamic objects. Static objects, such as furniture and home appliances (e.g. TV), have fixed positions. Depending on the scenario, dynamically moving objects such as people in a room can be modelled. In addition, the dielectric properties of the objects and walls need to be determined. For example, the permittivity and the conductivity of materials need to be determined for each object and wall. Finally, the location, antenna structure, and mobility of the Tx and the Rx need to be determined.

7.1.1.2 Ray tracing methods

In [i.77], the two commonly adopted approaches for ray tracing are the Image Method (IM) and the Shooting and Bouncing Ray (SBR) method.

The IM can be used to determine the ray path with multiple reflections. When the Tx and the Rx locations are given, the trajectory of a ray reflected from a plane surface can be determined by the IM. The procedure is as follows:

1) Determine the location of the image of Rx (Ri), where Ri locates the image of Rx with respect to the planar reflection surface.

2) Connect Tx and Ri to obtain a line segment which intersects the plane at a point Q. The reflected ray path can be determined by (Tx, Q, Ri).

However, the IM may not be efficient in an indoor environment due to a large number of reflection surfaces.

The SBR method was first introduced in [i.78] for the radar. Then it has been used in radio propagation modeling. The SBR comprises three steps, i.e. ray launching, ray tracing, and ray reception [i.77]. The procedure is as follows:

1) Ray launching: prior work in [i.77] demonstrated the effectiveness of the icosahedron ray-launching method, where an icosahedron with 20 identical equilateral triangular faces is created to assist in the launching of rays. This method characterizes the uniformity of the distribution of launched rays as well as provides significant topological information about different rays launched.

2) Ray tracing: When a ray is traced from the source location, it can go to the Rx point directly (i.e. an LoS path), or it can be reflected and diffracted several times before reaching the Rx point (i.e. NLoS paths). If the ray hits an object, a reflected or diffracted ray will be spawned. These ray-object intersection tests usually consume more than 90 % of computational time in a non-sophisticated implementation of the ray tracing algorithms. Significant research work has been done in accelerating the ray tracing algorithms [i.77].

3) Ray reception: The last step selects the most effective paths to test if the wavefront intersects the receiving antenna. To model this process, reception spheres are used. The radii of the spheres are determined by the distance between the signal transmitter and receiver, representing the cross-section of ray cones. If a centre ray intersects the receiver sphere, the cone it represents will contribute to the total electric field of the receiver.

7.1.1.3 Ray tracing on THz bands

1) **Effect of surface materials on THz bands:** The radio signal transmitted from a source will encounter multiple objects in the environment, forming reflected, diffracted, or scattered rays to the Rx. Ray tracing can have different results depending on the material properties of objects and it incorporates surface materials into the propagation loss calculations by using the complex relative permittivity of the surface. In [i.79] and [i.80], recommendations include methods, equations, and values used to calculate the relative permittivity for a range of frequencies. However, in those recommendations, the applicable frequencies for most materials are below 100 GHz. For THz bands, some material properties have been investigated [i.81], [i.82], [i.83] but need to be further investigated for more materials. Another aspect of material properties for THz ray tracing is the surface roughness of objects. The surface roughness is compared with the wavelength to distinguish "smooth" surfaces from "rough" surfaces in a specific frequency band [i.84]. When the wavelength is comparable to or smaller than the surface roughness, the surface is considered as "rough". Therefore, surfaces that are considered smooth at lower frequencies can be rough in the THz band [i.85]. When the incident wave encounters a rough surface, the reflected ray will radiate in the specular direction and the scattered rays will radiate in all other directions. Among these rays, specularly reflected rays are dominant in the THz band [i.9], while other scattering components are conjectured to have a strong impact on NLoS channels since the surface roughness becomes comparable with the wavelength, and thus the diffusely scattered power increases with increasing frequency. [i.9] suggests determining scattered rays by dividing the scattering surface into smaller square tiles around specular reflection points, with each tile contributing a scattered ray. Moreover, the correlation length of a rough surface is typically much greater than the wavelength in the THz band, thus sharp irregularities are not present. In [i.86], Kirchhoff scattering theory is introduced to determine modified reflection coefficient at THz bands. The Rayleigh roughness factor is:

$$\rho = e^{-\frac{g}{2}} \tag{23}$$

where g is calculated by:

$$g = \left(\frac{4\pi \cdot \sigma \cdot cos\theta_i}{\lambda}\right)^2 \tag{24}$$

where σ represents the roughness of materials, θ_i is the incident angle. Then the modified reflection coefficient can be demonstrated as

$$r' = \rho \cdot r \tag{25}$$

where r stands for the original Fresnel reflection coefficients, while r' is the modified reflection coefficient. Diffraction effects are assumed to be mostly negligible in terms of contribution to overall communication signal level at the receiver in THz bands, due to the extremely high diffraction loss in the THz band [i.85]; however, since they might be beneficial for describing the response of a sensed object, diffractions might need to be modelled for sensing applications [i.69].

2) **Molecular absorption:** Ray-tracing methods model the radio signal's line-of-sight, reflected, diffracted, or scattered rays to the Rx. This does not consider the molecular absorption effect. In THz band, the attenuation of electromagnetic wave propagation is also caused by the water vapor or gas, which causes numerous rotational and vibrational absorption lines across the entire electromagnetic spectrum. A modeling method of molecular absorption applicable to THz bands (clause 5.1) can be used for ray tracing-based channel modeling.

Based on the above discussion, the whole process of the deterministic channel modeling for THz bands is schematically shown in Figure 13.

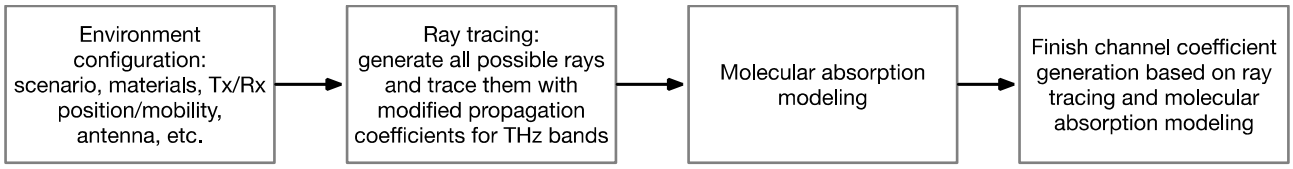

Figure 13: Process of deterministic channel modeling for THz bands

In summary, the process of the deterministic channel modeling for THz bands is (1) Environmental configuration, (2) ray tracing based on the modified propagation coefficients, (3) molecular absorption modeling, and (4) channel coefficient generation. Note that the last step is to generate channel coefficients by combining the previous two steps.

7.1.2 Hybrid Models

7.1.2.1 Hybrid deterministic/analytic channel model for low terahertz links

Deterministic ray-optical channel predictions require detailed 3D environment data. Due to the small wavelength in the order of millimetres and below, the environment data with all details taking the small wave length into account is usually not available. In [i.87], [i.88], it was shown that the geometrical parameters (Time Of Delay (TOD), Angle of Departure (AoD) and Angle of Arrival (AoA) can be predicted very well showing a good agreement between predictions and channel sounder measurements. However, the unavailability of the descriptions of the materials involved in the interaction with the rays yield significant inaccuracies of the predicted amplitudes of the rays.

To overcome these deficiencies and still exploit the advantages of predicting correctly the geometric properties, a new hybrid approach has been presented in [i.87], [i.88] for data centre applications. The hybrid model consists of a deterministic approach, which is enhanced by analytical aspects derived from measurements.

Deterministic aspects: standard ray-optical predictions are used to predict the geometric parameters TOD, AoA and AoD. The basis for this are accurate 3D models of the environment.

Analytical aspects are used in order to assign the values of the amplitudes to rays by the deterministic approach. In [i.89] a uniform analysis of 56 positions located in five different environments has revealed an exponential decay of the amplitudes of the Multipath Components (MPCs) in dB scale for all measurement positions. Based on this, the following function has been proposed:

$$G_{dB,norm,l} = \alpha \, (e^{-\beta l} - 1) \quad (26)$$

where l is the MPC index, α is a coefficient accounting for the minimum normalized path gain and β is a coefficient accounting for the slope. In this approach, the numbers of the MPCs are sorted by their path gain. α and β are values determined from channel measurements in the environment and frequency of interest differentiating also Line-of-Sight (LoS) and Obstructed Line-of-Sight (OLoS) conditions. The set-up consisting of the environment together with LoS/OLoS is called a class. In [i.87], [i.88] coefficients from three classes within a data centre are provided both for the propagation channel (excluding the antennas) and the radio channel (including the antenna). The final impulse response is then derived as follows: The normalized path gains are unnormalized with respect to the strongest path determined with the deterministic approach. In the next step the unnormalized gains are assigned to the MPCs from the ray-optical approach with the same MPC index l.

Figure 14 shows the various scenarios that have been measured in [i.90] and Figure 15 shows the measured MPCs for four different sets of Medium Height (MH) and Top-of-the-Rack (ToR) links in a Data Centre.

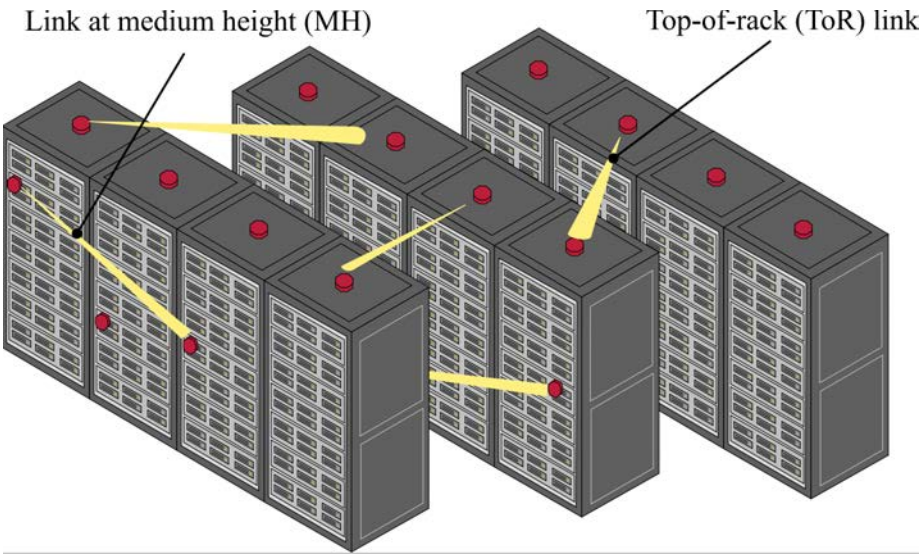

Figure 14: Configurations measured in a data centre (based on [i.90])

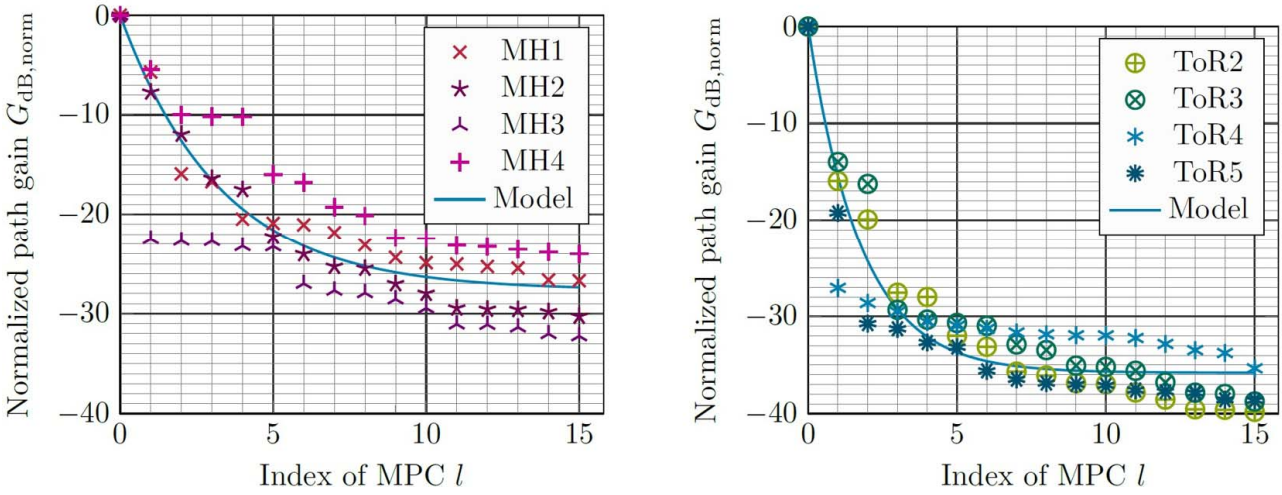

Figure 15: Measured MPCs and approximation by the hybrid model for double-directional propagation channel for the MH LOS (left; α = 27,66; β = 0,304) and the ToR LOS (left; α = 39,41; β = 0,306) classes (Source: [i.88] Copyright 2024 Shaker Verlag, reproduced with permission)

Although [i.87], [i.88] provide coefficients and the model validation has been done only for a data centre, the approach can be applied also to other scenarios, provided that α and b are values are determined by double directional channel sounder measurements.

7.2 Survey of existing channel models published in relevant literature

7.2.1 ETSI TR 138 901 channel model

7.2.1.0 Introduction

The ETSI TR 138 901 [i.1] model is popularly used for wireless system evaluations. The channel model provides an accurate and compatible probabilistic channel model for frequency bands ranging from 0,5 to 100 GHz. This is useful for designing, optimizing, and evaluating 5G system performance for various physical layer enhancements. It provides both a simpler stochastic channel model (e.g. CDL and TDL models) and a more complex map-based hybrid channel model in clause 8 of [i.1]. The set of channel models and parameterizations in ETSI TR 138 901 [i.1] have been widely used in 5G standardization and implementation.

The ETSI TR 138 901 [i.1] CDL model which is popularly used for MIMO simulation generates transmitter (Tx) and receiver (Rx) antenna geometries based on 3D coordinate systems, generates AoAs, AoDs, and delay parameters of multi-paths according to statistical characteristics or depending on scenarios, and then sums them to generate time domain channel coefficients. Figure 16 illustrates an example diagram of the ETSI TR 138 901 [i.1] model. Several AoAs/AoDs/delays for clusters and rays are generated based on statistics, and the channel coefficients are generated based on Tx and Rx array structures. Since channel coefficients are generated by using AoAs, AoDs, and delay values for multipath without directly generating the locations or antenna geometry of scatterers, this is called the non-geometry-based stochastic method. Thus, the ETSI TR 138 901 [i.1] model is less complex than the map-based hybrid channel model.

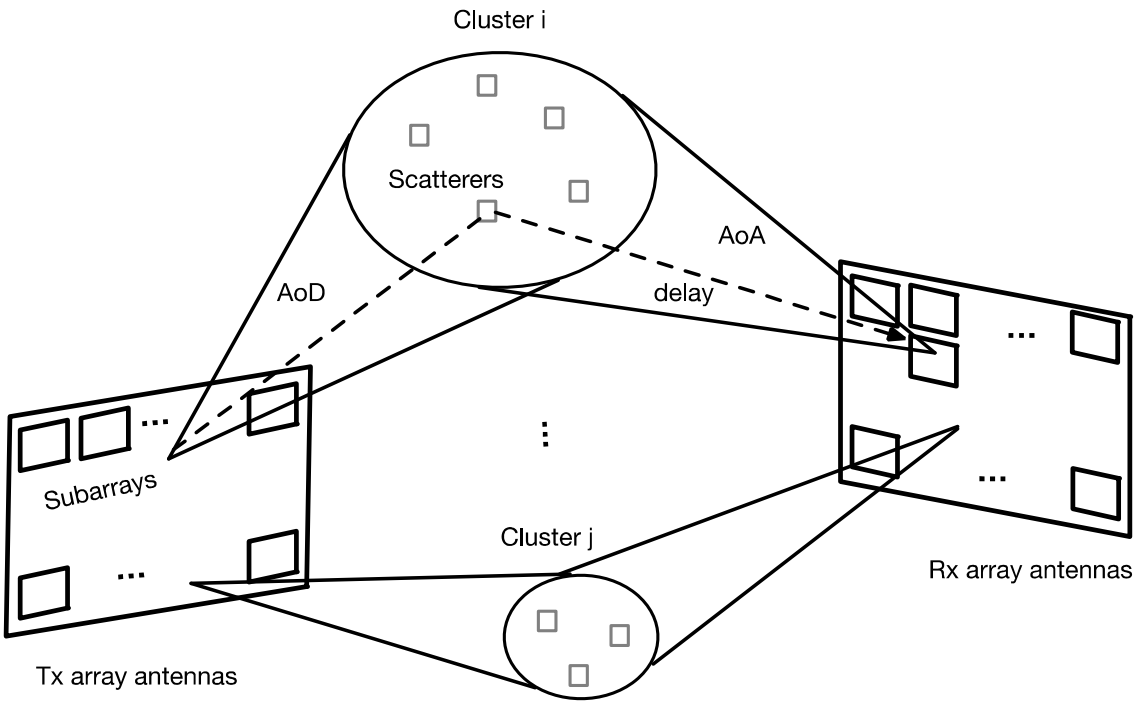

Figure 16: ETSI TR 138 901 model

The ETSI TR 138 901 [i.1] model has the following limitations to be reused for THz communication and THz sensing,

- Frequency range
- Planar wave modeling
- Considerations for modeling relatively large bandwidths
- Sensing channel modeling.

The following clauses discuss each limitation in detail.

7.2.1.1 Frequency Range

The ETSI TR 138 901 [i.1] model including the statistical characteristics such as pathloss, AoA, AoD, delay and oxygen absorption modeling, were derived based on measurements up to 100 GHz. Every statistical parameter and its generating methodology should be revisited for THz bands based on actual field measurements or ray tracing techniques.

7.2.1.2 Planar wave modelling

From [i.2], the far-field region is represented by the following equation:

$$R \geq \frac{2D^2}{\lambda_c} \text{ (Rayleigh distance)}, \tag{27}$$

where D is the maximum overall dimension of the antenna and λ_c is the wavelength of the carrier frequency. Since a relatively long range is often assumed compared to the antenna array size under 100 GHz, planar wave modeling (or far-field modeling) may be sufficient. However planar wave modeling may be inaccurate for THz channel modeling since the communication range can be less than the Rayleigh distance. In THz, the true spherical nature of wave propagation needs to be considered. For spherical wave modeling, the elements of channel matrix **H** can be found by direct distance calculation, i.e. considering the distance of the signal path between each of the Tx and Rx antennas, as opposed to planar wave modeling that models the channel based on a common distance between the antenna elements. This results in the following:

$$(\mathbf{H}(k))_{m,n} = e^{j\frac{2\pi r_{m,n}}{\lambda_k}}, \tag{28}$$

where $(\cdot)_{m,n}$ denotes the element in row m and column n, and $r_{m,n}$ is the distance between Tx antenna element n and Rx antenna element m, and k is the index of a subcarrier or a subband. Note that the spherical wave model may require distance calculation per each antenna element pair.

Figure 17 illustrates the planar wave model and the spherical wave model. In the planar wave model, AoA and AoD are used to generate phase terms of channel coefficients, and the wave propagation distance is used to determine propagation delay. In the spherical wave model, each distance between each Tx-Rx antenna pair contributes to the phase and the delay of each channel coefficient. The far-field assumptions may not be applicable in THz bands and distance calculations between individual antenna pairs may be required. This would increase computational complexity.

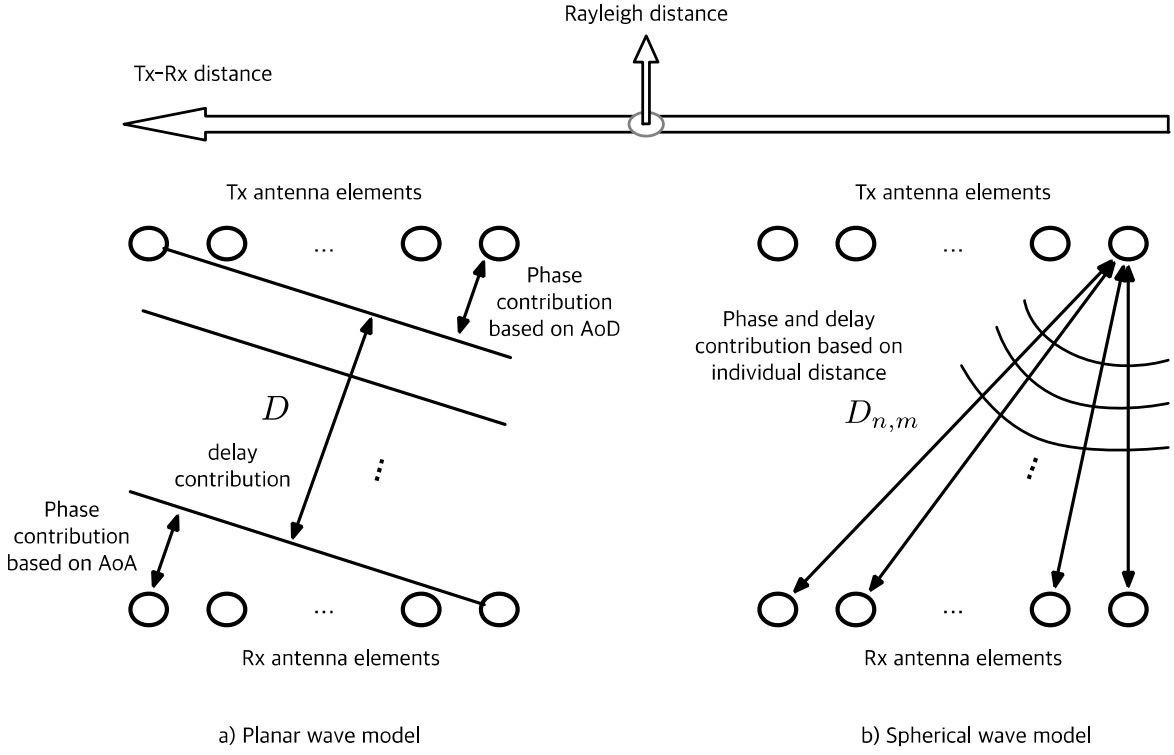

Figure 17: Planar and spherical wave models

7.2.1.3 Considerations for modeling relatively large bandwidths

In equation 28, the channel coefficient can be differently generated per subband/subcarrier due to the different wavelengths between different subbands/subcarriers. However, ETSI TR 138 901 [i.1] model uses the carrier frequency or wavelength of the carrier frequency used for channel gain and/or phase calculation. Since the fractional bandwidth and/or aperture to wavelength ratio can be larger at THz than that of lower frequency band, it is necessary to study the need for using subband-specific centre frequency depending on the considered RF architecture.

7.3 Channel modeling framework components and parameters

7.3.1 Path loss models

Based on the classification of the channel measurement scenarios in clause 4.1.2, Table 8 summarizes the measurements contributed to the ETSI ISG THz, specifically for the purpose of developing the path loss models. While further measurements have been contributed, the measurements in Table 8 represents those data sets that were combined to extract the path loss parameters.

Table 8: Measurement parameters for the data sets

Indoor / Outdoor	Scenario	LoS/ NLoS	Source	Centre Frequency of processed data (GHz)	BW of measurements (GHz)	Distance (m)	Antenna Polarization
Indoor	Office	LoS	Huawei	140	5	3,5 - 13,65	VV
				220	15	1 - 7	VV
			Durham	86	9	3,68 - 24,2	VV
				145	18	4,1 - 24,2	
				294	36		
	Corridor	LoS	Huawei	140	5	2 - 30	VV
				220	15	2 - 25	VV
				313	15	5 - 31	VV
			Durham	86	9	2,7 - 22,7	VV
				145	18	2,7 - 20,67	
				294	36		
	Factory	LoS	TUBS	304	8	5,5 - 11	VV
				304	8	5,5 - 15	
			Huawei	220	15	1 - 7	VV
			Durham	86	9	9,3 - 30,9	VV
				145	18		
				294	36		
			Fraunhofer IIS	305	5	3,48 - 9,27	VV + HH
Outdoor	Below rooftop Urban street	LoS	Huawei	140	5	3 - 25	VV
				220	15	3,45 - 25	VV
	Below rooftop Suburban street		Durham	86 145	9 18 36	6,3 - 79	VV

The data across the frequency bands indicated in Table 8 were combined per environment to estimate the ABG model parameters given in equation 29.

$$PL(f,d) = 10\alpha \log_{10}\left(\frac{d}{d_0}\right) + \beta + 10\gamma \log_{10}\left(\frac{f}{1\text{GHz}}\right) + X_\sigma \quad (29)$$

where α and γ are distance-dependent and frequency-dependent coefficients, respectively, β is an optimized offset parameter, f is the frequency in GHz, d_0 is the reference distance in m, and X_σ is Gaussian random variable with variance equal to σ. Figure 18 shows the fit to the data per environment with the estimated parameters of the model summarized in Table 9.

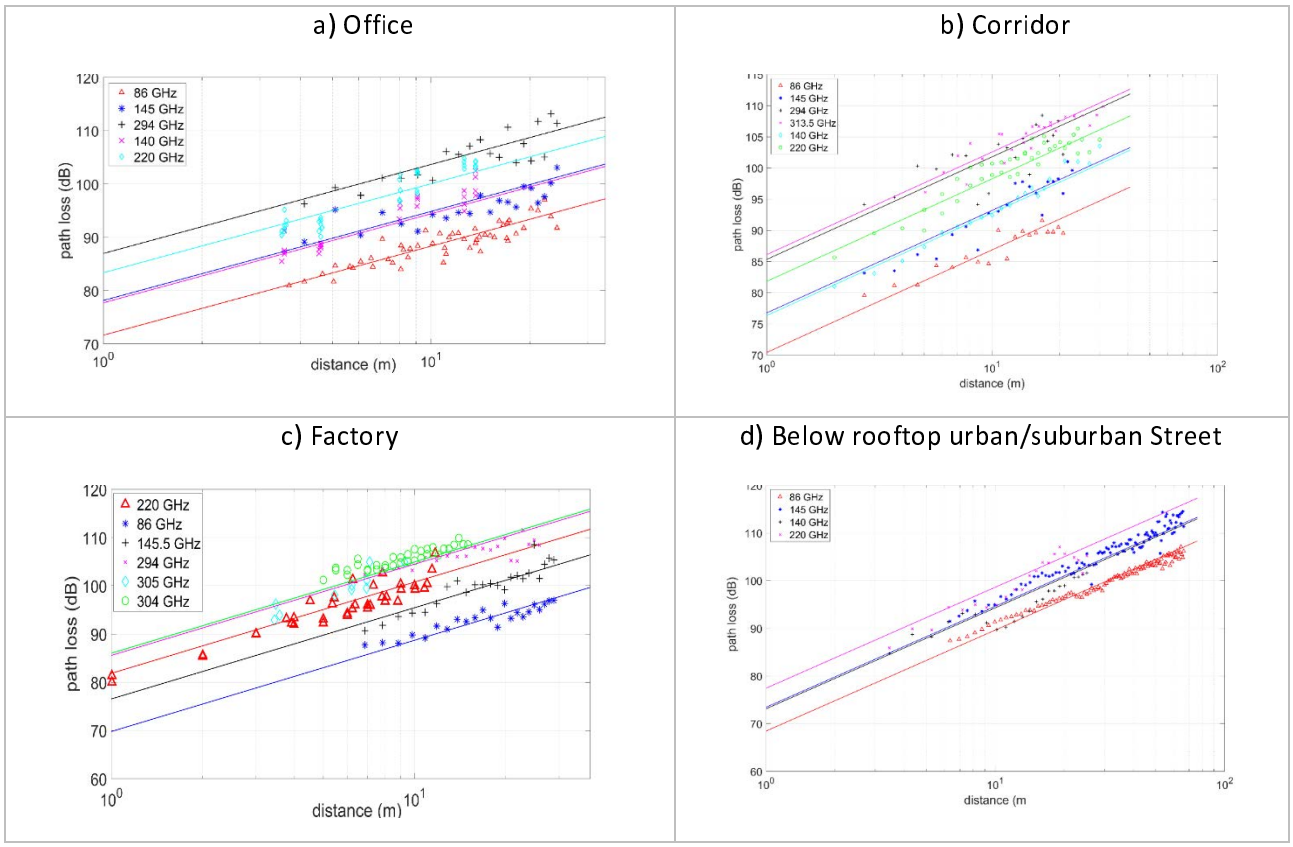

Figure 18: ABG Model fitting of the measurement data

Table 9: Estimated path loss parameters of the ABG model

Frequency (GHz)	Scenario	LoS/NLoS	Parameters (α, β, γ, σ)
86 - 294	Office	LoS	1,67, 16,1, 2,87, 2,12
86 - 313	Corridor	LoS	1,65, 16,4, 2,79, 1,95
86 - 305	Factory	LoS	1,89, 12,6, 2,96, 1,9
86 - 220	(Sub)urban street	LoS	2,12, 25,8, 2,2, 1,63

7.4 Channel modeling considerations for ISAC

7.4.1 Sensing channel modeling extensions for ETSI TR 138 901

ETSI TR 138 901 [i.1] channel model is designed for base station to UE communication link and thus lacks the sensing channel model aspects. The model is parameterized for a set of communication scenarios. Hence, various sensing scenarios such as monostatic sensing or bistatic sensing channels are not modelled which makes it unsuitable for some future use cases. The target modeling requirements are generally dependent on underlying performance requirements and particular Use Cases (UCs). The missing elements of the ETSI TR 138 901 [i.1] can be further observed given the potential sensing UCs, and the corresponding channel modeling requirements against the current state of ETSI TR 138 901 [i.1]. In particular, the following aspects can be identified:

- Various sensing scenarios support: depending on the device that transmits and/or receives sensing signal, mono-static sensing and bi-static sensing scenarios are considered. For mono-static sensing, mono-static gNB sensing and mono-static UE sensing need to be supported. For bi-static sensing, bi-static gNB-to-UE (or UE-to-gNB) sensing, bi-static UE-to-UE sensing and bi-static gNB-to-gNB sensing need to be supported. For these sensing scenarios, Large-Scale Parameters (LSPs) and Small-Scale Parameters (SSPs) are additionally defined for sensing channel generation. Depending on the type of target to be sensed and the use case, the altitude, RCS, LSP/SSP generation method, etc., of the target or device may be different.

- LoS/NLoS state determination for sensing channel: In most radar-based sensing channel modeling, it is assumed that a target exists (i.e. the channel between the target and the sensing device is LoS state). This may be sufficient for evaluating only sensing performance, but to evaluate performance from a system perspective and evaluate integrated sensing and communication performance, an actual channel model including NLoS between the sensing device and target is needed. The existing distance-dependent LoS/NLoS state decision probability model may be reused (in this case, the distance between the Tx device and the Rx device should be replaced with the distance between the sensing device and the target), or based on measurement or channel sounding, new models may be discussed for sensing LoS/NLoS state determination. Additionally, parameters such as Delay Spread (DS), Angular Spread (AS), Shadowing Factor (SF), Pathloss (PL), etc. may be determined differently depending on the LoS/NLoS state.

- Large Scale Parameters (LSPs) for sensing channel: DS, AS, SF, PL, and Ricean K factor (K) can be different from those of the communication channel. Figure 3 shows an example of different angular spread/distribution in communication and sensing channels. In a communication channel, since the base station and the UE have different antenna heights, it is desirable to use different angular distributions for AoA and AoD (see Figure 19). However, in the case of mono-static sensing, since the Tx and Rx are co-located and their antenna height are the same, the AoA and AoD should have the same distribution.

- Small Scale Parameters (SSPs) for sensing channel:

  - Cluster/Ray modeling for sensing channel: Deterministic or semi-deterministic Ray/cluster Modeling can be considered. Delay, gain, and echo angle for a direct path toward a sensing target are determined based on the physical location of a sensing target. Delays, gains, and angles for indirect paths toward the sensing target are generated based on a statistical manner based on measurement or sounding results. If the target is located very close to the sensing device, the near-field effect can also be considered. This may be seen as generating channels that include a single bounce toward/from the target and channels that have multi-bounces toward/from the target. If the sensing target creates one or more clusters and multiple rays exist within the one or more clusters, one of the rays corresponds to a direct path and the rest of the rays correspond to indirect paths. Based on them, a multi-path channel can be generated for a sensing target. There is also a need to discuss how the delay and angle of the target unrelated channel are generated. The channels generated by the surrounding environment or clutter can be distinguished from channels generated by targets. There is a need to further discuss how to generate clusters/rays generation for mono-static sensing and bi-static sensing. When implementing a cluster for a sensing object, it needs to be decided whether to generate a cluster for the sensing object in addition to the existing communication clusters or assign one or more clusters from the generated clusters for communication with the sensing object.

  - Effect of mobility: the device mobility is already modelled in communication channel modeling, but target mobility also needs to be considered.

- RCS consideration: RCS needs to be characterized for the relevant sensing targets/scenarios:

  - Different sensing targets such as humans, vehicles, or AGV/AMR (smart factory) may have different RCS values and human health signals (respiration/heartbeat channel signatures) may have different modeling approaches e.g. using micro-Doppler modeling or variational RCS values.

  - The channel modeling supports different related deployment scenarios (e.g. RCS characterization for various Tx/Rx position with respect to the sensing target).

  - For use cases involving target identification, posture recognition, orientation detection, etc., the geometry of sensing targets should be modelled. Instead of a single RCS value, the scattering field of a target can be modelled by multiple scattering centres with given relative locations and different RCS models. The expanded multi-scattering centre uses multiple scattering points to abstractly describe the electromagnetic scattering characteristics of the target, which can more accurately restore the amplitude and the shape information of the target.

- XPR for sensing channel: In mono-static sensing, even if the channel between the sensing device and the target is LoS, the channel itself should be modelled for reflected wave. Note that in a communication channel, an infinite XPR value is used for the LoS path (i.e. a diagonal matrix is used for an X-pol channel generation), but in a sensing channel, an XPR value of infinity should not be used for the direct path toward the sensing target, and the mean and variance of XPR may be different from those of communication channel. For bi-static sensing, reusing XPR values for communication channels can be considered.

- Consistency: Some use cases may require spatial/temporal consistency modeling. For example, assume a case where multiple devices cooperate to sense a single target. If the sensing channels of the two devices are generated independently, the cooperative sensing performance may be incorrectly estimated. If two devices are physically close together or a device or a target moves in limited space, their channel generation may also correlate. It is necessary to discuss how to make a correlation in LSPs and/or SSPs generation between spatial/temporal displacements.

- Environment target consideration: The interaction between the surrounding environment and sensing targets can be important for sensing performance evaluation. The specular reflections can take a large portion in the received power, which contain explicit geometry information between sensing target, Tx, Rx, and other objects. For example, the reflection paths can be exploited to create a virtual TRP to improve the localization accuracy for target localization and tracking. The major objects, such as buildings are considered as environment targets. The interaction between sensing target and environment target, and the interaction between environment targets should be deterministically modelled.

- Frequency range limitation for sensing: ETSI TR 138 901 [i.1] model has a limitation of frequency range up to 100 GHz. For sensing UCs, this needs to be extended to THz bands.

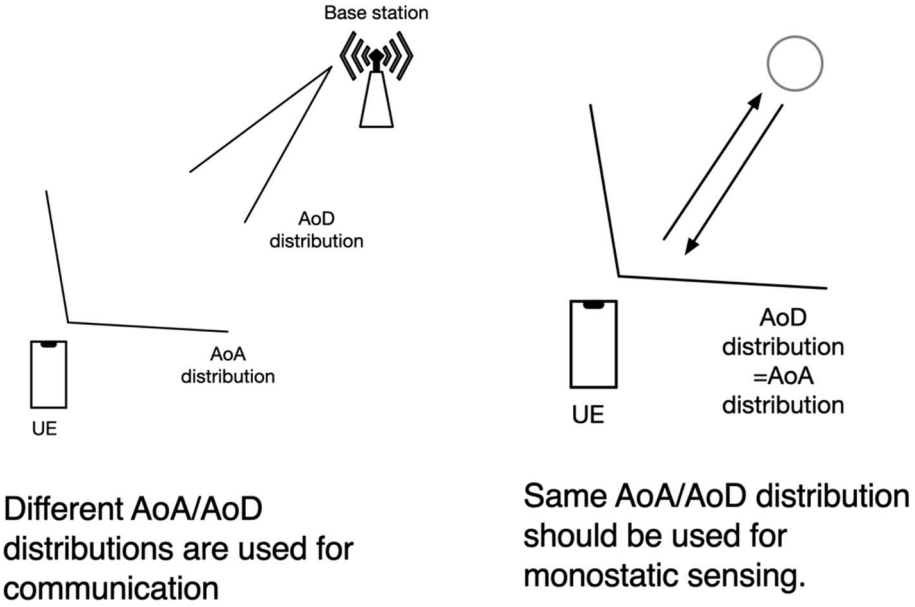

Figure 19: Different AoA/AoD distribution for communication and sensing

7.4.2 3GPP ISAC channel modelling study item

To address some of the sensing-related channel modeling extensions for ETSI TR 138 901 [i.1], 3GPP RAN has approved a Study Item (SI) for ISAC channel modelling, led by 3GPP RAN1 [i.180], which is ongoing and is planned to be finalized in May 2025. This SI aims to:

- Identify the details of the deployment scenarios for ISAC.

- Define channel modelling details for sensing using ETSI TR 138 901 [i.1] channel model as a starting point, and taking into account relevant measurements, including:

  - modelling of sensing targets and background environment, including, for example, Radar Cross-Section (RCS), mobility and clutter/scattering patterns;

  - spatial consistency.

The SI aims at a common modelling framework capable of detecting and/or tracking the following five types of objects and to enable them to be distinguished from unintended objects:

- UAVs.

- Humans indoors and outdoors.
- Automotive vehicles (at least outdoors).
- Automated guided vehicles (e.g. in indoor factories).
- Objects creating hazards on roads/railways, with a minimum size dependent on frequency.

Furthermore, sensing related terminology including the sensing transmitter and receiver, sensing target, sensing signal, mono-static, bi-static are discussed by the SI, with the deployment configurations of each sensing target discussed separately.

For ISAC channel modelling methodology study, a common framework for ISAC channel model is composed of a component of target channel and a component of background channel is firstly defined:

$$H_{ISAC} = H_{target} + H_{background},$$

where target channel H_{target} includes all multipath components impacted by the sensing target(s) and background channel $H_{background}$ includes other multipath components not belonging to target channel.

Unlike the communication channel, the sensing channel is target-oriented and the sensing target splits the propagation channel into two links, i.e. the Tx-ST (sensing target) link and the ST-Rx link. For target channel modelling, a concatenation approach has been adopted to generate the end-to-end target channel and the complexity of the concatenation should be controlled when indirect paths are modelled in the target channel. For the indirect path, except the traditional stochastic clusters are considered in the indirect path of the target channel, discussions are ongoing on modelling the Environmental Object (EO) in the target channel by a deterministic method, which helps to address the 'ghost target' issue and improve the sensing performance in the NLoS condition. The EO and/or stochastic cluster are considered to model the indirect path of the target channel if applicable. The modelling method of EO and stochastic cluster can be referred to clauses 7.6.8 and 7.5 in ETSI TR 138 901 [i.1] respectively.

In some scenarios (e.g. vehicle detection), measurement results show that the RCS of the target can be observed dependent on the incident and scattering angle, indicating that the sensing target can be modelled by multiple scattering points. On the other hand, in scenarios related to UAV detection, measurement results show that the RCS of the target can be observed as an omni-directional mean value with small random variation, thus indicating that the sensing can be modelled as a single scattering point. For the bi-static background channel, ETSI TR 138 901 [i.1] and the current 3GPP Technical Reports (TRs) such as TR 37.885 [i.181] and TR 36.777 [i.182] can be used as a starting point, with new approaches not precluded.

Following the finalization of the 3GPP SI on ISAC channel modeling, the ETSI ISG THz plans to build on top of the work to address the THz-specific considerations for ISAC within the scope of the ETSI TR 138 901 [i.1] channel modeling framework.

7.5 Channel modeling considerations for RIS

7.5.1 Introduction

RIS can adjust how signals propagate through controlled reflection and scattering. These surfaces are composed of meta-material elements that can be reconfigured in real-time to alter signal phase and amplitude, aiding in overcoming challenges like high path loss at THz frequencies. The use of RIS in the THz band has the potential to support next-generation wireless systems, improving data transmission efficiency and enabling reliable communication for 6G and beyond.

7.5.2 ETSI GR RIS 003 channel models

In ETSI GR RIS 003 [i.174], RIS channel models are developed and characterized. ETSI GR RIS 003 [i.174] summarizes how the existing ETSI TR 138 901 [i.1] channel modeling is applied to the RIS link, near and far field pathloss models, RIS channel multipath model, reradiation model, and interference and unwanted reradiation models. ETSI GR RIS 003 [i.174] outlines various path loss models applicable also to THz and sub-THz RIS-based systems:

- **General Path Loss Model** ([i.174], clause 6.3.1.1): The BS-RIS-UE cascaded channel can be modelled as a function of transmit/receive antenna gains, RIS element gains, reflection coefficients, and the distances between the RIS elements and the transmitter/receiver. This model is versatile and applicable to both near-field and far-field scenarios.

- **Near-Field Path Loss Model** ([i.174], clause 6.3.1.3): In near-field conditions, contributions from different RIS elements are modelled separately in terms of distances and phase shifts. This model is useful for initial estimations and can be refined with specific propagation conditions.

- **Far-Field Path Loss Model** ([i.174], clause 6.3.1.4): When the transmitter and receiver are in the far-field of the RIS, the path loss expression can be further simplified (based on free-space path loss model).

ETSI GR RIS 003 [i.174] addresses multipath scattering and reradiation effects, which are critical in sub-THz and THz frequency bands, e.g.:

- **Multipath Models** ([i.174], clause 6.5): Discusses unstructured and structured multipath models, particularly for high-frequency bands. These models consider the complex interactions between incident waves and the RIS, including scattering, reflection, and diffraction.

- **Multi-Mode Reradiation** ([i.174], clause 6.6): Models for multi-mode reradiation describe how RIS elements contribute to interference and unwanted reradiation, including both in-band and out-of-band effects.

However, in [i.174], the polarization effect is not much discussed. RIS has mainly been regarded as a scatterer in a wireless environment. When Electromagnetic (EM) waves interact with RIS, they interact with two types of material interfaces: metal and substrate, which can be designed as the two types of EM controlling methods for RIS. The first EM controlling method for RIS utilizes the antenna resonant mode corresponding to the resonant length on the metal plate. The second EM controlling method for RIS uses the controllable properties of substrate material, and the current technology for this method is based on Liquid Crystals (LCs) which is not widely used in RIS since designing and controlling LCs is challenging. The level of matched polarization among antennas of the transmitter, receiver, and RIS significantly affects the received power.

7.5.3 Polarization effect modeling of RIS channel

Channel models discussed in ETSI GR RIS 003 [i.174] are not sufficient for polarization channel effect modeling. This clause discusses how to model the polarization effect of RIS channel. Figure 20 illustrates the RIS channels when RIS is deployed.

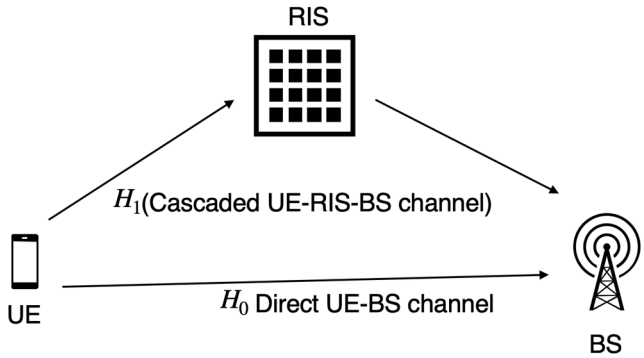

Figure 20: RIS channels

In the stochastic modeling of ETSI TR 138 901 [i.1], the LoS and NLoS status of the first hop and the second hop are determined by using a probability model according to the distance to determine the state of LoS/NLoS, and the large-scale parameters and small-scale parameters are determined according to the LoS or NLoS state. Before formulating channel response, the antenna field response **E** for azimuth angle θ and elevation angle ϕ can be formulated as follows:

$$\mathbf{E}(\theta,\phi) = [\mathrm{E}^{\mathrm{V}}(\theta,\phi), \mathrm{E}^{\mathrm{H}}(\theta,\phi)]^{\mathrm{T}} \tag{30}$$

where E^{V} and E^{H} are vertical and horizontal antenna responses respectively at the given angle θ and ϕ. The channel for a path can be formulated as:

$$\mathrm{H}^{\mathrm{t,r}} = \sqrt{\mathrm{P}^{\mathrm{t,r}}}\mathbf{E}^{\mathrm{r}}(\theta^{\mathrm{r}},\phi^{\mathrm{r}})^{T}\mathbf{M}\mathbf{E}^{\mathrm{t}}(\theta^{\mathrm{t}},\phi^{\mathrm{t}})\mathrm{e}^{-\mathrm{j}(\varphi^{\mathrm{t}}+\varphi^{\mathrm{r}}+\sigma^{\mathrm{t,r}})} \tag{31}$$

where $\mathrm{P}^{\mathrm{t,r}}$ is the pathloss, $\mathbf{E}^{\mathrm{r}}$ and $\mathbf{E}^{\mathrm{t}}$ are transmit and receive antenna responses, respectively, **M** is a transformation matrix of polarization response, $(\theta^{\mathrm{r}},\phi^{\mathrm{r}})$ and $(\theta^{\mathrm{t}},\phi^{\mathrm{t}})$ are AoA and AoD angles, respectively, φ^{t} and φ^{r} are initial phases of the transmit antenna and receive antenna respectively, and $\sigma^{\mathrm{t,r}}$ is a phase rotation due to traveled wave. In equation (31), if the path is LoS or direct, $\mathbf{M} = \begin{bmatrix} 1 & 0 \\ 0 & -1 \end{bmatrix}$, if the path is NLoS or indirect path, $\mathbf{M} = \begin{bmatrix} e^{j\phi^{VV}} & \sqrt{\kappa^{-1}}e^{j\phi^{VH}} \\ \sqrt{\kappa^{-1}}e^{j\phi^{HV}} & e^{j\phi^{HH}} \end{bmatrix}$, where κ is a Cross Polarization power Ratio (XPR), ϕ^{VV}, ϕ^{VH}, ϕ^{HV}, and ϕ^{HH} are initial phase values for different polarization combinations.

To model polarization efficiency in RIS channel, Radar Cross Section (RCS) of RIS [i.175] are considered. The RCS of RIS is comprised of two components: Antenna Mode (AM) RCS and Structural Mode (SM) RCS. The AM-RCS originates from the reradiation of antennas under an incident wave, which is related to the radiation performance and loads of the antennas. The SM-RCS is the remainder of the total RCS to remove the AM-RCS. Consequently, the SM RCS always exists while the AM-RCS can be tailored by the incident EM wave. For the AM-RCS, the signal received by the RIS is affected by the polarization efficiency. To account for this, the cascaded channel for the RIS is formulated as:

$$\mathrm{H}_{AM}^{\mathrm{RIS}} = \sqrt{\mathrm{P}^{\mathrm{r,RIS}}\mathrm{P}^{\mathrm{RIS,t}}}$$

$$\underbrace{\mathbf{E}^{\mathrm{r}}(\theta^{\mathrm{r,RIS}},\phi^{\mathrm{r,RIS}})^{T}\mathbf{M}^{\mathrm{r,RIS}}\mathbf{E}^{\mathrm{RIS}}(\theta^{\mathrm{RIS,r}},\phi^{\mathrm{RIS,r}})}_{RIS\rightarrow r}$$

$$\boldsymbol{\Gamma}\cdot\underbrace{\mathbf{E}^{\mathrm{RIS}}(\theta^{\mathrm{RIS,t}},\phi^{\mathrm{RIS,t}})^{T}\mathbf{M}^{\mathrm{RIS,t}}\mathbf{E}^{\mathrm{t}}(\theta^{\mathrm{t,RIS}},\phi^{\mathrm{t,RIS}})}_{t\rightarrow RIS}$$

$$e^{-j\left(\varphi^{\mathrm{t}}+\varphi^{\mathrm{r}}+\varphi^{\mathrm{RIS}}+\sigma^{\mathrm{RIS,r}}+\sigma^{\mathrm{RIS,t}}\right)}, \tag{32}$$

where $\boldsymbol{\Gamma}$ is the RIS reflection coefficient matrix, φ^{RIS} is the initial phase from the antenna of RIS element, $\mathrm{P}^{\mathrm{r,RIS}}$ and $\mathrm{P}^{\mathrm{RIS,t}}$ are the pathloss from the RIS to receive antenna and from the transmit antenna to RIS, respectively, $\mathbf{M}^{\mathrm{r,RIS}}$ and $\mathbf{M}^{\mathrm{RIS,t}}$ are the polarization transformation matrices from RIS to receiver antenna and from transmitter antenna to RIS element. If RIS can tune RIS reflecting phase and amplitude in each component of the polarization channel, $\boldsymbol{\Gamma}$ can be non-diagonal matrix but if not, $\boldsymbol{\Gamma}$ is a diagonal matrix. In (3), the transformation of polarization corresponding to the AM-RCS of RIS can be captured by:

$$\mathbf{M}_{\boldsymbol{AM-RCS}} = \mathbf{E}^{\mathrm{RIS}}(\theta^{\mathrm{RIS,r}},\phi^{\mathrm{RIS,r}})\cdot\boldsymbol{\Gamma}\cdot\mathbf{E}^{\mathrm{RIS}}(\theta^{\mathrm{RIS,t}},\phi^{\mathrm{RIS,t}})^{T}.$$

By using this expression, equation 32 can be rewritten as:

$$\mathrm{H}_{AM}^{\mathrm{RIS}} = \sqrt{\mathrm{P}^{\mathrm{r,RIS}}\mathrm{P}^{\mathrm{RIS,t}}}\cdot\mathbf{E}^{\mathrm{r}}(\theta^{\mathrm{r,RIS}},\phi^{\mathrm{r,RIS}})^{T}\mathbf{M}^{\mathrm{r,we\ RIS}}\mathbf{M}_{\boldsymbol{AM-RCS}}\mathbf{M}^{\mathrm{RIS,t}}\mathbf{E}^{\mathrm{t}}(\theta^{\mathrm{t,RIS}},\phi^{\mathrm{t,RIS}})$$

$$e^{-j\left(\varphi^{\mathrm{t}}+\varphi^{\mathrm{r}}+\varphi^{\mathrm{RIS}}+\sigma^{\mathrm{RIS,r}}+\sigma^{\mathrm{RIS,t}}\right)}.$$

To model the polarization effect of the SM-RCS of RIS, the transformation of polarization for the scattered and reflected waves can be introduced, respectively:

$$\mathbf{M}_{sca} = \begin{bmatrix} S^{VV} & S^{VH} \\ S^{HV} & S^{HH} \end{bmatrix}, \mathbf{M}_{ref} = \begin{bmatrix} R^{\perp} & 0 \\ 0 & R^{\parallel} \end{bmatrix},$$

where the parameters are functions of the plate size and angles of the incident, scattered, and reflected waves [i.176]. The transformation of polarization corresponding to the SM-RCS of RIS can be expressed as:

$$\mathbf{M}_{SM-RCS} = \mathrm{c}_s \mathbf{M}_{sca} + \mathrm{c}_r \mathbf{M}_{ref},$$

where c_s and c_r are the tuning coefficients for the scattered and reflected fields, respectively. An overall channel in consideration of all polarization matrices can be formulated as follows:

$$\mathrm{H}_{AM+SM}^{\mathrm{RIS}} = \sqrt{\mathrm{P}^{\mathrm{r,RIS}}\mathrm{P}^{\mathrm{RIS,t}}} \cdot \mathbf{E}^{\mathrm{r}}(\theta^{\mathrm{r,RIS}}, \phi^{\mathrm{r,RIS}})^{T} \mathbf{M}^{\mathrm{r,RIS}} (\mathbf{M}_{AM-RCS} + \mathbf{M}_{SM-RCS}) \mathbf{M}^{\mathrm{RIS,t}} \mathbf{E}^{\mathrm{t}}(\theta^{\mathrm{t,RIS}}, \phi^{\mathrm{t,RIS}})$$

$$e^{-j\left(\varphi^{\mathrm{t}}+\varphi^{\mathrm{r}}+\varphi^{\mathrm{RIS}}+\sigma^{\mathrm{RIS,r}}+\sigma^{\mathrm{RIS,t}}\right)}. \quad (33)$$

From equation 33, the following conclusions can be made:

1) In RIS channel, there are three different components affecting the polarization effect:

   a) $\mathrm{M}^{\mathrm{RIS,t}}$: polarization transformation from the channel between Tx and RIS;

   b) $\mathrm{M}_{AM-RCS} + \mathrm{M}_{SM-RCS}$: polarization transformation on RIS; and

   c) $\mathrm{M}^{\mathrm{r,RIS}}$: polarization transformation from the channel between RIS and Rx.

2) Even though both links (UE->RIS, RIS-> BS) have the LoS state, the overall polarization transformation matrix (i. e. $\mathrm{M}^{\mathrm{r,RIS}}(\mathrm{M}_{AM-RCS} + \mathrm{M}_{SM-RCS})\mathrm{M}^{\mathrm{RIS,t}}$) is not diagonal. This means RIS channel can have a smaller XPR value.

3) M_{AM-RCS} is a function of the reflection coefficient which is related to hardware design. This can be different between active RIS and passive RIS. Practical hardware design can be taken into consideration for RIS channel modeling.

4) M_{SM-RCS} is related to the scattered and reflected waves on the surface of RIS. This term can be modeled by ray tracing or actual channel measurement.

7.6 Machine learning models to generate and analyse radio channels

7.6.1 Introduction

Understanding and modelling wireless channels is the key to wireless communication systems. In ETSI TR 138 901 [i.1], analytical models are proposed for modelling wireless channels in the frequency range of 0,5 GHz to 100 GHz. As the number of devices increases in wireless communication systems, and devices being deployed in a variety of environments, generating an analytical model fitting all kinds of scenarios becomes challenging. However, along with the increasing complexity of wireless channels, it is also possible to collect a multitude of traces of communication activities, which indicates the patterns and features of the corresponding communication system. With Machine Learning (ML) techniques, the underlying information from the traces can be extracted and further applied to guide the parameter settings and resource allocation in the wireless communication system. For frequency band as THz, where analytical model is under-developed, ML techniques can serve as a novel method to discover unknown characteristics of the channel.

In the present document, three categories of ML applications to THz wireless channel modelling are identified. With regard to the specific application, three different types of ML techniques/models are analysed, with focus on their improvements compared to classic analytical models and also their limitations.

7.6.2 Application of ML to Channel Modelling

7.6.2.1 Scenario Identification

Scenario identification in the context of classification of Line of Sight (LoS) and Non-LoS (NLoS) channels is essential to applications involving localization tasks and to channel modeling in general. In particular, LoS channels are fundamental to the realization of THz communication, and knowing the presence of a LoS link might impact the feasibility of communication over THz frequencies. For instance, in the absence of a LoS link, a system designer might resort to multi-hop communications (either through active nodes or through RISs) or relays with different mediating protocols to guarantee per-link LoS conditions.

Scenario identification is a challenging task for a mobile device due to the complexity of the existing methods. For instance, He et al. [i.110] propose a visual inspection solution based on recorded video footage, which demands high complexity of computation and indicates other means for scenario identification could be more practical. Existing ML-based scenario identification approaches in the literature exploit the variation of the channel statistics to perform the identification task. Amplitude-based solutions using Support Vector Machines (SVM) algorithms have been proposed to perform scenario identification [i.111] based on the maximum amplitude of the channel, while in [i.112], the authors compare random forest, artificial neural networks and SVM algorithms using features such as the maximum amplitude, the kurtosis function, the Ricean K-factor, the skewness, and features that exemplify time-varying characteristics of the channel such as the angular variance. The importance of the type of features used in scenario identification were stressed in [i.113], where the authors attributed the performance gains, compared to the approach in [i.111], to the inclusion of angular information in the feature set. Authors in [i.114] consider the impact of training settings, such as the training data size and the number of hidden layer nodes, on the classification accuracy.

Going beyond LoS/NLoS classification, authors in [i.115] test the accuracy of several ML-based models on the task of indoor environment classification based on density and ranging from highly cluttered to open space. Results show that the k-NN model can achieve above 99 % classification accuracy in case of four clutter levels.

7.6.2.2 Channel Prediction

7.6.2.2.1 Large-Scale Propagation and Radio Map Generation

Given a target coverage area, it is beneficial to have knowledge on the quality of coverage so as to adjust the design or improve the communication system. However, to get a precise description of the channel characteristics, such as path loss in a large area, the common approach of ray tracing entails high computational costs. To this end, combined with the recent advancement in computer vision, researchers have been working on using mature computer vision techniques to directly generate maps of radio resources given the 2D image description of the scenes as input.

In [i.116], satellite photos of a suburban area are pre-processed to explicitly represent the locations of buildings and other objects, then fed as input to generate the receiver signal strength at a single location by the Convolutional Neural Network (CNN). Specifically, the receiving antennas' information is also encoded in the structure of the CNN. Levie et al. [i.117] adopted a similar approach, but with a complete radio map as output and simulated data for training and evaluating. Ates et al. [i.118] firstly categorize the path loss parameters and then applied CNN to classify the input scenarios represented by satellite images. In [i.119], CNN is applied to generate high-resolution radio maps on multiple metrics, based on the low-resolution images generated by fast but low-granularity simulation.

In THz communication, where the channel exhibits high directivity and suffers from blockage, the radio map generation techniques mentioned above are expected to identify direction and blockage more quickly than iterating on all possible rays as in ray tracing methods. Furthermore, recent advancements in computer vision of 3D point clouds also provides the possibility in generating "radio space" given the point clouds of a scene as input. For high frequency communication such as THz where the range of communication could be relatively short and heavily relying on LoS, using ML techniques in 3D vision might facilitate the generation of channel models in 3D scenarios.

Pathloss prediction by training a Random Forest (RF) on real measurement data for vehicle-to-vehicle communications was performed in [i.120]. The results showed that, for both location dependent (e.g. using geographical descriptors) and location independent modeling, RF can achieve better prediction than traditional log distance path loss model used on the same data.

7.6.2.2.2 Gain Prediction in Multi-Channel Scenarios

The ability of ML techniques to model non-linearities can also be applied to the scenario of small scale fading in wireless communication. In a fixed setting where the channels at each subcarrier are correlated but not identical, they can be modelled or predicted as matrices where the correlations of the subcarriers components can be captured by ML. In [i.121], the subcarriers in OFDM of a MIMO channel is modelled as a three-dimensional matrix as the learning objective. The tentatively estimated channel matrix in the same format is taken as input to the ML model. In this case, the ML serves as a fine tuner for the estimation of channel information. Yuan et al. [i.122] proposed to use CNN to model the autocorrelation function of a time-varying MIMO channel. Two approaches are compared and evaluated. The first one uses the estimated autocorrelation factors as input to yield corrected correlation vectors. The second approach leverages the temporal characteristics of recurrent neural network and is relaxed from the estimation steps as in the first approach since the output of the neural network is used as input in the next step. Furthermore, Kim et al. [i.123] compared the performance of Kalman Filters and machine learning in predicting MIMO channels. The neural network deployed is multi-layer perceptron and the authors allow variable complexity of input signals, which is dependent on the time range of the available old channel state information. In [i.124], different recurrent units are implemented in neural networks and compared for predicting the gains of flat fading MIMO channels. All of the above techniques, while potentially providing performance benefits, require considerably higher computing resources (in particular, in the training phase) than the traditional (statistical) methods.

7.6.2.3 Clustering of Multi-Path Components

Typically, channel models assume that wireless propagation happens through a finite number of multipath components, each representing a plane wave travelling along a different path. Each multipath component is characterized by its complex amplitude, delay, direction of arrival and departure. Typically, multipath components that exhibit similar characteristics are grouped into a cluster. In this context, different ML techniques have been exploited to identify clusters in an automatic manner. In [i.125], authors presented the KPowerMeans, a variant of the popular K-means algorithm which accounts for the power of multipath components to compute clusters centroids. The same algorithm was used in [i.126] and [i.127] for the identification of multipath clusters at mmWave and THz frequencies. Li et al. [i.128] collected channel measurements at THz frequencies and applied the DBSCAN algorithm [i.129] to identify the multipath clusters. Chen et al. [i.130] exploited THz channel measurements and ray tracing simulations for clustering and matching of multipath components. First, the multipath components observed in real measurements are clustered using the DBSCAN algorithm. Then, the identified clusters are matched with those observed in a ray tracing simulator based on the Multipath Component Distance (MCD) metric. In [i.131], authors proposed a clustering algorithm that identifies independent clusters based on a kernel density measure. In [i.132], a novel clustering approach based on Fuzzy-c-means is presented. In [i.133], authors proposed a new clustering algorithm based on the region competition algorithm [i.134], an optimization technique originally developed for image segmentation, and the kurtosis measure. In [i.135], clustering is treated as a sparsity-based optimization problem which exploits the physical property that the power of multipath components decreases exponentially with respect to the delay.

In [i.107], simple clustering algorithms were applied to THz measurement data to separate and group Multi-Path Components (MPCs), without manually identifying the peaks in the received signals. The techniques are especially useful for signals in THz band thanks to the clear separation of peaks due to the faster attenuation of signals at higher frequencies. Further work includes automated setting of the clustering-related parameters, as well as extending the extracted MPC information to include the departure/arrival angles of the MPCs.

7.6.3 ML Techniques and Models

7.6.3.1 Discriminative Models

Discriminative models take environmental parameters as input and output channel information. In this case, ML models, especially neural networks, are used to find the fit for the non-linear relationships between the input parameters, e.g. transmitter/receiver location and blockage information provided by the models of the propagation environment. Most of the applications in clause 7.6.2.2 are exemplary of this format of ML deployment.

One application of discriminative models is to generate radio maps. In this case, the input is the geographical information of a certain area. The ML model assigns a specific (scalar) value such as a receiving signal strength to the corresponding location. When applying random forest algorithm to predict large-scale path-loss [i.120], the ML model determines the path-loss value for a given transmitter-receiver pair together with other auxiliary information. When deploying ML models in multi-channel predictions, the model generally outputs the channel information matrix based on previous channel information, therefore assigning values of channel state information based on the previous values.

7.6.3.2 Generative Models

For channels models where uncertainties are included in the analytical expressions, generative ML models can also be adopted to output similar channel model samples. The uncertainties in the analytical solutions are dealt with by randomizing the input into the generative model.

Two approaches of generative models can be considered. In Approach 1, one can select an analytical channel model of interest (e.g. 3GPP model) for a specific scenario (e.g. outdoor, office, etc.). The generative ML model's goal in this approach is to stochastically generate realistic instances of channel filter parameters based on a dataset - denoted with - that parameterizes the pre-selected channel model. Examples of such parameters are angle of arrival and departure, path gains, impulse responses, etc. The parameterized channel model then acts as a filter through which the transmitted signal is filtered to produce the output received signal. The ML model in Approach 2 - the so-called Black box model - behaves like the stochastic channel itself and therefore directly produces instances of received output signals. For this approach, the dataset can be all input and output I/Q samples, resulting in the size of the dataset much larger than in Approach 1. However, this approach does not require prior knowledge of the channel model. For example, the complex THz channel modeling effects can be directly generated from the generative model based on the dataset. Table 10 shows the summary of both approaches.

Table 10: Summary of generative model approaches

	Generality to different scenarios	Model complexity	Data requirements
Approach 1: generative models for channel parameter generation	Manually customizes the ML model to different environments and mobility scenarios following the traditional channel models' definitions for those specific scenarios.	Complexity could be reduced by the knowledge already encoded in the ML model. However, for (sub-)THz band, where channel models are still under development, successfully capturing the physical effects could prove challenging.	The knowledge encoded in the model can aid in this aspect. Existing and under-development channel models can aid in generating simulated training data.
Approach 2: generative black box model	Data driven approach. Parameters such as velocity and type of environment can be part of the input vector.	This approach may require a complex process of neural architecture search as prior knowledge is not encoded explicitly. However, the level of complexity is tunable (through, e.g. hyperparameter selection), unlike the traditional approach which needs to be parameterized for specific channel effects.	Data requirements are the most challenging aspect of this approach, as the quality and quantity of the training data will determine the quality of the model. Both measured and simulated training data may not include all the effects that need to be captured in the model.

When applying such models for generating channel samples, ML techniques such as transfer learning can be adopted to boost the versatility of the ML models. Environment-related parameters can be used as auxiliary inputs to enable the ML model to perform channel model generation in various scenarios, including transmitter/receiver locations, density and characteristics of the reflecting objects, as well as velocity of the communication nodes.

Furthermore, fine-tuning techniques to transfer the learned knowledge of one scenario to another is also practical when developing generative models. This approach can be especially helpful when there is a large number of channel samples in a specific scene and scarce samples in another. The generative ML model well-trained on the first scene can then be fined tuned with a limited number of samples from the target scene.

7.6.3.3 Physics-Inspired Models

Physics-inspired machine learning models are a class of machine learning algorithms that incorporate principles from physics into their design, e.g. conservation laws. Neural Radiance Fields (NeRF) was firstly proposed in [i.108] to model the radiance field of a scene, which describes how light travels through the scene and interacts with the objects, with neural networks. Since both visible light and wireless communication signals are electromagnetic waves, [i.109] proposed to use the technique for radio frequency signals, so as to model the received signals at a location from different angles. The current limitations of NeRF-related research in channel modelling are that it is highly scene-dependent (e.g. in [i.109], the propagation environment, as well as the transmitter's and receiver's location are fixed). Considering the prerequisites of generating enough samples to train neural network in NeRF^2, the advantages of NeRF^2 shows when there is a need to generate receiving spectrum of a location from all angles while re-running ray-tracing is costly.

Current solutions in generative models and physics-inspired models require a large number of data samples to train the ML model. The capacity for them to generalize and extend beyond the training scenarios is the key of their deployment in realistic channel modelling applications. In other words, the cost of generating samples and training the ML models should be compensated by the models' wide application fields and short deployment time.

7.6.4 Machine Learning for statistical channel modeling

The challenges incurred by modeling the complex phenomena manifesting in THz bands has recently triggered the desire to (partially) defer the task of channel modeling to Machine Learning (ML). The motivating premise is that ML can find patterns or distributions in the data that can capture some of the complex channel effects, especially those occurring at high-frequency bands [i.3]. Yet, some caveats and challenges should be considered in deciding whether to use ML for channel modeling, such as potential overfitting and lack of generalization thereafter, and computational complexity in generating time-variant channel instances.

Generative Machine Learning (ML) models aim to capture the distribution of training data. Therefore, they can be stochastically sampled to generate new data instances that resemble those sampled from the training distribution. In contrast, discriminative ML models are optimized to represent an input-output mapping and thus target a conditional distribution, such as the one used for classification.

Annex A:
Transmission Windows

Recommendation ITU-R P.676-12 [i.22] is commonly used in order to predict the specific attenuation due to gases and related effects to frequencies up to 1 000 GHz, which can be used in order to identify the Transmission Windows (TW) for THz communications. [i.76] brings the concept of transmittance, originally used in free-space optics, to the THz domain in order to define the transmission windows for communications. Transmittance (T), given as a percentage, is defined as the fraction of the incident electromagnetic power that is transmitted through the atmosphere and can be derived from the atmospheric attenuation. Based on the concept of transmittance, Figure A.1 shows the derived transmission windows for a link distance of 100 metres at sea level, temperature of 15° and water vapor density of 7,5 g/m^3.

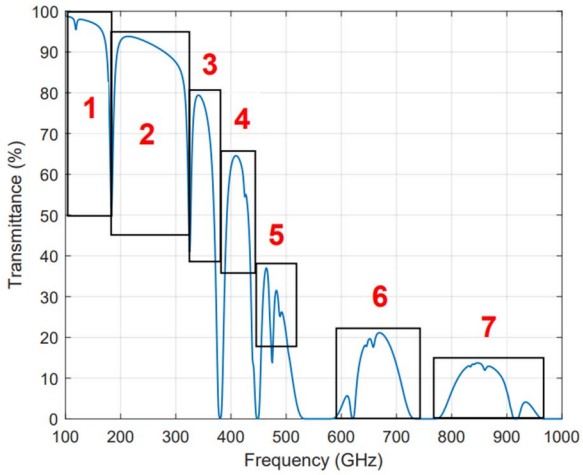

Figure A.1: Transmission windows between 100 GHz and 1 THz at sea level, a temperature of 15° and water vapor density of 7,5 g/m^3

The Bandwidth (BW) of each TW is defined between the values of transmittance relative to the peak value of transmittance of each frequency band. Since the transmittance depends on the link distance both position and BW of the TWs vary with the link distance, see Figure A.2.

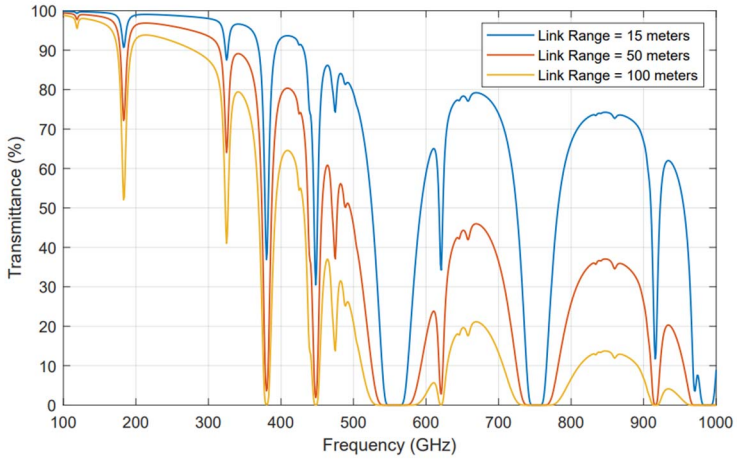

Figure A.2: Transmission windows between 100 GHz and 1 THz for various link distances at sea level, a temperature of 15° and water vapor density of 7,5 g/m^3

Table A.1 lists the TW corresponding to Figure A.2.

Table A.1: Definition of transmission windows depending on the link distance (at sea level, a temperature of 15° and water vapor density of 7,5 g/m^3)

TW	Link Distance (m)	Lower frequency (GHz)	Centre frequency (GHz)	Upper frequency (GHz)	Bandwidth (GHz)
1	15	100	142	183	83
1	50	100	142	183	83
1	100	100	140	180	80
2	15	183	254	325	142
2	50	183	254	325	142
2	100	185	253	321	136
3	15	325	351	376	51
3	50	325	348	371	46
3	100	328	348	369	41
4	15	384	414	443	59
4	50	388	412	436	48
4	100	391	412	433	42
5	15	452	486	520	68
5	50	455	479	502	47
5	100	457	473	488	31
6	15	598	660	722	124
6	50	630	668	705	75
6	100	635	667	696	62
7	15	786	870	953	167
7	50	800	850	900	100
7	100	811	851	892	81

History

Document history		
V1.1.1	December 2024	Publication